Technische Universität München

TUM School of Medicine and Health

Elucidating novel mechanisms of proteolytic ectodomain shedding in Alzheimer's disease and COVID-19

Georg Jocher

Vollständiger Abdruck der von der TUM School of Medicine and Health
der Technischen Universität München zur Erlangung des akademischen Grades eines

Doktors der Naturwissenschaften (Dr. rer. nat.)

genehmigten Dissertation.

Vorsitz: Prof. Dr. Simon Nikolas Jacob

Prüfende der Dissertation:

1. Prof. Dr. Stefan Lichtenthaler
2. Prof. Dr. Carl Blobel, Ph.D.
3. Prof. Dr. Christoph Becker-Pauly

Die Dissertation wurde am 18.09.2023 bei der Technischen Universität München eingereicht und durch die TUM School of Medicine and Health am 20.12.2023. angenommen.

Publications related to this thesis

Jocher, G., Grass, V., Tschirner, S.K., Riepler, L., Breimann, S., Kaya, T., Oelsner, M., Hamad, M.S., Hofmann, L.I., Blobel, C.P., *et al.* (2022). ADAM10 and ADAM17 promote SARS-CoV-2 cell entry and spike protein-mediated lung cell fusion. EMBO reports, e54305.

Güner, G., Aßfalg, M., Zhao, K., Dreyer, T., Lahiri, S., Lo, Y., Slivinschi, B.I., Imhof, A., **Jocher, G**., Strohm, L., *et al.* (2022). Proteolytically generated soluble Tweak Receptor Fn14 is a blood biomarker for γ-secretase activity. EMBO molecular medicine *14*, e16084.

Tüshaus, J., Müller, S.A., Kataka, E.S., Zaucha, J., Sebastian Monasor, L., Su, M., Güner, G., **Jocher, G**., Tahirovic, S., Frishman, D., *et al.* (2020). An optimized quantitative proteomics method establishes the cell type-resolved mouse brain secretome. The EMBO journal *39*, e105693.

ABSTRACT

Protein secretion by proteolytic ectodomain shedding is a key biological process involved in physiology. Two members of the ‘A Disintegrin and Metalloproteinase (ADAM) family, ADAM10 and ADAM17, are major sheddases with ubiquitous expression patterns and over 100 described substrates. As such, they are involved in a multitude of pathophysiological processes. Therefore, targeting these proteases in disease conditions is considered a promising therapeutic approach. Deciphering the molecular consequences of proteolysis is crucial for understanding disease pathogenesis and the discovery of novel therapeutic opportunities.

In this doctoral thesis, I explore proteolytic events in the context of Alzheimer’s disease (AD) and COVID-19.

In the first part of this thesis, I investigate the consequence of ADAM17 loss of function in microglia using mass-spectrometry-based proteomics, and discover that the triggering-receptor on myeloid cells (TREM2), which has been found to carry mutations in patients suffering from late-onset AD, is controlled by the iRHOM2/ADAM17 shedding machinery, thereby providing a plausible mechanistic explanation for why genetic associations of ADAM17 and iRHOM2 could alter disease onset.

The sudden onset of the SARS-CoV-2 pandemic has shifted global research efforts to the study of the SARS-CoV-2 receptor angiotensin-converting-enzyme 2 (ACE2), which is known to undergo ADAM17-dependent ectodomain shedding. However, the involvement of ADAM17 in SARS-CoV-2 disease pathogenesis is largely unclear.

In the second part of this thesis, using a variety of biochemical and virological techniques, I discover that, in addition to the already known cellular entry routes, there is also a metalloprotease-dependent pathway. Moreover, I made the surprising observation that ADAM metalloproteases can directly cleave the spike protein of the coronavirus, triggering pathological lung cell fusion.

In conclusion, this thesis provides an explanation for the increased risk posed by (epi-) genetic variants of iRHOM2 and ADAM17, as they significantly influence the cleavage of TREM2. Furthermore, I have identified ADAM10 and ADAM17 as significant host factors for COVID-19, deciphering new crucial biological concepts in the fields of protease and coronavirus biology.

ZUSAMMENFASSUNG

Die Sekretion von Proteinen durch proteolytische Abspaltung der extrazellulären Domäne ist ein grundlegender physiologischer Vorgang. Zwei bedeutende Mitglieder der "A Disintegrin and Metalloproteinase (ADAM)"-Familie, ADAM10 und ADAM17, sind bedeutende "Sheddasen", die in der Mehrheit der menschlichen Zellen exprimiert sind und über 100 beschriebenen Substrate besitzen. Daher sind sie an einer Vielzahl von pathophysiologischen Vorgängen beteiligt. Das Entschlüsseln der molekularen Konsequenzen dieser proteolytischen Prozesse ist daher entscheidend für das Verständnis der Krankheitspathogenese und für die Entdeckung neuer therapeutischer Möglichkeiten.

In dieser Doktorarbeit vertiefe ich mich in die Untersuchung proteolytischer Ereignisse im Kontext der Alzheimer-Krankheit (AD) und der COVID-19 Erkrankung.

Unter Einsatz von massenspektrometrischer Proteomik untersuche ich die Konsequenzen einer ADAM17-Funktionsstörung in Mikroglia und entdecke dabei, dass die Proteolyse des triggering-receptor on myeloid cells (TREM2), welcher, sofern genetische Mutationen vorliegen, für dieEntstehung der Alzheimer-Krankheit wichtig ist, hauptsächlich von iRHOM2/ADAM17- kontrolliert wird. Damit liefere ich eine plausible mechanistische Erklärung dafür, warum genetische Assoziationen von ADAM17 und iRHOM2 den Krankheitsbeginn verändern können.

Der plötzliche Ausbruch der SARS-CoV-2-Pandemie hat die globalen Forschungsbemühungen auf die Untersuchung des SARS-CoV-2-Rezeptors Angiotensin-Converting-Enzym 2 (ACE2) gelenkt, von dem bekannt ist, dass dieser ADAM17-abhängig gespalten wird. Die Beteiligung von ADAM17 an der Krankheitspathogenese von SARS-CoV-2 ist jedoch weitgehend unklar. Mit verschiedenen biochemischen und virologischen Techniken entdecke ich, dass es neben den bereits bekannten zellulären Eintrittswegen auch einen Metalloprotease-abhängigen Weg gibt. Eine überraschende Beobachtung war außerdem, dass ADAM-Metalloproteasen das Spike-Protein des Coronavirus direkt spalten können, mittels derer die pathologische Fusion von Lungenzellen ausgelöst wird.

Zusammenfassend liefert diese Arbeit eine Erklärung für das erhöhte Risiko, das durch (epi-) genetische Varianten von iRHOM2 und ADAM17 verursacht wird, da sie die Spaltung von TREM2 erheblich beeinflussen. Darüber hinaus habe ich ADAM10 und ADAM17 als bedeutende Wirts-Faktoren für COVID-19 identifiziert und dabei neue, biologische Konzepte in den Bereichen der Protease- und Coronavirus-Biologie erarbeitet.

TABLE OF CONTENTS

ABBREVIATIONS

ACN	Acetonitril
A549	Adenocarcinomic human alveolar basal epithelial cell line
ACE2	Angiotensin-converting enzyme 2
AD	AD Alzheimer´s disease
ADAM	A disintegrin and metalloproteinase
APP	Amyloid precursor protein
BACE	β-site APP cleaving enzyme
BB94	Batimastat
BSA	Bovine Serum Albumin
BSL3	Biosafety Level 3
CNS	central nervous system
ConA	Concanavalin A
COVID-19	Coronavirus disease 2019
CSF	Cerebrospinal fluid
DNA	Deoxyribonucleic acid
DBCO	Dibenzocyclooctyne
DIA	Data independent acquisition
DIV	Days in vitro
DMSO	Dimethylsulfoxide
DPC-333	ADAM17 inhibitor (BMS-561392)
DTT	Dithiothreitol
ECL	Enhanced chemo-luminescence
EDTA	Ethylenediaminetetraacetic acid
EGF	Epidermal growth factor
EGFR	Epidermal growth factor receptor
EGTA	Egtazic acid
ELISA	Enzyme-Linked ImmunoSorbent Assay
ER	Endoplasmic reticulum
FA	Formic acid
FBS	Fetal bovine serum
FDR	False discover rate
GFP	Green fluorescent protein
GI	ADAM10 inhibitor GI254023X
HBSS	Hanks buffered salt solution
HCL	Hydrochloric acid
HEK293T	Human embryonic kidney
hiSPECS	High-performance secretome protein enrichment with click sugars
HPLC	High-performance liquid chromatography
IAA	Iodacetamide

iRhom	Inactive rhomboid
LFQ	Label-free quantification
LPS	Lipopolysaccharide
lysC	Endoproteinase Lys-C
m/z	Mass to charge ratio
MACS	Magnetic Activated Cell Sorting
ManNAz	Tetra-acetylated N-azido-mannosamine
MOI	Multiplicity of infection
MsD	Mesoscale Discovery
MTT	3-(4,5-dimethylthiazol-2-yl)-2,5-diphenyltetrazolium bromide
NaCl	Sodium chloride
NHBE cells	Normal human bronchial epithelial cells
P/S	Penicillin/Streptomycin
PAGE	Poly-acrylamid gel electrophoresis
PBS	Phosphate-buffered saline
PBS-T	Phosphate-buffer saline plus Tween
PCR	Polymerase chain reaction
PDL	Poly-D-lysine
PFA	Paraformaldehyde
PI	Protease inhibitor cocktail
PMA	Phorbol myristate acetate
PNGase F	N-glycosidase F
sACE2	soluble ACE2 (ectodomain of ACE2)
SDS	Sodium-dodecyl sulphate
SDS-PAGE	Sodium dodecyl sulfate polyacrylamide gel electrophoresis
SP3	single-pot, solid-phase-enhanced sample preparation
ß-ME	ß-Mercaptoethanol
TAPI-1	TNF-α Protease Inhibitor-1
TCA	trichloroacetic acid
ThR	Thiazine Red
TM	transmembrane
TMPRRS2	Transmembrane Serine Protease 2
TNFa	Tumor necrosis factor alpha
TREM2	Triggering receptor on myeloid cells
TX-100	Triton-X-100
WGA	wheat-germ-agglutinin

1 INTRODUCTION

1.1 Ectodomain shedding

A key biological concept is the post-translational modification of proteins by proteolysis, because it can alter the conformational state and cellular localisation of a protein irreversibly. An active field of science is the study of proteolysis in the context of ectodomain shedding (or briefly shedding), which is the removal of the extracellular portion of membrane-anchored proteins by proteases. The shedding process is mediated by a group of proteases, including metalloproteases such as ADAMs (A Disintegrin and Metalloprotease Domain), proteases of the BACE (ß-amyloid precursor protein cleaving enzyme) family, transmembrane serine proteases (TMPRS), as well as other protease families (Lichtenthaler et al., 2018) Shedding plays a significant role in the regulation of various cellular processes such as cell signaling and immune responses. Dysregulated shedding events can therefore have detrimental impact on health, being linked to the onset of numerous diseases. This includes neurodegenerative conditions, such as Alzheimer's disease, as well as viral infections, highlighting the importance of shedding regulation for maintaining overall physiological homeostasis (Lichtenthaler et al., 2018; Rosenbaum and Saftig, 2023).

In the context of Alzheimer's disease (AD), shedding initiates the generation of amyloid-beta (Aβ) peptides, the primary components of amyloid plaques observed in the brains of AD patients. The amyloid precursor protein (APP) undergoes sequential cleavage by the β-secretase BACE1 and γ-secretase complex, generating the pathogenic Aβ peptides (Vassar et al., 1999). Alternatively, APP can be cleaved by α-secretase(s) within the Aβ sequence, precluding the formation of pathogenic fragments. The α-secretase function is primarily attributed to members of the ADAM family, particularly ADAM10 and ADAM17, which are both genetic risk factors for AD, highlighting the importance of ectodomain shedding in disease pathogenesis (Jorissen et al., 2010; Kuhn et al., 2010; Lammich et al., 1999). The sequential action of a sheddase and an intramembrane protease such as γ-secretase is commonly referred to as regulated intramembrane proteolysis (RIP). This cascade of proteolytic events leads often to the release of biologically active intracellular domains that translocate to the nucleus and modulate gene expression (Fig. 1)

(De Strooper et al., 1999; Lichtenthaler et al., 2018).

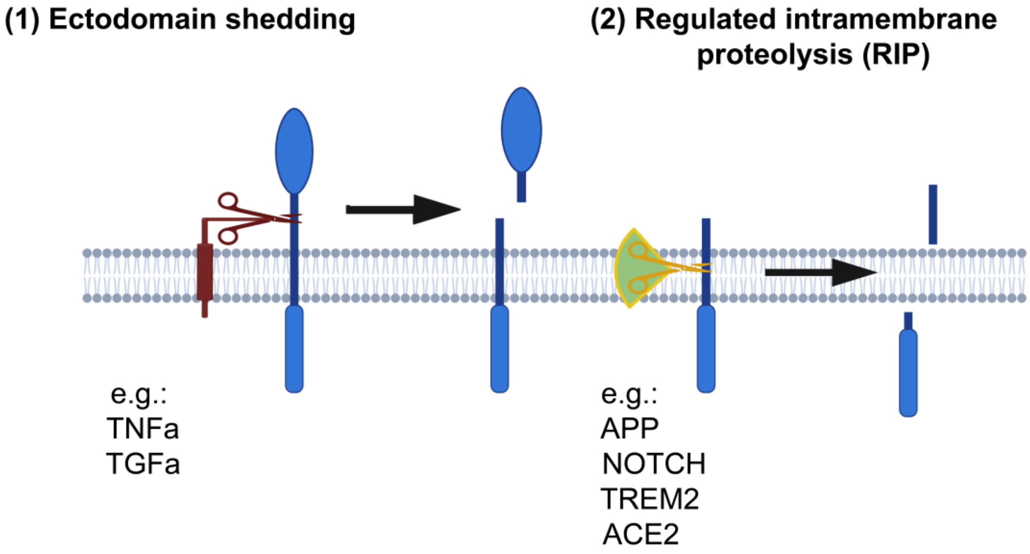

Figure 1: Schematic diagram of proteolytic processing of membrane proteins. First, the ectodomain of a single-pass transmembrane protein (illustrated in blue) is proteolytically liberated, a process termed ectodomain shedding (1). Subsequently, regulated intramembrane proteolysis (2) occurs on the remaining portion of the protein. The detached intracellular segment of the protein may initiate signaling cascades. Figure created with Biorender.

A prominent role of ectodomain shedding in the context of viral infections is well-established, although there are mechanistic differences. This is due to the virus‘ specific requirement of host cell proteases needed for viral entry and spread. Many viruses, including influenza, human immunodeficiency virus (HIV), the tropical disease-causing viruses Ebola and Nipah, and the severe acute respiratory syndrome coronavirus (SARS-CoV), rely on host cell proteases to cleave the viral surface protein at a specific site, thereby releasing the ectodomain from the virus (Gnirss et al., 2012; Weis and Maisner, 2015). For example, influenza hemagglutinin (HA) requires proteolytic cleavage to expose its receptor-binding domain and enable binding to sialic acid receptors on host cells. This process is known to be catalyzed by transmembrane protease serine subtype 2 (TMPRSS2) and other so-called hemagglutinin activating proteases (HATs), which are host cell membrane resident serine proteases (Hoffmann et al., 2018). Shedding does not only help to overcome otherwise sterically unfavorable conformations required for the binding process, but also greatly boost its binding affinity (Kopan and Ilagan, 2009). In this way, proteolysis results in the virus being equipped with an orientation that is important for efficient transmission. While the role of shedding of viral surface proteins is well-documented, much less is known about host cell receptors required for virus binding. Indeed, many of these receptors are known sheddase substrates. These include the receptor for Coxsackie and Adenovirus CAR, Ephrin-B2/B3 for the Nipah virus (all shed by ADAM10), the enterovirus 71 receptor P-selectin glycoprotein ligand 1 (PSGL-1, shed by BACE1), or the SARS-CoV and SARS-CoV-2 receptor ACE2 (shed by TMPRSS2 & ADAM10/17 (Heurich et al., 2014; Lagares et al., 2017; Lichtenthaler et al., 2003; Niehues et al., 2022). The functional contribution of shedding to viral entry and spread is still a topic of debate due to the complexity of the underlying mechanism. This complexity arises from several factors. Firstly, multiple proteolytic events may be necessary, either simultaneously or in rapid succession, to facilitate shedding. Secondly, the exact cleavage sites involved in shedding remain unknown. Finally, genetic manipulations can often cause compensatory changes or produce non-functional proteins, making it challenging to interpret test results with certainty. As such, further research is necessary to fully understand the role of shedding and possible successive proteolytic events in viral infections.

Ectodomain shedding is thus a broad scientific field with countless mysteries that form the basis for understanding of physiology. A main goal of this doctoral thesis is to expand our understanding of ectodomain shedding in the context of Alzheimer’s disease and COVID-19.

1.2 The α-Secretase ADAM10 and ADAM17

ADAM10 and ADAM17 are two members of the ADAM family of transmembrane proteins, which have crucial functions in various cellular processes, ranging from development to neurodegeneration. Indeed, they are considered to be the two most important members among the ADAMs, because they cleave a large range of physiologically relevant substrates, have a ubiquitous tissue distribution, and are implicated in many diseases due to their pivotal role in ectodomain shedding (Rosenbaum and Saftig, 2023; Zunke and Rose-John, 2017).

Both ADAM10 and ADAM17 are expressed as zymogens, which means they are enzymatically inactive and require pre-activation. In the trans-Golgi network (TGN), this is executed by proteolytic removal of the pro-domain through pro-protein convertases such as furin, whereafter the mature forms of these proteins can reach the plasma membrane (Fig. 2) (Wong et al., 2015).

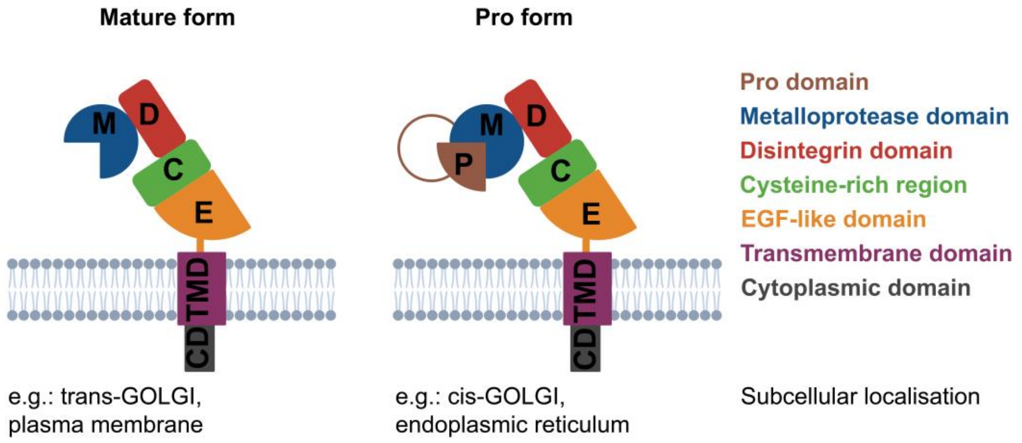

Figure 2: Domain organization of a prototypical, catalytically active ADAM (a disintegrin and metalloprotease) protein. ADAMs are type 1 transmembrane proteins that have a large extracellular domain and a short cytoplasmic tail. The extracellular domain contains the pro-domain, a feature that keeps the protein in an inactive state termed “pro-form”. After removal of the prodomain, the N-terminal most part of the ADAM is the metalloprotease domain containing the active site. Subsequent segments of the extracellular domain include a disintegrin domain, a cysteine-rich domain, and an EGF-like domain, which is not present in ADAM10. Intracellularly, a transmembrane domain coupled with a short cytoplasmic domain serves as a membrane anchor. ADAMs also possess an N-terminal signal sequence, which is not shown here. Figure created with Biorender.

Despite their similar domain structure, ADAM10 and ADAM17 are functionally and mechanistically very different (Hsia et al., 2019). The question of whether and how substrates of ADAM10 and ADAM17 can be distinguished from one another remains a challenging topic and is the subject of ongoing debates. This dissertation encompasses both functional properties of their substrates and mechanistic regulation, and has led to a deeper understanding of these complex molecules. Historically, the principle of locus heterogeneity, which is a central concept in classical genetics, has been leveraged to dissect the functional properties of ADAM10 and ADAM17. The importance of locus heterogeneity in identifying the specific protease responsible for substrate cleavage lies in its ability to provide direct evidence of protein function *in vivo*. By demonstrating that mutating the substrate or directly blocking cleavage by ADAM10 or ADAM17 produces similar or opposing phenotypes than loss of the protein in question, researchers can establish the molecular function of such proteolytic event. This approach can be particularly useful in situations where compensatory mechanisms can mask the effects of individual protein loss, which is common in many *in vitro* studies, or when there is a lack of specific inhibitors.

In 1996, ADAM10 was first discovered in Drosophila, where it is encoded by the gene *kuz* and is important for partioning of non-neuronal and neural cells during development. Clonal Analyses indicated that both *kuz* and *Notch* are required to prevent neural hypertrophy in a cell-autonomous manner (Heitzler and Simpson, 1991; Howard et al., 1996; Rooke et al., 1996). Loss of *kuz* resembles *Notch* loss of function in both Drosphila and vertebrates. Functionally, proteolysis of Notch by ADAM10 is required for lateral inhibition during neurogenesis (Pan and Rubin, 1997).

Almost at the same time, the close homolog ADAM17 was found to be responsible for the conversion of pro-TNFa into it's soluble form as a response to bacterial endotoxins such as Lipopolysaccharide (LPS) (Black et al., 1997; Moss et al., 1997). Blocking sTNFa production by a metalloprotease inhibitor was sufficient to protect animals against an otherwise lethal dosis of LPS (Mohler et al., 1994). This effect was paralleled by the loss of ADAM17, demonstrating that ADAM17 is the *in vivo* relevant sheddase of TNFa. Another prime example of locus heterogeneity is the eyelid fusion deficiency caused by loss of TGFa, which is also seen in ADAM17 knock-out (KO) animals (Peschon et al., 1998).

There are more examples of ADAM10 or ADAM17 specific phenotypes that could be attributed to single substrates that are being cleaved by multiple proteases *in vitro*, but *in vivo* the phenotype manifests only upon loss of the physiologically relevant sheddase. Indeed, substrates that are exclusively being cleaved by ADAM10 or ADAM17 *in vitro* are sparse.

Due to the obvious functional differences between ADAM10 and ADAM17 that were mainly established by genetic studies, researchers tried to understand how ADAM10 and ADAM17 differ mechanistically. One emerging concept was the idea, that they could be switching between active and inactive states and there might be physiological stimuli that would render a protease active at a time. Indeed, it was found that Phorbol esters such as phorbol-12-myristate-13-acetate (PMA) or LPS are strong inducers of ADAM17 activity, while ADAM10 remains largely unaffected by these compounds when they are being used for stimulated shedding experiments both *in vitro* and *in vivo*. Ionomycin, a calcium ionophore, that increases intracellular calcium levels stimulates shedding of substrates by ADAM17 and ADAM10, but ADAM10 only stimuli are not known (Le Gall et al., 2009). A burning matter of concern is whether stimulation of shedding by these stimuli that are often being used at high, non-physiological concentrations, has any relevance for understanding the regulation of these proteases *in vivo*. Arguably, it cannot be excluded that these stimuli do not recapitulate the precise mechanism of action of these proteases, and in fact, it was shown that PMA, when used at 100 nM, induces abnormal levels of active ADAM17 on the cell surface, that physiological stimuli were unable to induce (Lorenzen et al., 2016). On the other hand, detection of subtle biochemical effects are often limited by sensitivity and a narrow detection window of employed assays, which can be overcome by the use of strong stimuli. In fact, there is good correlation of several ADAM17 substrates including TGFa, amphiregulin, HB-EGF, and TNFa in terms of *in vitro* substrate cleavage after PMA or LPS stimulation and their *in vivo* contribution. Notably, several physiological stimuli, including EGF, LPA, BzATP among others, produced similar results than their non-physiological counterparts (Le Gall et al., 2010). This shows that these strong non-physiological stimuli can be used as a surrogate for physiological ADAM17 activation to interrogate protease dependency *in vitro* and in case of LPS probably also *in vivo* (Blobel, 2005). Concerning ADAM10, it was found that it has compared to ADAM17, a much higher baseline activity and does not need external stimulation to see strong effects on ADAM10 substrate cleavage. Taken together, these observations led to the idea that ADAM10 is a constitutively active protease, whereas ADAM17 requires stimulation to expand its full activity (e.g.: (Horiuchi et al., 2007; Le Gall et al., 2009; Zunke and Rose-John, 2017)).

ADAM10 and ADAM17 are key sheddases that are integral to normal physiology. A primary objective of this thesis is, therefore, to broaden our knowledge about their substrate repertoire and to define differences between ADAM10 and ADAM17, because this lays the groundwork for potential therapeutic intervention in the future.

1.3 ADAM10 and ADAM17 as drug targets for therapeutic intervention

The versatile roles of ADAM10 and ADAM17 have catalyzed the development of diverse therapeutic intervention strategies. The major challenge involved was the specific inhibition of these proteases. Most efforts were concentrated on formulating small-molecule active site inhibitors, leading to the evolution of what is known as “hydroxamate-based inhibitors”. However, the first-generation inhibitors, such as Batimastat and Marimastat, failed to pass clinical trials. Their broad-spectrum inhibitory nature and pronounced side effects were the main drawbacks (Bramhall et al., 2002; Drummond et al., 1999; Moss et al., 2008). Consequently, subsequent developmental phases were primarily directed towards fine-tuning the specificity of inhibition for individual proteases, a goal which was achieved with varying degrees of success (Dreymueller et al., 2015; Zhou et al., 2006; Zocchi et al., 2016).

Complementing these efforts, alternative strategies to inhibit ADAM10 or ADAM17 were explored, including the production of antibodies and recombinantly produced pro-domains. These novel approaches demonstrated a highly specific inhibitory effect on the proteases (Atapattu et al., 2012; Moss et al., 2007; Tape et al., 2011; Wong et al., 2016).

However, inhibiting ADAM10 and ADAM17 poses a significant challenge due to the multitude of substrates that are concurrently inhibited throughout the organism. Notably, harmful side effects in adult organisms have primarily been associated with chronic global inhibition (Moss et al., 2008). Despite these challenges, the inhibition of these proteases is generally considered feasible. Looking forward, the key to successful treatment strategies is assumed to lie in the development of targeted approaches that enable tissue-specific and substrate-specific inhibition of ADAM10 and ADAM17. This focus on specificity undoubtedly shapes the future of therapeutic interventions involving these proteases (Wetzel et al., 2017).

Therefore, a promising line of research focuses on finding adaptors of ADAM10 and ADAM17 that can influence their activity as specifically as possible. In the case of ADAM17, the main focus is on the IRHOMs, especially iRHOM2, which regulates ADAM17 in immune cells and mediates certain means of substrate selectivity (Herrlich and Kefaloyianni, 2018; Maretzky et al., 2013; McIlwain et al., 2012b; Zhao et al., 2022). Similar mechanisms are suspected in the case of the tetraspanin-C8 family, which are ADAM10 adaptors and potential shedding modulators (Haining et al., 2012; Jouannet et al., 2016; Lipper et al., 2023).

To summarize, a wealth of innovative ideas are emerging that aim to specifically inhibit the proteolysis of ADAM10 and ADAM17 substrates. However, the prerequisite of these strategies is a thorough examination of what substrates are cleaved by which protease(s) and understanding the implications of this cleavage for physiology.

In this doctoral thesis, two major topics were addressed that aim to contribute to the understanding of ADAM10 and ADAM17, with the ultimate goal of developing new therapeutic intervention strategies. The first part deals with the function of ADAM17 and its adaptor iRHOM2 in the context of Alzheimer's disease. The second part explores the role of ADAM10 and ADAM17 in the cleavage of ACE2 and its significance for SARS-CoV-2 cell entry and pathogenesis.

1.4 PART I: ADAM17 and its regulator iRHOM2 in Alzheimer's disease

ADAM17 was the first ADAM to be identified to contribute to ectodomain shedding of APP (Buxbaum et al., 1998), and was therefore linked to the etiology of Alzheimer's disease pathology, as APP processing lies at the basis of the amyloid cascade hypothesis – the central theory of Alzheimer's disease pathogenesis (Ballard et al., 2011). Indeed, a rare mutation that reduces ADAM17 activity has been associated with increased risk for late-onset Alzheimer's disease (LOAD) and this was mainly attributed to its role in restricting the α-cleavage of APP (Hartl et al., 2020). Yet, it is noteworthy that ADAM10 is primarily responsible for APP cleavage in neurons (Kuhn et al., 2010), whereas ADAM17 is mostly recognized for its pro-inflammatory function in immune cells, such as microglia, primarily due to its role in TNFa processing.

Previous studies mainly focused on the role of neurons in AD, largely due to disease-associated mutations in *APP* that cause familial forms of AD. The role of microglia, however, is becoming increased appreciation in the development of sporadic forms of AD. Indeed, recent studies identified a significant proportion of risk genes that are selectively or primarily expressed in microglia relative to other cell types in the brain (Lambert et al., 2013; Srinivasan et al., 2016). Beyond the common genetic variants identified by Genome-Wide Association Studies (GWAS), rare genetic loci have further substantiated the important role of microglia in determining the risk of developing AD (Guerreiro et al., 2013; Sims et al., 2017). Interestingly, a study that investigated epigenetic traits implicated *iRHOM2*, a newly identified regulator of ADAM17 in myeloid cells, in enhancing the risk to develop LOAD (De Jager et al., 2014). Notably, the expression of iRHOM2 was found to be upregulated in LOAD patients compared to age-matched controls. Given these findings, it is tempting to hypothesize that mutations or epigenetic alterations that alter ADAM17 activity in microglia may increase the risk for LOAD, but the precise molecular mechanism is elusive.

Mechanistically, iRHOM2 controls the trafficking and maturation of ADAM17 (Fig. 3) specifically in microglia, while in other cell types of the brain, the close homolog IRHOM1 is the main regulator of ADAM17 maturation (Adrain et al., 2012; Li et al., 2015; McIlwain et al., 2012b). In microglia, one of the best-studied substrates of the ADAM17/iRHOM2 complex is TNFa. It's widely recognized that chronic neuroinflammation, characterized by elevated levels of sTNFa, is a persistent feature of Alzheimer's disease brains (Heneka et al., 2015). However, the role of inflammation in exacerbating or ameliorating Alzheimer's disease (AD) pathology is a subject of ongoing debate (Kwon and Koh, 2020). Indeed, conflicting evidence regarding the contribution of TNFa to AD pathology exists. A frequently used approach to address this question involves inducing a TNFa surge by LPS administration to various routes in mouse models of Aß-built up. Interestingly, evidence for both increased (Michaud et al., 2013; Qiao et al., 2001) and decreased (DiCarlo et al., 2001; Herber et al., 2007) Aß-burden after LPS stimulation are reported. These conflicting results are typically attributed to the varying experimental conditions including, but not limited to, mouse genetic background, age-at-onset of plaque formation, and LPS dosage (Jendresen et al., 2019). Consequently, the role of the ADAM17/iRHOM2/TNFa axis in the risk for LOAD remains uncertain, and it is therefore very much likely that substrates, other than TNFa, contribute significantly.

Among the many described ADAM substrates in microglia, the triggering receptor on myeloid cells (TREM2) is a major risk factor for LOAD, and known for its important role in microglial response to Aß plaques and transition to a disease-associated phenotype (DAM) (Keren-Shaul et al., 2017). DAM microglia are considered to be protective, because they are required for Aß-plaque compaction, the clearance of myelin debris, and neuronal health (Bosch-Queralt et al., 2021; Meilandt et al., 2020; Nugent et al., 2019). Numerous TREM2 coding variants alter the risk for AD. Most of the disease-associated mutations affect cell surface levels and signaling by modulation of ectodomain shedding. However, the identity of the physiologically relevant sheddase is not fully resolved, although significant attempts to answer this question were undertaken. The current state of research considers both ADAM17 and ADAM10

(Feuerbach et al., 2017; Schlepckow et al., 2017) as the main sheddases, but also other proteases are implicated (Berner et al., 2020).

Thus, to address why alterations in ADAM17/iRHOM2 proteolytic activity could increase the risk to developing LOAD, we set out to study iRHOM2 function in microglia.

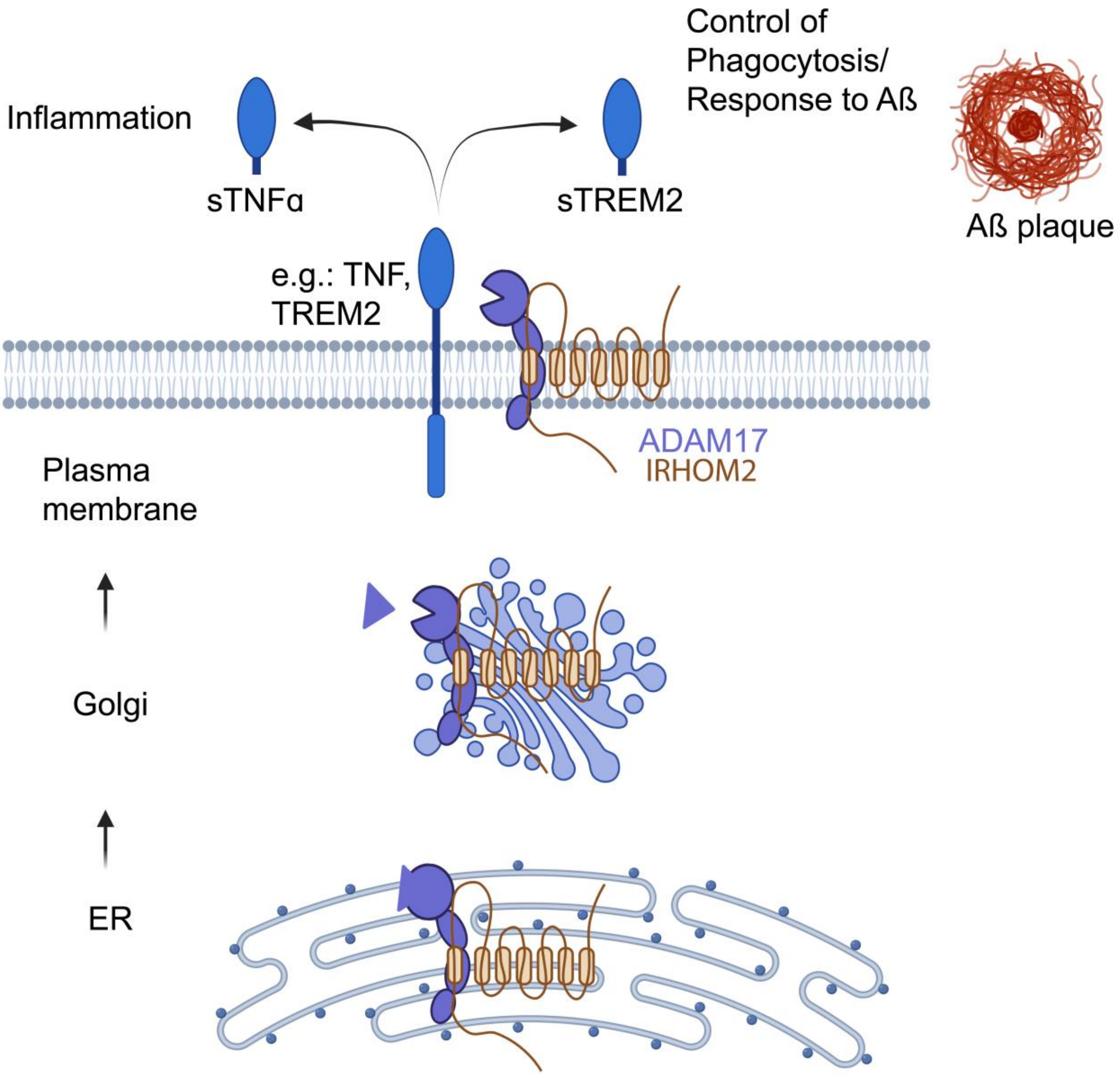

Figure 3: Maturation and proteolysis by ADAM17 in microglia. ADAM17 requires iRHOM2 for intracellular trafficking and maturation. Furthermore, ADAM17/iRHOM2 control ectodomain shedding of physiologically important substrates such as TNFa or TREM2. Proteolysis of these substrates may have consequences for the build-up of amyloid (Aß) plaques. Figure created with Biorender.

1.5 PART II - Ectodomain shedding and Proteolysis in COVID-19

The sudden onset of the Coronavirus crisis has thrown health systems worldwide into great distress. Although the new SARS-CoV-2 virus resembles the first one (SARS-CoV-1), the molecular biological determinants, which are important for understanding and developing effective medications, are to date inadequately elucidated. Given that the Coronavirus receptor ACE2 is a known substrate candidate of ADAM17, we have decided to contribute our knowledge of the regulation of ADAM17 and ADAM10, which we know from the study of other substrates important for Alzheimer's disease, such as APP and TREM2, to help combat the global pandemic. The second part of this thesis covers therefore our work about the enigmatic role(s) of ADAM metalloprotease in COVID-19.

1.5.1 The SARS-CoV-2 receptor Angiotensin-converting enzyme 2 (ACE2)

The Angiotensin-converting enzyme 2 (ACE2) is a key regulator in the Renin-Angiotensin-Aldosteron system (RAAS), which controls blood pressure homeostasis, as well as the body’s salt and fluid balance (Boehm and Nabel, 2002; Imai et al., 2005; Skeggs et al., 1980). Dysregulation of ACE2 can give rise to acute respiratory distress syndrome (ARDS), the most severe form of acute lung injury induced by multiple triggers such as sepsis, pneumonia, acid aspiration, and notably, SARS-CoV infection. Shortly after the first coronavirus pandemia (2002/2003), it was found that ARDS caused by SARS-CoV directly involves ACE2, by serving as the receptor for the “spike” glycoprotein (or simply S protein) located on the surface of SARS-CoV (Imai et al., 2005; Kuba et al., 2005; Li et al., 2003). ACE2 is itself a carboxypeptidase that chops off the C-terminal leucine of Angiotensin 1 (ANG1) to generate ANG1-9, and also removes the C-terminal phenylalanine of Angiotensin 2 (ANG2) to produce ANG1-7. Its close homolog ACE converts ANG1 into ANG2, which is a ligand for the Angiotensin 2 type 1 receptor (AT1R) responsible for vascular permeability and subsequent acute lung failure (Imai et al., 2005). Thus, ACE2 acts by imposing a negative feedback mechanism to counterbalance ACE-mediated ANG2 production (Fig 4).

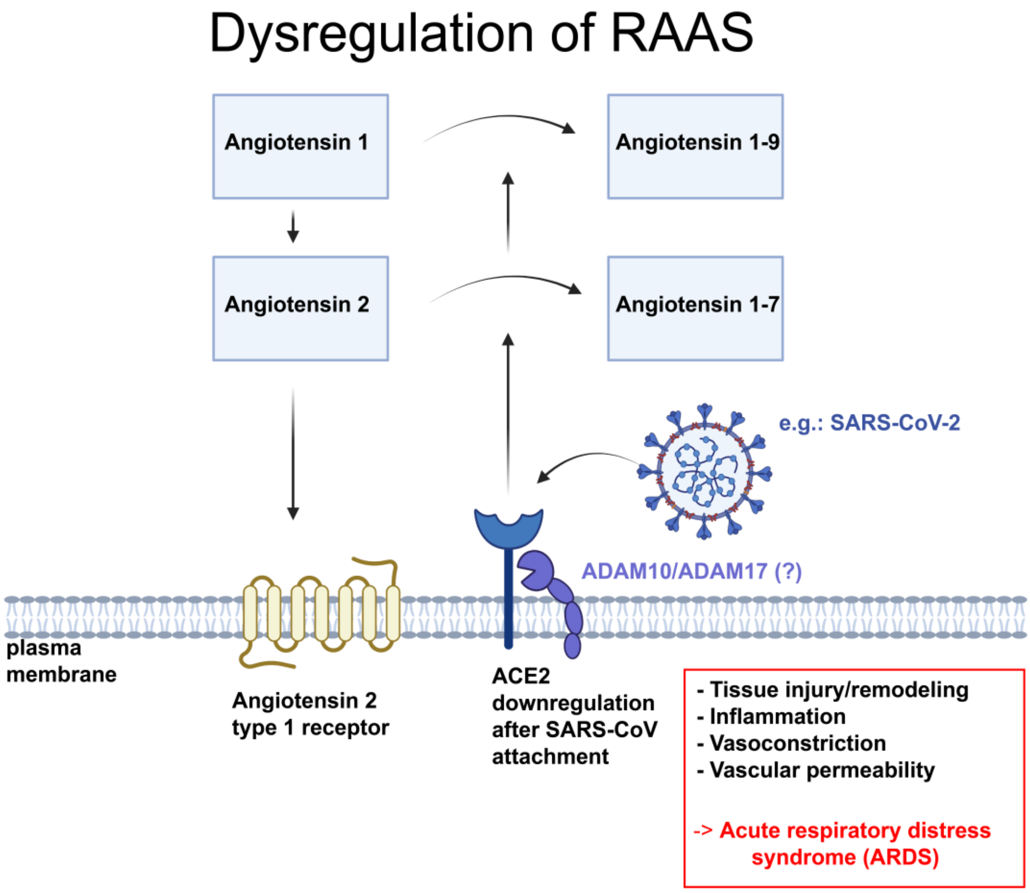

Figure 4: The Angiotensin converting enzyme 2 (ACE2) is an ADAM substrate and an integral part of the renin-angiotensin-aldosteron-System (RAAS). Downregulation of ACE2 causes dysregulation of the RAAS. Severe forms of imbalance triggered by, for instance, ACE2-engaging coronaviruses can lead to the acute respiratory distress syndrome (ARDS). ACE2 undergoes proteolytic ectodomain shedding, but its contribution to SARS-CoV-2 pathogenesis is not understood. Figure was adapted from (Gupta et al., 2020) and created with Biorender.

In instances of an ACE2-engaging coronavirus infection, the interaction of S and ACE2 leads to the downregulation of ACE2, thereby increasing the circulating levels of Angiotensin 2 and increasing the activation of the AT1R. However, the precise mechanism underlying the downregulation of ACE2 – whether it occurs at the transcriptional level, through protein degradation, or via enhanced ectodomain shedding – is not understood (Kuba et al., 2005). It is known that ACE2 undergoes proteolytic ectodomain shedding and that proteolysis could be mediated by ADAM17 (Lambert et al., 2005). Furthermore, a follow-up study implicated ADAM17-mediated ACE2 shedding upon S protein engagement, proposing a ligand-induced shedding mechanism to be facilitating SARS-CoV entry (Haga et al., 2008). Although it seems clear that ACE2 shedding is mainly mediated by ADAM17 in human airway epithelial cells, the cleavage-resistant mutant ACE2-L584A did not alter SARS-CoV entry, suggesting that the membrane-bound ACE2 is required for infection (Jia et al., 2009). Conflicting reports occurred in a study that investigated the role of a transmembrane serine protease (TMPRSS2) in the context of ACE2 shedding and S protein activation (discussed in chapter 1.7). The study showed that in TMPRRS-expressing cells, ACE2 cleavage is mediated by TMPRRS2 and the authors concluded that ADAM17 was dispensable for infection of these cells (Heurich et al., 2014).

Given these uncertainties amid the ongoing SARS-CoV-2 pandemic, understanding the role of ADAM metalloproteases holds paramount significance. This knowledge could potentially influence the treatment paradigm of COVID-19 and ACE2-related syndromes.

1.5.2 The coronavirus spike protein and host cell entry routes

The spike (S) protein of a prototypical coronavirus (CoV) is a type 1 transmembrane protein that is comprised of two functionally different subunits, the S1 and S2 domains (Fig. 5). The S protein is functionally inactive in its native form, and requires proteolytic cleavage by host cell proteases to achieve full activity. After initial removal of the N-terminal signal peptide that primes the nascent polyprotein for ER import, the S protein becomes post-translationally modified by the addition of N-linked glycans, which is supposed to be crucial for receptor binding and immune evasion (Walls et al., 2016b). Further, the S protein is transported to the endoplasmic reticulum/Golgi intermediate compartment (ERGIC), the primary budding site of coronaviruses. The S proteins are incorporated into the viral membrane and further transported through the secretory pathway to exit the host cell (Masters, 2006). The virion can then engage its target receptor on another target cell. Structural studies revealed a homotrimeric configuration of the spike protein before it attaches to the host cell membrane. Once the receptor has been bound by S1 harboring the receptor binding domain (RBD), the spike protein undergoes a conformational change, leading to exposure of the S2 domain that interacts with the host cell membrane (Walls et al., 2020; Walls et al., 2016a). Two sequential proteolytic priming events are required, that ultimately lead to the activation of the fusion peptide by catalyzing the fusion of the viral envelope with the host cell membrane. The first proteolytic priming occurs at the so-called S1/S2 boundary site. This site is located on the S1/S2 boundary site and consists of a cleavage motif (Fig. 5) for host cell proteases. The second cleavage occurs at the so-called S2' site, which is located in the S2 domain just N-terminally of the fusion peptide. The SARS-CoV requires two subsequent cleavage events by a TMPRSS2 at the S1/S2 site and at the S2' site to trigger virus-host membrane fusion. Other coronaviruses pathogenic to humans, such as the Middle-East respiratory distress syndrome causing coronavirus (MERS-CoV) and SARS-CoV-2, harbor a multibasic (characterized by the occurrence of multiple basic residues) cleavage motif at the S1/S2 site and are not exclusively limited to the use TMPRRS2 to execute both cleavages (Hoffmann et al., 2020; Park et al., 2016).

Notably, it was found that coronaviruses equipped with a multibasic cleavage site use proteases of the constitutive secretory pathway of infected cells, such as furin, to prime the S1/S2 site. However, the S1 and S2 domain remain non-covalently attached, thereby maintaining a functional S protein. The advantage of this "pre-priming" of S is arguably that only a single cleavage at the S2' site is further required to activate the fusion peptide, and it is well-established that multibasic cleavage sites at S1/S2 increase pathogenicity (Hoffmann et al., 2018; Hoffmann et al., 2020). Furthermore, it is appreciated that several enzymes, that belong to different protease families can be hijacked by coronaviruses for priming. These proteases are located at different sites in cells, and their subcellular localisation determines the site of S protein-driven membrane fusion. For example, cathepsin L that is expressed in endosomes was shown to contribute to CoV entry by cleaving the S protein on the S2' site to allow membrane fusion intracellularly (Simmons et al., 2005). In contrast, S2' priming at the cell surface is established to be conducted by members of the type 2 transmembrane serine protease (TTSP) family, of which TMPRSS2 is the most prominent member (Hoffmann et al., 2020).

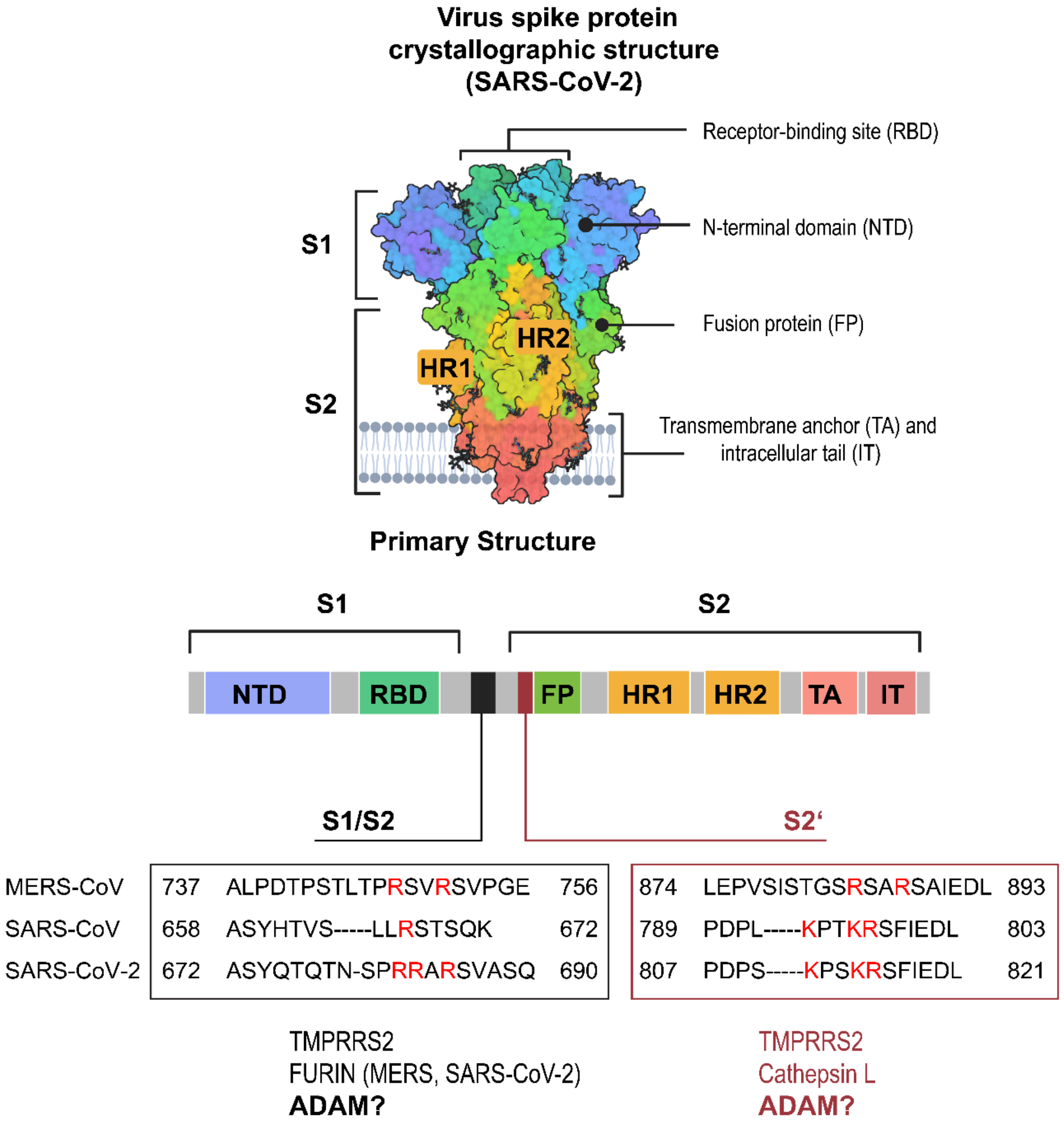

Figure 5: Three dimensional (3D) and primary structure of a coronavirus spike protein. The crystallographic structure shows the homotrimeric configuration of the SARS-CoV-2 spike protein. The domain organization is highly conserved among multiple members of pathogenic coronaviruses, but the primary structure of the proteolytic cleavage sites at the S1/S2 boundary and the S2 prime site (S2’) for engagement with host cell proteases differs among the closely related MERS-CoV, SARS-CoV, and SARS-CoV-2. MERS-CoV and SARS-CoV-2 harbor a multibasic cleavage site at the S1/S2 boundary site, making it susceptible to intracellular priming by FURIN. The atomic structure derived from (Walls et al., 2020), and can be accessed online (PDB ID: 6VXX-PDB). Figure was adapted from ” An In-depth Look into the Structure of the SARS-CoV2 Spike Glycoprotein ” created by Diana Sofia Mollocana Yanez and Nima Vaezzadeh using BioRender.com. Retrieved from *https://app.biorender.com/biorender-templates*.

Accordingly, coronaviruses can infect cells through two distinct cellular entry pathways.

The endocytic/lysosomal entry pathway (hereafter: endosomal entry/fusion) requires the initial endocytosis of the virus. The virus is then transported to the lysosomes, where the pH is favorable for Cathepsins to cleave the spike protein at the S2' site, ultimately facilitating the transfer of the viral genetic material into the cytoplasm for replication. Hence, inhibitors of lysosomal acidification, such as hydroxychloroquine, or Cathepsin inhibitors like E64d have proven efficiency to block entry of SARS-CoV, MERS-CoV, and SARS-CoV-2. By contrast, infection through the cell surface entry pathway (hereafter: cell-surface entry/fusion) is pH-independent, because it happens directly at the plasma mediated by TMPRRS2, which does not require an acidic environment. The relative contribution of endosomal fusion and cell surface fusion are thus determined by the expression of host cell proteases and the properties of the viral S protein. Generally, it is postulated that coronaviruses preferentially use the cell surface fusion pathway in TMPRRS2-expressing cells, whereas TMPRRS2-negative cells are typically infected via the endosomal entry route (Fig.6).

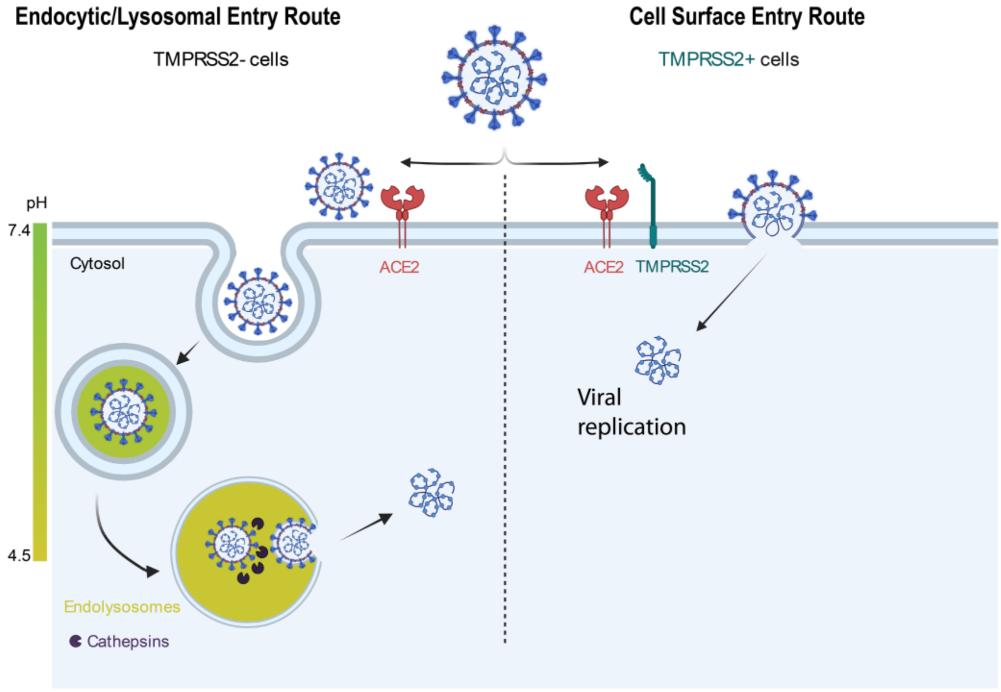

Figure 6: Coronaviruses can enter cells via two entry pathways. The endocytic/lysosomal entry route depends on the activity of pH-dependent cysteine proteases such as Cathepsin L. Entry via direct membrane fusion occurs on the plasma membrane and requires the activity of TMPRSS2. The predominant entry of a certain coronavirus into human cells is determined by available proteolytic cleavage motifs in the S1/S2 and S2' site. This scheme illustrates the entry of SARS-CoV, and SARS-CoV-2 via ACE2. Notably, MERS-CoV uses DPP4 as its receptor. Figure created with Biorender.

Together, proteolytic priming of the S protein is a common motif of pathogenic coronaviruses to enable viral entry at distinct cellular sites, and ultimately, determines viral tropism. Astonishingly, the novel SARS-CoV-2 virus exhibits a markedly enhanced viral tropism compared to its predecessors. Whereas SARS-CoV and MERS-CoV primarily infected cells of the upper respiratory tract, and in severe cases, the lungs, SARS-CoV-2 prompts symptoms affecting a much wider range of organs beyond the lungs (Gupta et al., 2020). Hence, it is now established that COVID-19 is a multisystem syndrome, with instances of neuroinvasion being reported (Liu et al., 2021). Therefore, it is tempting to speculate as to how this dramatically increased viral tropism can occur. A plausible explanation for this could be the utilization of other host cell proteases, which also allow rapid entry at the cell surface in other cells that have low levels of TMPRSS2 or related proteases expressed.

Thus, a major aim of this thesis was to examine the possibility that a metalloprotease could contribute to SARS-CoV-2 infection, either by acting on the SARS-CoV-2 receptor ACE2 or by priming of the viral S protein.

2 AIMS OF THE STUDY

The overarching goal of this thesis is to elucidate novel mechanisms of the alpha-secretases ADAM10 and ADAM17 within the context of Alzheimer’s disease and COVID-19. The motivation arises from the understanding that ADAM inhibition holds significant therapeutic potential. Although undesired effects of ADAM inhibitors have been reported, substantial progress is being made to address these concerns. To foster these developments, it is crucial to identify and characterize the underlying molecular function of ADAM substrates.

In the context of AD, the role of iRHOM2 has emerged to be increasing the risk for onset of the disease. Disentangling the role of iRHOM2 in microglia may establish ADAM17 inhibition as a novel therapeutic intervention strategy for AD. Targeting iRHOM2 may an elegant way to specifically inhibit ADAM17 in microglia, because other important physiological ADAM17 functions in other cell types are mostly IRHOM1-dependent.

The first part of this thesis embarks on the following objectives:

1. Charting the substrate repertoire of iRHOM2/ADAM17 in primary microglia.

2. Validation of substrate candidates and establishing a causal explanation to late-onset Alzheimer’s disease by functional/mechanistic analysis of AD-linked substrates.

For COVID-19 while the involvement of ADAM metalloproteases is suspected, their contribution to disease pathogenesis is largely unexplored. Investigating the role of these metalloproteases in SARS-CoV-2 entry might explain its broad tissue tropism. Disentangling the molecular mechanism and establishing the involvement of ADAMs in SARS-CoV-2 disease can thus open up new therapeutic possibilities.

The second part of this thesis includes therefore the following aims:

1. Exploring whether and how ADAMs contribute to SARS-CoV-2 pathogenesis.

2. Assessing whether ADAM inhibition represents a novel therapeutic strategy for treating COVID-19.

3 MATERIAL AND METHODS

3.1 MATERIAL

Table 1 Antibodies

Antibody	Source
ACE2	bio-techne (#AF933)
ADAM10 [EPR5622]	Abcam (#ab124695)
ADAM17	Sigma-Aldrich (#AB19027)
ADAM17-C-term	Blobel laboratory (Schlöndorff et al., 2000)
Alexa Fluor 488	Abcam (#ab150077)
alpha-TUBULIN	Abcam (#ab4074)
Anti-Mouse IgG HRP	Promega (#W4021)
Anti-Rabbit IgG HRP	Promega (#W4011)
Anti-Rat IgG HRP	Life (#31470)
Anti-rat Sulfo-tag	Meso Scale Discovery (#R32AH-1)
Aß (3552)	Lichtenthaler laboratory
Calnexin	Enzo Life Sciences (#ADI-SPA-860)
CD68	Bio-Rad (#MCA1957)
CNPase [11-5B]	Abcam (#ab6319)
GFAP	Abcam (#ab7260)
GFP	Biozol (#FGR-20R-GR011)
His-tag [3D5]	Feederle laboratory
IBA1	Thermo Fisher (#PA5-27436)
iRHOM2	Lichtenthaler laboratory (Weskamp et al., 2020)
SARS Spike CoV-2 [1A9]	Genetex (#GTX632604)
ß-ACTIN	Sigma-Aldrich (#A5316)
ß-III-TUBULIN	Sigma-Aldrich (#T8578)
TREM2 [5F4]	Haass laboratory (Kleinberger et al., 2014)

Table 2 Equipment & Material

Equipment	Source
0.45 µm pore-size membrane filter	VWR (#MILFHNWP04700)
15 mm glass coverslip	Fisher Scientific (# 501215160)
96-well plate	Thermo Fisher (#442404)
BCA Kit	Interchim (#UP40840A)
BEGM Bronchial epithelial BulletKit	Lonza (#CC-3171 & CC-4175)

C18 analytical column	Dr. Maisch GmbH (#ReproSil-Pur 120 C18-AQ)
CD11b Microbeads	Miltenyi (#130-093-634)
Cell strainer	Fisher Scientific (#15370801)
Clear Polystyrene Microplates 25 Pack	Biotechne (#DY990)
Costar Spin-X Columns 0.22 µm	Merck (CLS8160)
CyQUANT MTT assay	Thermo Fisher (#V13154)
DBCO beads	Jena Bioscience (#CLK-1037-1)
Duolink proximity ligation assay	Sigma-Aldrich (#DUO92007)
ELISA Plate Sealers 100 Pack	Biotechne (#DY992)
Falcon tubes	Thermo Fisher (#AM12502)
Forceps	Fine Science tools (#11251-35)
Human ACE-2 DuoSet ELISA 1 Kit (for 5 Plates)	Biotechne (#DY933-05)
human TNF alpha tissue culture kit	Meso Scale Discovery (#K151E3S)
ImmunoSpot S5 analyzer	C.T.L. Europe
Incucyte S3	Sartorius
LEICA TCS SP5	Leica
MACS Separator	Miltenyi (#130-091-051)
Mini-PROTEAN tetra vertical electrophoresis cell	Biorad (#1658004)
MSD Gold Streptavidin plates	Meso Scale Discovery (#L45SA-2)
nanoElute nanoHPLC	Bruker
Neuronal Dissociation Kit	Miltenyi (#130-092-628)
Nitrocellulose	Biorad (#1704159)
Nunc immuno-plate F96	Thermo Fisher (#442404)
Qubit 3 Fluorometer	Thermo Fisher (#Q33327)
Qubit Assay kit	Thermo Fisher (#Q33212)
RNA 6000 Nano Kit	Agilent (#5067-1511)
RNeasy Plus Micro Kit (50)	Qiagen (#74034)
sAPPa ELISA kit	IBL (#JP27734)
Scissors	Fine Science tools (#14040-10)
SeraMag Beads A	Thermo Fisher (#09-981-121)
SeraMag Beads B	Thermo Fisher (#09-981-123)
T175 flask	Thermo Fisher (#156505)
T75 flask	Thermo Fisher (#156472)
TC20 Automated Cell Counter	Biorad
Tecan Infinite M200 Nanoquant	Tecan
Trans-Blot Turbo Transfer System	Biorad (#1704150)
ZEISS LSM 900	Zeiss
µ-Slide 8 Well high ibiTreat #1.5 polymer coverslip	ibidi (#80806)

Table 3 Reagents and Chemicals

Reagent	Source
Acetonitrile	Biosolve (#01204101)
BEBM Bronchial Basal Medium, 500 ml	Lonza (#CC-3171)
Bodipy 493/503	Life (#D3922)
Bovine Serum Albumin	Sigma-Aldrich
Brij-35	Merck (#8.01962)
DMEM	Thermo Fisher (#61965059)
DMEM/F12	Lonza (#BE12-719F)
DMSO	Roth (#4720.4)
DTT	Sigma-Aldrich
ECL reagent	GE Healthcare
EDTA	Sigma-Aldrich (#108421)
EGTA	Sigma-Aldrich
ELISA Plate-coating Buffer	Biotechne (#DY006)
FBS	Life Technologies
formic acid	Sigma-Aldrich
GI254023X	Sigma-Aldrich (#SML0789)
HBSS	Thermo Fisher (#14170112)
HCL 32%	Merck (#100319)
Hoechst	Thermo Fisher (#62249)
Hygromycin B	Merck (#H3274)
Iodoacetamide	Sigma-Aldrich
lentiCRISPRv2 vector	Addgene (#52961)
Lipofectamine 2000	Thermo Fisher (#11668027)
LysC (mass spec grade)	Promega (#VA1170)
OPTIMEM	Thermo Fisher (#51985042)
Paraformaldehyd	Merck (#158127)
pcDNA3.1-VSVG	Lichtenthaler laboratory
Penicillin/Streptomycin	Thermo Fisher (#15070-063)
phenol-free DMEM	Thermo Fisher (#21063029)
PNGase F	NEB (#P0709S)
Polybrene	Merck (#TR-1003)
poly-D-lysine	Sigma-Aldrich
Protease inhibitor cocktail	Sigma-Aldrich (#P8340)
Puromycin	Sigma-Adrich (#P8833)
pxPAX2	Lichtenthaler laboratory
Read-buffer (4x)	Meso Scale Discovery (#R-92TC-3)
Reagent Diluent Concentrate 2 (10X 5 x 21 mL)	Biotechne (#DY995)
Recombinant ADAM10	Biotechne
Recombinant ADAM17	Enzo Life Sciences
recombinant soluble ACE2	Life (#RP87703)

Recombinant spike protein	Sino Biologicals (#SIN-40589-V08B1)
Recombinant TMPRRS2	Biozol (#LS-G57269-20)
RPMI	Thermo Fisher (#21875034)
Skim Milk Powder	Sigma-Aldrich
Sodium azide (NaAzide)	Merck (#1.06688)
sodium butyrate	Sigma-Aldrich
Stop Solution 2N Sulfuric Acid (15 x 6 mL)	Biotechne (#DY994)
Substrate Reagent Pack (8 vials Color A 8 vials Color B)	biotechne (#DY999)
trichloroacetic acid	Sigma-Aldrich (#T0699)
Tris-HCL	Merck (#108319)
Triton-X-100	Merck (#1.08603)
trypan blue	Biorad (#1450021)
trypsin-EDTA	Thermo Fisher
Tween	Merck (#8.22184)
ZnCl2	Merck (#39059)

3.2 METHODS

To simplify the search process, the main chapters of this methods section are listed in alphabetical order.

3.2.1 Animal work and mouse models

All mouse work was performed in accordance with the European Communities Council Directive and animal experiments were approved by the Regierung von Oberbayern under the license code #02-19-067. Breeding and housing of the mice took place at the pathogen-free animal facility in the German Center for Neurodegenerative diseases (DZNE) Munich.

The *iRhom2*$^{-/-}$ mice were obtained from the laboratory of Prof. Carl P. Blobel (international termination: B6.129-iRhom2tm1Mak). The targeting strategy and characterization of this line has been described previously (McIlwain et al., 2012b). For maintenance of this mouse line, heterozygous animals were mated and the genotype of the offspring was determined with PCR and agarose gel electrophoresis. The genomic DNA was typically isolated from a tail clip or ear notch using standard procedures. The PCR was performed using the following primers for *Wildtype* and *iRhom2* knock-out reactions, respectively.

Wildtype forward primer: 5’ – GCCAGAGAGAACTGGAGCTG – 3 ‘

Wildtype reverse primer: 5’ - CTGCAAGAGATGTGGGTGAA - 3’

iRhom2$^{-/-}$ forward primer: 5’ – ACTGACTTGCTCCGACCACACC– 3 ‘

iRhom2$^{-/-}$ reverse primer: 5’ - CAGCTCATTCCTCCCACTCATG- 3’

3.2.2 Bioinformatics and statistical analyses

The software Graphpad Prism 8.2.1 was used to display the results of Part I of this doctoral thesis, except for proteomics and transcriptomics data, which is described separately in chapter 3.2.5.5 and 3.2.7.3, respectively. For Part II, statistical analyses and data visualization was performed using Python 3.8 using the following packages: Pandas 1.1.4, Matplotlib 3.3.4, Seaborn 0.11, Scipy 1.6.2, Statsmodels 0.12.2.Calculations of standard curves for ELISA or BCA assay were performed as indicated in the respective chapters.

3.2.3 Cell culture

Cell culture work was carried out strictly under a laminar flow workbench to ensure a sterile work environment. Cell lines were grown and maintained in T75/T175 cell culture flasks. For passaging, the cell lines were split before reaching confluence. Briefly, cells were detached by incubating them 5 minutes in 3-5 ml Trypsin-EDTA. Cells were collected in 50 ml falcon tubes, centrifuged for 5 min at 600 x g. Trypsin-EDTA was quantitatively aspirated and cells were split in ratio 1:10 or 1:20 depending on the cell line and cell number, which was determined by live/dead counting via trypan blue. The preparation of the cell culture media was carried out as follows: DMEM, RPMI, DMEM/F12, or OPTIMEM was purchased from Thermo Fisher. The media was supplemented with 50 ml of FBS, and 5 ml of Penicillin/Streptomycin, and then aliquoted in 50 ml falcons and stored at 4°C until use. The specific cell culture medium utilized for each individual cell line is listed in chapter 3.2.3.1.

3.2.3.1 Cell systems

The following cell lines were used in this study.

The adenocarcinomic human alveolar basal epithelial cell line “A549” was cultured in DMEM (Thermo Fisher, #61965059). A549 cells were split 1:20 every other day. Cells were kindly provided by Prof. Pichlmair.

Human embryonic kidney “HEK293T” cells was cultured in DMEM (Thermo Fisher, .3#61965059). HEK293T cells were split 1:10 every other day.

The human histiocytic lymphoma cell line “U937” was cultured in RPMI (Thermo Fisher, #21875034). U937 cells were split 1:10 every other day.

The african green monkey kidney cell line “VeroE6” cells were cultured in DMEM (Thermo Fisher, #61965059) VeroE6 cells were split 1:10 every other day. Cells were kindly provided by Prof. Pichlmair.

Primary microglia from mouse brains (see chapter 3.2.3) were cultured in DMEM/F12 (Lonza, #BE12-719F).

Normal human bronchial epithelial (NHBE) cells from human donors were cultured in BEGM (Lonza,# CC-3171) and grown in monolayers. The cells were used for experiments immediately after reaching confluence. Cells were kindly provided by Dr. Jakwerth.

3.2.3.2 Pharmacological treatments with sheddase inhibitors

Sheddase inhibitors were dissolved in DMSO at a 10 mM stock concentration. Aliquots were stored at – 20°C and always thawed freshly prior to use. Typically, the inhibitors were used at 10 µM (1:1000 in culture media), if not otherwise stated. Similar volume of DMSO was used as the vehicle control.

3.2.3.3 Cell viability assay

To evaluate the impact of pharmacological substances on A549-ACE2 cells, the CyQUANT MTT cell viability assay kit (Thermo Fisher) was employed following the manufacturer's instructions. To summarize, 1×10^4 cells were placed into a 96-well plate. After attachment, the cells were maintained in phenol-free DMEM (Thermo Fisher) containing 5% FBS and concentrations of BB94, DPC-333, apratastat, or DMSO ranging from 0–25 µM, for a period of 48 hours. Inhibitors were diluted to ensure each sample contained a total of 0.25% DMSO.Two days later, cells were rinsed twice with phenol-free DMEM and then incubated in 100 µl of PBS which contained 12 mM MTT (supplied with the kit) for a duration of 4 hours at 37°C. To dissolve the formazan, 100 µl of an SDS-HCL solution (made by dissolving 1 g of SDS in 0.01 M HCl) was added and left to incubate for 18 hours at 37°C. Absorbance was then measured at a wavelength of 570 nm. Calculations were performed as recommended by the manufacturer’s protocol.

3.2.3.4 Isolation of primary microglia

Microglia isolation was performed using a standard operating procedure based on magnetic cell separation (MACS) technology and the neuronal dissociation kit from Miltenyi Biotec (Colombo et al., 2021). Briefly, brains from P4-P9 mouse pups were isolated by decapitation using scissors and forceps. The cerebella were removed and the two hemispheres were carefully separated. Ultra fine forcepses and a stereotactic microscope was used to remove the meninges. The tissue was kept on ice-cold HBSS at all times. Enzyme mixes were diluted and pre-incubated at 37°C for 15 minutes as described by the manufacturer’s protocol. The hemispheres were then chopped into 4-5 small pieces and transferred into a gentleMACS™ C Tube. Enzyme mixes were added and the tissue was dissociated using a standard program (37C_NTDK_1) on the gentleMACS Octo Dissociator. After automatic dissociation, the tissue homogenate was centrifuged for 5 seconds at 300 x g. To further dissociate the tissue, the suspension was passed for 10 times through a fire-polished glass pipette (coated with 4% (w/v) BSA). A 40 µM cell strainer was rinsed with 5 mL HBSS and the suspension was then passed through the strainer to remove undissociated tissue. The cell suspension was cleared by two sequential washing steps by adding 10 mL of HBSS and centrifugation at 300 x g for 10 min. After the first washing step, the cell number was determined using the TC20 Automated Cell Counter from Biorad. After this, cells were resuspended in 90 µl of MACS buffer (PBS containing 0.5 % (w/v) BSA and 5 mM EDTA, sterile filtered) and 10 µl of CD11b Microbeads (Miltenyi Biotec) per 1 x 10^7 cells. After immuno-labelling, the cell suspension is washed by adding 2 mL of MACS buffer and centrifugation (300 x g for 10 min). The supernatant is discarded and cells are resuspended in 1 mL of fresh MACS buffer. The microglial fraction was then isolated by using the MACS columns provided by the kit. The columns were plunged into the MACS Separator (Miltenyi Biotec) and rinsed by adding 3 x 1 mL of MACS buffer to the columns. The cell suspension is then applied to the columns and rinsed 3 x with 1 mL MACS buffer. After this, the columns are removed from the MACS Separator and placed in fresh 15 ml Falcon tubes. To flush out the microglia, the plunger is inserted into the column after 2.5 mL of MACS buffer was added and pressed down until foam formation was observed in the column’s tip. The flushed-out microglia are then centrifuged for 5 min at 300 x g, snap frozen in liquid nitrogen or resuspended in culture media depending on the intention of the experiment.

3.2.3.5 hiSPECS secretome analysis

To analyze the secretome of cultured primary microglia, the high-performance secretome protein enrichment with click sugars (hiSPECS) method was adopted as previously described (Tüshaus et al., 2020) with minor modifications. A point-by-point protocol is attached in Appendix 1. Briefly, heterozygous WT/iR2KO animals at three months old were bred. Their genotypes were subsequently confirmed using PCR. The offspring came from a total of three separate mating pairs, with each pair producing at least one pup of the differing genotype. Microglia were harvested at p9 as described in Chapter 3.2.3.4, achieving a minimum yield of one million cells per brain. These one million CD11b+ microglia were then placed in a six-well plate and cultured for three days. After this period, the culture medium was switched to DMEM/F12 (10% FBS, 1% P/S) containing 50 µM of tetra-acetylated N-azido-mannosamine (ManNAz). The media was collected after 72 and briefly filtered by centrifugation. A lectin-based enrichment was conducted to reduce contaminants and to concentrate the azido-glycoproteins using concanavalin A (ConA) and wheat-germ-agglutinin (WGA). After elution of the azido-glycoproteins, the proteins were bound to magnetic dibenzocyclooctyne (DBCO) beads by means of a so-called click reaction, in which the N-azido-sialic acid that is metabolically incorporated into the glycotress of newly formed proteins becomes covalently attached by means of a triazole moiety (Kuhn et al., 2012). Stringent washing of the magnetically immobilized glycoproteins allowed for contaminant removal. The glycoproteins were then eluted, enzymatically digested with Trypsin and lysC and subjected to SP3 contaminant removal. The cell lysates of microglia from this experiment was harvested and subjected to Western Blotting or whole lysate proteomics, as described in chapter 3.2.6.4 and 3.2.5.2, respectively.

3.2.3.6 Generation of genetically modified A549 cell lines

A549 cells stably expressing human ACE2-HA were kindly provided by Prof. Pichlmair Parental A549 were transduced with pwpI-hACE2-HA-zeo and selected using 300 µg/ml zeocin (Thermo Fisher) over a time period of three weeks. The cells were split when confluence was reached (usually 2-3x per week). ACE2 expression was confirmed in these cells by Western blotting. The A549-ACE2 cells were then used for further genetic manipulation using guides against ADAM10 or ADAM17, as mentioned below:

Guide sequences:

Control guide (NTC, target: non-targetting): 5’-TCCGGAGCTTCTCCAG TCAA-3’

ADAM10 guide 1 (A10 KO1, target: exon 2): 5’-CGTCTAGATTTCCAT GCCCA-3’

ADAM10 guide 2 (A10 KO2, target: exon 3): 5’-GATACCTCTCATATTTACAC-3’

ADAM17 guide 1 (A17 KO1, target: exon exon 1): 5’-GGTCGCGGCGCCAGCACGAA-3’

ADAM17 guide 2 (A17 KO2, target: exon exon 1): 5’-GGTCTTTACCGAGTCTCTGG-3’

The guides were incorporated into the lentiCRISPRv2 vector (Addgene). The guide design and cloning was performed by Dr. S.K. Tschirner as described in comprehensive detail (Jocher et al., 2022).

3.2.3.7 Lentivirus production and antibiotic selection for CRISPR-directed gene knock-out

A549-ACE2 cells were transduced and selected using standard operating procedures as described (Jocher et al., 2022). Briefly, poly-D-lysine (Sigma, 25 µg/ml) was used to coat 10 cm culture dishes overnight at 37°C. These dishes were rinsed twice with PBS. HEK293T cells were then plated at a density of 7 x 10^6 cells per dish to package the CRISPR constructs into the virus. The cells were then allowed to incubate overnight under standard growth conditions, which is 37°C and 5% CO2, in DMEM (10% FBS, 1% P/S). For transfection, 0.9 ml of Optimem was combined with 35.6 µl of Lipofectamine 2000 (Thermo) in one tube, with gentle inversion for mixing. In a separate tube, 0.9 ml of Optimem was mixed with 13.3 and 9 µg of the packaging plasmids pxPAX2 and pcDNA3.1-VSVG, respectively, as well as 18 µg of the CRISPR KO construct in question. These two preparations were then combined and left at room temperature for an hour. One hour before transfection, the medium of the HEK293T cells was replaced with 9 ml of Optimem supplemented with 10% FBS. The transfection mix was subsequently introduced drop-wise into this medium, after which the cells were left to incubate overnight. The following day, the medium was exchanged with 6 ml of DMEM (2% FBS, 1% P/S, 10 mM sodium butyrate). After overnight incubation, the supernatants were subjected to centrifugation at 1000 x g for 10 min. To thoroughly remove cell debris, the supernatants was passed through a 0.45 µm pore-size membrane filter (VWR), using a luer lock syringe to ensure precision. Finally, the purified supernatants were aliquoted and stored at -80°C until use. A549-ACE2 cells were seeded (5 x 10^5) into T25 flasks and incubated overnight under standard growth conditions (37°C, 5% CO_2, DMEM 10% FBS, 1% P/S). The following day, the culture medium was replaced with 1 ml of fresh medium, to which 1 ml of the lentiviral supernatant of the corresponding CRISPR KO construct was added or alternatively, supplemented with 2 ml of fresh medium as a negative control for successful antibiotic selection. Polybrene was then introduced to all cells to achieve a final concentration of 5 µg/ml. After incubation overnight, cells were rinsed twice with PBS and the medium was swapped for 6 ml of standard growth medium supplemented with either 1 µg/ml of puromycin or 500 µg/ml of hygromycin B for selection purposes. Antibiotics were removed once all cells in the negative control were dead. In order to create ADAM10/17 double KO, ADAM17 KO guide 1 cells were seeded in T25 flasks as outlined above and were infected with lentiCRISPRv2 ADAM10 KO construct carrying a resistance cassette for hygromycin instead of puromycin. The successful knockout of the target gene in all resulting cell lines was verified by Western blotting and functionally with ELISA against sAPPa.

3.2.3.8 Syncytia formation assay

The syncytia formation assay was conducted as previously described (Jocher et al., 2022).In brief, HEK293T cells were co-transfected with pcDNA3.1(+)-eGFP and pCG1-SARS-CoV-2-S-HA (graciously provided by Prof. Pöhlmann) using Lipofectamine 2000, in accordance with the instructions provided by the manufacturer. 18 hours post-transfection, the cells were detached using PBS/EDTA (pH 7.5, 1 mM) and layered on top of A549-ACE2, in a 1:1 ratio (4 × 10^4 cells/µ-Slide 8 Well, #80806, Ibidi). Syncytium formation was inhibited by the addition of 10 µM BB94 or DMSO at the time of co-culturing. After a period of 24 hours, the cells were fixed using 4% PFA for 15 minutes at room temperature, followed by staining in a blocking buffer (PBS, 2% NGS, 0.05% saponin). The cells were exposed to an anti-GFP antibody (Fitzgerald, rabbit, 1:500) for 45 minutes at room temperature, rinsed with PBS, and then stained with a secondary antibody (Abcam, 1:400, goat anti-rabbit Alexa Fluor 488), and Hoechst 33342 (Thermo Fisher, 1:2,000) for half an hour at room temperature. The resulting images were captured on a ZEISS LSM 900. Syncytia and nuclei were quantified by assessing the GFP and Hoechst fluorescence through Image J. To adjust for variations in cell density, the area of syncytia was computed in relation to the intensity of the nuclei as follows:

AS.rel by AS.rel = AS.total / IN.mean

AS.total is the total syncytia area and IN.mean represents the average intensity of nuclei. The relative percentage of nuclei within syncytia (PN) was determined using the following equation:

PN = IN.ROI * AN.ROI / IN.mean

ROI is the region of interest, IN.ROI is the intensity of the nuclei in the ROI, AN.ROI is the area of nuclei in the ROI, and IN.mean stands for the mean nuclei intensity.

3.2.3.9 Infection assays using pseudotyped VSV particles

The assays comprising single-round infectious particles were performed by Mrs. Lydia Riepler, MSc, at the Medical University of Innsbruck. The experiments comprising infection of A549-ACE2 cells are described in (Jocher et al., 2022). Results and methods of the infection of the A549-ACE2 KO lines are unpublished and described in comprehensive detail below.

Briefly, the single-round infectious VSVΔG, with GFP acting as the marker gene and pseudotyped with a C-terminally truncated SARS-CoV-2 spike protein (VSV-S), was created as described previously (Riepler et al., 2020). A negative control was established using a VSVΔG virus pseudotyped with the glycoprotein (GP) of the lymphocytic choriomeningitis virus (LCMV), termed VSV-GP.

The day before infection, 1x 10^4 cells were seeded per well in a 96-well plate, each well containing 100 µl of complete medium. On the day of infection, half of the medium (50 µl) was removed from each well and replaced with 50 µl of medium containing inhibitors or DMSO to achieve a final concentration of 10 µM in case of the metalloprotease inhibitors and 5 µM or 1 µM in case of E64d. The DMSO volume was adjusted to reach a final concentration of 0.25% DMSO per well. After incubating for an hour at 37°C, the cells were infected with 50 µl of the relevant virus dilution, achieving roughly 100 infected cells per well. The inhibitors were applied a second time to maintain the concentration with the increased volume.

To inhibit viral infection using recombinant sACE2, the infectious particles were incubated with half-logarithmic dilutions (9 steps, beginning from 2.52 µg) of sACE2 (Thermo Fisher) or the same amounts of BSA for an hour prior to infection. 16 hours post-infection, the infected (i.e., GFP-positive) cells were quantified using an ImmunoSpot S5 analyzer (C.T.L. Europe, Bonn, Germany).

3.2.4 ELISA

3.2.4.1 ACE2

Soluble ACE2 was detected using the DuoSet ELISA kit (R&D) according to the manufacturer's protocol. In brief, A549-ACE2 cells were seeded at 8 x 10^5 cells per 6-well and incubated in DMEM (10% FBS, 1% P/S). The following day, the media was exchanged to DMEM (10% FBS, 1% P/S) containing indicated amounts of metalloprotease inhibitors. The supernatant was collected after 48 hours. PMA (25 ng/ml) was spiked in 3 hours before harvest to induce ADAM17 shedding. The supernatants were centrifuged (3000 x g, 5 min) immediately after harvest. Antibodies and standards were used as recommended. The 48 h culture supernatants were diluted 1:40 in reagent diluent (provided by the kit). Detection was performed as instructed. Calculations were performed using a four-parameter logistic fit curve regression model (myassays.com).

3.2.4.2 sAPPa

The detection of soluble human APPa (sAPPa) was carried out using the sAPPa ELISA detection kit from IBL according to the manufacturer's recommendations (Jocher et al., 2022). Briefly, the A549-ACE2 cells were seeded at a density of 2 x 10^5 cells in 24-well plates and incubated overnight in DMEM (10%FBS, 1% P/S). The next day, the cells were incubated with fresh media containing indicated amounts of inhibitors or DMSO. The supernatant was collected after 48 h, briefly centrifuged (3000 x g, 5 min) to remove cell debris, and then subjected to ELISA.

To detect soluble murine APPa (sAPPa) in culture supernants of primary microglia, the sAPPa ELISA detection kit from IBL was used according to the manufacturer's recommendations. The primary microglia were isolated and cultured as described in chapter 3.2.3.4. The supernatants were collected like for hiSPECS experiments (chapter 3.2.3.5).

The standards and antibodies contained in both human and murine kits were used as recommended. Calculations were performed using a four-parameter logistic fit curve regression model (myassays.com).

3.2.4.3 TREM2

For detection of murine TREM2 in culture supernatants of primary microglia, we adopted a custom-made protocol based on the small spot streptavidin sector GOLD technology (MSD), as previously described (Kleinberger et al., 2014). Briefly, MSD Gold plates pre-coated with streptavidin were incubated in blocking buffer (PBS, 0.05% Tween, 3% BSA) on a horizontal shaker (300 rpm) overnight at 4°C. Blocking buffer was discarded, and the plate was incubated with the biotinylated anti-TREM2 capture antibody (R&D systems, BAF1729). The antibody (stock: 100 µg/ml) was diluted 1:800 in blocking buffer to reach a final concentration of 0.125 µg/ml, and 25 µl per well were incubated for 90 minutes at room temperature on a horizontal shaker (300 rpm). Then, the plates were washed 3x in 200 µl per well washing buffer (PBS, 0.05% Tween). After this, culture supernatants from primary microglia were diluted 1:40 in sample dilution buffer (PBS, 0.05% Tween, 1% BSA, 2 µl/ml protease inhibitor cocktail). 50 µl of diluted samples were added to the wells. A standard curve was performed by a two-fold serial dilution (Standard 1-7: 400 pg/ml – 12.5 pg/ml; Standard 8: 0 pg/ml) of recombinant mTREM2-FC (stock: 200 ng/ml) in PBS. To avoid dimerization of the FC-tagged TREM2, a denaturation buffer (10 µl, 200 mM Tris-HCL pH 6.8, 4% SDS, 40% Glycerol, 2% ß-ME, 50 mM EDTA) was added and the samples were boiled at 95°C for 5 min. The samples were allowed to reach room temperature before dispensing 50 µl of each standard into the wells in duplicates. Samples and standards were incubated for 2 hours at room temperature on a horizontal shaker (300 rpm).The plate was washed as above-mentioned, and 50 µl of a rat anti-TREM2 detection antibody (Sigma Aldrich, clone 5F4) was dispensed into the wells and incubated for 1 hour at room temperature on a horizontal shaker (300 rpm). The antibody (stock: 1 mg/ml) was diluted 1:1000 in blocking buffer. The plate was washed again as before-mentioned, and a goat-anti-rat Sulfo-tag (MSD) secondary antibody was added to the wells. The secondary antibody was diluted 1:1000 in blocking buffer, 25 µl per well were added and incubated for 1 hour at room temperature on a horizontal shaker (300 rpm). Next, the plate was washed 2x with washing buffer and 2x with PBS, before 150 µl of a 1x Read buffer (MSD) was added to the wells. The plate was read using the in-house MSD platform. The MSD platform software was used to determine the levels of TREM2 in the samples of unknown concentration with the help of a four-parameter logistic fit curve regression model.

3.2.4.4 TNFa

For detection of murine sTNFa in culture supernatants, primary microglia were seeded at a density of 1 x 10^6 cells/well in a 6-well plate and cultured in DMEM-F12 (10% FBS, P/S) At DIV3, the media was exchanged to DMEM-F12 (P/S) supplemented with 1 µg/ml LPS or equal volumes of PBS serving as the vehicle control. After 1 h incubation, the media was collected and centrifuged for 5 min at 3000 x g to remove cell debris. TNFa levels were determined in the supernatant using the Mouse TNF-alpha Tissue Culture Kit from MSD according to the manufacturer’s instructions.

For detection of human sTNFa in culture supernatants of U937 cells, the cells were seeded at a density of 2 x 10^5 cells/ well in a 24-well and cultured in RPMI (10% FBS, P/S). U937 cells were differentiated by addition of 25 ng/ml PMA for 24 h. The media was then exchanged to RPMI (P/S), and cells were serum-starved overnight. The cells were then stimulated for 2 h with RPMI containing 100 ng/ml LPS in the presence or absence of either DMSO or 10 µM of DPC-333, BB94, and TAPI-1. TNFa levels were determined in the supernatant using the human TNF-alpha Tissue Culture Kit from MSD according to the manufacturer’s instructions.

3.2.5 Mass spectrometry

3.2.5.1 SP3 contaminant removal

The single-pot, solid-phase-enhanced sample preparation (SP3) technique was utilized to remove contaminants and exchange the liquid matrix. The employed protocol is based on the original protocol from Hughes et al. 2019 with modifications (Hughes et al., 2019). A point-by-point protocol is attached in Appendix 2. The contaminant-free tryptic peptides were resolved in 0.1% FA, briefly sonicated and then subjected to LC-MS/MS, as described in the chapter 3.2.5.3.

3.2.5.2 SP3 for proteomic analysis of whole cell lysate from cultured primary microglia

Microglia were isolated from pups and cultured as described in chapter 3.2.3.4. After media collection for hiSPECS, the cells were washed 2x with PBS, before lysis was conducted using 200 µl of STET lysis buffer, as described in chapter 3.2.3.5. Subsequently, a BCA assay was conducted to determine the protein concentration of the lysate as described in chapter 3.2.6.3. 10 µg of lysate protein was digested with trypsin and lysC. The peptides were prepared for LC-MS analysis using the single-pot, solid-phase-enhanced sample preparation (SP3) technique. The protocol is based on the original protocol from Hughes et al. 2019 with modifications (Hughes et al., 2019) to allow for combined enzymatic digestion, contaminant removal, and elution of the digested peptides. A point-by-point protocol is attached in Appendix 3. The contaminant-free tryptic peptides were resolved in 0.1% FA, briefly sonicated and then subjected to LC-MS, as described in the chapter 3.2.5.3.

3.2.5.3 LC-MS/MS analysis

Samples were analyzed by liquid chromatography-mass spectrometry (LC-MS/MS) employing a nanoElute nanoHPLC system coupled online to a TimsTof pro mass spectrometer (Bruker, Germany). Eight µL per sample were separated on a nanoElute nanoHPLC system equipped with an in-house packed C18 analytical column (30 cm × 75 µm ID, ReproSil-Pur 120 C18-AQ, 1.9 µm, Dr. Maisch GmbH, Germany). The liquid chromatography involved a binary gradient of water (A) and acetonitrile (B), containing 0.1% formic acid, and was implemented at a flow rate of 300 nl/min. The column temperature was kept constant at 50 °C. The gradient for secretome samples was set as follows: 0 min, 2% B; 3.5 min, 5% B; 48 min, 24% B; 59 min, 35% B; 64 min, 60% B. The gradient for lysate samples was configured to: 0 min, 2% B; 2 min, 5% B; 92 min, 24% B; 112 min, 35% B; 121 min, 60% B

Samples were analyzed using DIA parallel accumulation serial fragmentation. For the microglia hiSPECS analysis, one scan cycle induced one MS1 full scan followed by 2 rows of 48 sequential DIA windows with 20 m/z width for peptide fragment ion spectra with an overlap of 1 m/z covering a scan range of 300 to 1200 m/z. The ramp time was set to 166 ms, and six windows were scanned per ramp. This resulted in a total cycle time of 2.8 seconds. For microglia lysates, one scan cycle induced one MS1 full scan followed by 2 rows of 42 sequential DIA windows with 23 m/z width for peptide fragment ion spectra with an overlap of 1 m/z covering a scan range of 350 to 1275 m/z. The ramp time was set to 120 ms, with six windows were scanned per ramp, culminating in a total cycle time of 1.8 seconds.

3.2.5.4 LC-MS/MS data analysis

The analysis of the MS raw data was performed employing DIA-NN software, version 1.81, through a library-free search as mentioned in Demichev, 2020 (Demichev et al., 2020). For this analysis, a canonical Mus musculus database, which encompasses one protein for each gene, was used. This database was procured from UniProt and contained 21,966 entries as of the download date on April 9, 2021. Trypsin was defined as a protease with cleavage specificity for C-terminal of K and R. Variable modifications included acetylation at the N-termini of proteins and oxidation of methionines, while carbamidomethylation of cysteines was set as a fixed modification. The software automatically adjusted the mass tolerances for peptide and fragment ions, along with ion mobility tolerances. The analysis permitted two missed cleavages. The False Discovery Rate (FDR) was set at 1% for both proteins and peptides. For quantification purposes, only unique and razor peptides were chosen.

3.2.5.5 Statistical data analysis and visualization of proteomic data

The statistical data analysis of the DIA-NN output was performed with the software Perseus Version 1.6.14.0 (Tyanova et al., 2016) and volcano plots were generated using a custom-made python script (provided by Dr. S.K. Tschirner) in Python 3.9 and the with help of the following packages: pandas 1.1.5, numpy 1.19.4, scipy 1.8.1, seaborn 0.11.1 and matplotlib 3.3.3. Permutation-based FDR threshold curves were generated in and imported from Perseus. Curve parameters are as follows: 250 randomizations, FDR significance threshold = 0.05, s0 = 0.1. Log_2 intensity fold changes and $-\log_{10}$ p-values were calculated by the Python script for all proteins (or protein groups) that were detected in a defined minimum number of samples per condition (5/6 in each group for lysate proteomics, 3/6 in each group for hiSPECS). Only LFQ intensities from protein groups with at least two peptides were considered.

3.2.6 Protein biochemistry

3.2.6.1 Cell lysis for protein extraction

Cell lysis for standard protein analysis using Western blotting or whole lysate mass spectrometry-based proteomics was conducted as follows, if not specifically indicated otherwise. Cells were washed 2x with PBS to remove any residual cell culture media, and then STET lysis buffer (50 mM Tris, 150 mM NaCl, 2 mM EDTA, 1% Triton, pH 7.5) containing 2 µl/ml (1:500) protease inhibitor (PI) cocktail (Sigma Aldrich) and additionally 5 µM of GI254023X (GI) and 10 mM of 1,10-phenanthroline to block the post-lysis autoproteolytic cleavage of ADAM10 and ADAM17, respectively (Brummer et al., 2018) (Schlöndorff et al., 2000). The quantity of STET lysis buffer used for cell lysis varied depending on the experimental setup. As a rule of thumb, 200 µl of STET lysis buffer was used to lyse 1 x 10^6 cells. The volume was accordingly adjusted in line with the varying experimental conditions.

3.2.6.2 Qubit Assay

Determination of digested peptides for subsequent LC-MS/MS analysis was performed using the Qubit assay kit according to the manufacturer’s protocol. Briefly, the protein reagent was diluted 1:200 with protein buffer (both provided by the kit), and then each of the three standard solutions (provided by the kit) were diluted 1:20 in reagent buffer mix to a final volume of 200 µl. The digested peptides were diluted 1:200 in protein reagent buffer mix. Concentration of peptides was determined using the Qubit 3 Fluorometer (Invitrogen) at 562 nm.

3.2.6.3 Bicinchoninic acid (BCA) assay

Cell lysis for standard protein analysis using Western blotting or whole lysate mass spectrometry-based proteomics was conducted as follows, if not specifically indicated otherwise. Cells were washed 2x with PBS to remove any residual cell culture media, and then STET lysis buffer (50 mM Tris, 150 mM NaCl, 2 mM EDTA, 1% Triton, pH 7.5) containing 2 µl/ml (1:500) protease inhibitor (PI) cocktail (Sigma Aldrich) and additionally 5 µM of GI254023X (GI) and 10 mM of 1,10-phenanthroline to block the post-lysis autoproteolytic cleavage of ADAM10 and ADAM17, respectively (Brummer et al., 2018) (Schlöndorff et al., 2000). The quantity of STET lysis buffer used for cell lysis varied depending on the experimental setup. As a rule of thumb, 200 µl of STET lysis buffer was used to lyse 1 x 10^6 cells. The volume was accordingly adjusted in line with the varying experimental conditions.

To determine the concentration of proteins present in blood plasma, we performed a BCA assay using the Pierce™ BCA Protein Assay (Thermo Fisher) according to the manufacturer's protocol. Briefly, BSA was serially diluted in STET lysis buffer (50 mM Tris, 150 mM NaCl, 2 mM EDTA, 1% Triton, pH 7.5) to establish a standard curve ranging from 0 – 2 mg/mL. The standards and samples were pipetted in duplicates (10 µl per well) into a 96-well plate (Thermo Fisher) and incubated in kit reagent A and B for 30 min at 37°C. The spectrophotometric absorbance was determined at 562 nm using the Tecan Infinite M200 Nanoquant. The Tecan software was used to calculate the standard curve and sample concentration.

3.2.6.4 Western blotting

Western blot analysis was conducted using standard operating procedures. Briefly, equal amounts of protein, as determined by the BCA assay (see chapter 3.2.6.3), was diluted in 4x Laemmli buffer (8% SDS, 40% Glycerol, 0.025% Bromophenol blue, 10% ß-Mercaptoethanol ,125 mM Tris, pH 6.8) and boiled for 5 min at 95°C. Samples were run under reducing conditions, if not otherwise stated. To ensure detection of iRHOM2, boiling of the samples was omitted. Polyacrylamid gels for gel electrophoresis (PAGE) contained 8 – 14% acrylamide depending on the intention of the experiment. Gels were run in a Mini-PROTEAN tetra vertical electrophoresis cell (Biorad) containing 1x-SDS-running buffer (25 mM Tris, 240 mM Glycin, 0.1% (w/v) SDS). Voltage was shifted from constant 80 V to 130 V as soon as proteins have migrated through the stacking gel. The running was typically stopped once the loading front ran out of the gel. The separated proteins on the polyacrylamide gels were then transferred onto 0.2 µM nitrocellulose membranes using the Trans-Blot Turbo system from Biorad according to the manufacturer's instructions. After the transfer, the membranes were blocked for 1 h in blocking buffer (PBS-T, PBS containing 1% (v/v) Tween and 5% (w/v) skim milk powder). Then, membranes were incubated with the primary antibody at 4°C overnight on a horizontal shaker. The primary antibodies and respective dilutions are listed in Table 1. If not otherwise indicated, the primary antibody was prepared as followed: 0.5 mL of 5% BSA was diluted in 9.5 mL PBS-T. Then 10 µl of the undiluted primary antibody and 50 µl of a 10% (w/v) sodium azide solution was added. After this, the membranes were washed three times in washing buffer (PBS-T). Next, the membrane was incubated with the secondary antibody for 45 min on a horizontal shaker at room temperature. The secondary antibodies are listed in Table 1. If not otherwise indicated, the secondary antibody was prepared as followed: 0.5 mL of 5% BSA was diluted in 9.5 mL PBS-T. Then 1 µl of the undiluted secondary antibody was added. Membranes were washed again three times with PBS-T. For detection, ECL reagents were prepared and incubated as recommended by the manufacturer. Images were recorded using the ImageQuant LAS 4000 platform. Subsequently, images were cropped, and brightness and contrast was adjusted using Photoshop (version 12.1). Densitometric quantifications were performed using Fiji (ImageJ 2.0.0-rc-67/1.52c).

3.2.6.5 PNGase F digest and TCA precipitation

To achieve better separation of the pro and mature forms of ADAM17 with western blotting, the cell lysate was digested with PNGase F (NEB), which was followed by a trichloroacetic acid precipitation (TCA) to reduce input volumes for SDS-PAGE. Briefly, the concentration of the samples by adding STET lysis buffer including PI and 1,10-phenanthroline (as described in chapter 3.2.6.1) to the least concentrated sample. 10 µg of input material, to which 10x denaturation buffer (provided by the kit) and STET buffer to achieve a final 1x concentration of the denaturation buffer, typically in a total volume of 70-80 µl. The samples were then boiled at 99°C for 10 minutes. To complete the digestion process, we added Glyco buffer 2, NP-40, and PNGase F (all contained in the kit) to reach a final volume of 110 µl. The samples were then digested at 37°C for 1 hour before proceeding with TCA precipitation.

To precipitate proteins with TCA, first water was added to the samples to achieve a total volume of 600 µl. Then 100 µl of 70% TCA was added, mixed thoroughly, and chilled on ice for 30 minutes. The samples were then centrifuged at 21000 x g for 30 minutes at 4°C, and the TCA was quantitatively removed. The resulting pellets were washed twice with 1 ml of 100% ice-cold acetone, each wash followed by centrifugation at 21000 x g for 20 minutes at 4°C. After removing the supernatant completely, the pellets were dried with an open lid at 50°C until all the liquid was fully evaporated. Finally, the pellets were resuspended in 1x sample buffer diluted in STET-lysis-buffer, boiled at 95°C for 5 minutes, and then subjected to a 8% SDS-PAGE.

3.2.6.6 Membrane fractionation

To detect TREM2 in primary microglia, a membrane fractionation protocol was adopted from previously reported protocol (Kleinberger et al., 2014). Primary microglia were isolated and cultured as described in chapter 3.2.3.4. After media was collected for hiSPECS or ELISA, the cells were washed twice with cold PBS. After washing, the cells were harvested in 1 ml of icecold PBS by scraping the cells and transferring them to a new Eppendorf tube. All work was conducted on ice or centrifugation at 4°C. The cells were then spun in a tabletop centrifuge for 5 minutes at 4600 rpm. After this, the supernatant was aspirated and the cell pellet was resuspended in 200 µl of hypotonic buffer (10 mM Tris-HCL pH 7.4, 1 mM EDTA pH 8, 1 mM EGTA pH 8).

The cells in hypotonic buffer were then incubated on ice for 30 minutes. Cells were vortexed every 10 minutes. The samples were then snap frozen in liquid nitrogen. After the freezing step, samples were slowly thawed on ice. This was followed by another centrifugation step, this time for 45 minutes at 13000 rpm. The supernatant was then collected, representative of the cytosolic fraction of the cells.The remaining pellet was dissolved using 100 µl of STE(N)-lysis buffer (50 mM Tris-HCL pH 7.6, 150 mM NaCl, 2 mM EDTA pH 8, 1% TX-100). The pellet was thoroughly dissolved by pipetting up and down several times.The samples were incubated for 20 minutes on ice before a final centrifugation was performed for 20 minutes at 13000 rpm. The supernatant, now representing the membrane fraction of the cells was collected in separate tubes and a BCA assay (chapter 3.2.6.3) was performed to determine the protein concentration.

3.2.6.7 In vitro cleavage assay of SARS-CoV-2 spike protein

The in vitro cleavage of spike protein was performed as previously described (Jocher et al., 2022). Briefly, recombinant spike protein (SinoBiologicals) was subjected to a 24-hour incubation at 37°C with 1 µg of recombinant ADAM17 (Enzo Life Sciences), ADAM10 (R&D), or TMPRSS2 (LSBio) at a 1:1 ratio. The activity of ADAM proteases was ensured in a 25 mM Tris buffer containing 2.5 µM ZnCl2, 0.005% Brij-35 (w/v), at a pH of 9.0. In the case of TMPRSS2, reactions were carried out in a 50 mM Tris buffer with 0.2% Triton X-100, 50 mM NaCl, at a pH of 7.5. To inhibit ADAMs and TMPRSS2, proteases were treated with BB94 (10 µM) or camostat mesylate (100 µM), respectively, for a duration of 5 minutes prior to the addition of spike protein. Subsequently, the samples were heated to 95°C for 5 minutes in a 2x Laemmli buffer and then subjected to 8% SDS-PAGE. The cleavage fragments were detected by Western blotting using an anti-His-tag (Clone 3D5, kind gift of Dr. R. Feederle) antibody.

3.2.7 Bulk transcriptomic analysis of primary microglia

3.2.7.1 Microglia isolation, RNA isolation, quality control and Nanostring analysis

Primary microglia were isolated from adult (22-weeks) *Wildtype* and *iRhom2*$^{-/-}$ animals using magnetic cell separation as described before (Chapter 3.2.3.4). Total RNAs were extracted using miRNeasy kit (Qiagen) according to the manufacturer's instructions. All RNA samples had initial RNA Integrity (RIN) scores above 7.0 as determined using the Eukaryote Total RNA Nano Series II assay on the Aglient 2100 Bioanalyzer. The cDNA conversion was performed by reverse transcription and a multiplexed target enrichment of 13 RNA samples (6x WT, 7xKO) was performed. The RNA levels of a customized codeset containing 235 mRNAs (Table 4) were analyzed using the Nanostring technology. The Nanostring analysis was conducted at Proteros (Martinsried, Munich). Briefly, the Nanostring technology quantified gene expression levels by employing molecular colour-coded barcodes. This process involved the use of two distinct 50 base pair mRNA probes, a capture probe and a reporter probe, which were added to the sample. These probes bound to the mRNA molecules present in the sample through hybridization. The reporter probe, which carried the molecular colour-coded barcodes, bound to the barcode, while the capture probe bound to biotin. This binding allowed the complex to be immobilized to magnetic beads, which enabled purification and subsequent data collection. Each sample was combined with the capture and reporter probes, and this mixture was loaded into the nCounter cartridge. This cartridge was then transferred into the nCounter SPRINT™ machine. The preparation and measurement of the sample adhered to the guidelines supplied with the instrument. Each measurement included the running of negative and positive controls, which were utilized for data normalization.

3.2.7.2 Data pre-processing and normalization

While all the replicates of the samples in the experiment had no missing data, we neither imputed nor performed any data pre-selection criterion. Consequently, all genes (a total of 235) were incorporated into the differential gene expression analysis. The normalization of data prior to differential expression analysis was performed using the same procedure as that implemented by Wang et al. 2016 (Wang et al., 2016), whose advantage is its specificity to nCounter data. The data normalization process considered the positive controls, negative controls and the housekeeping genes embedded within the nCounter technology. Principal component analysis was run to visualize the relationships between the samples.

3.2.7.3 Differential expression analysis and statistics

The comparison of gene expression between the WT and KO mice was facilitated through the use of the edgeR package in R, which enabled pairwise comparisons of the experimental conditions (Robinson et al., 2010). A generalised linear model, paired with a likelihood test (implemented in the R package edgeR), was employed for the detection of differentially expressed genes (based on count data) between the experimental conditions, as previously described (Schiffman et al., 2018). A gene was considered differentially expressed if the Bonferroni corrected p-value was less than 0.05. All statistical analyses were conducted in the R environment. The determination of the extent of gene differential expression between the experimental conditions was accomplished using a moderated t-test, coupled with empirical Bayes in edgeR.

Table 4 Customized gene list for Nanostring analysis.

Probe Name	Accession #	Probe Name	Accession #	Probe Name	Accession #
Adam17	NM_001277266.1	F11r	NM_172647.2	P2ry6	NM_183168.2
Abcc3	NM_029600.3	Fabp5	NM_010634.3	Pgrmc1	NM_016783.3
Abhd12	NM_024465.3	Fads1	NM_146094.2	Pik3r4	NM_001081309.1
Abi1	NM_001077190.1	Fcrls	NM_030707.3	Pla2g15	NM_133792.2
Abi3	NM_001163464.1	Fgd2	NM_001159538.1	Plcg2	NM_172285.1
Adamts1	NM_009621.4	Fgr	NM_010208.4	Pld3	NM_011116.1
Ak1	NM_001198790.1	Frmd4a	NM_001177843.1	Plxdc2	NM_026162.5
Ank	NM_020332.4	Fscn1	NM_007984.2	Pmepa1	NM_022995.3
Anxa5	NM_009673.2	Fth1	NM_010239.1	Pparg	NM_011146.1
Apbb2	NM_009686.1	Fxyd5	NM_008761.3	Pros1	NM_011173.2
Aplp2	NM_009691.2	Gab1	NM_001301298.1	Psd	NM_028627.2
Apoe	NM_001305844.1	Gal3st4	NM_001033416.2	Ptgfrn	NM_011197.3

Arg1	NM_007482.3	Garnl3	NM_178888.4	Ptgs1	NM_008969.3
Atf3	NM_007498.3	Gas6	NM_019521.2	Ptms	NM_026988.2
Axl	NM_009465.3	Gbgt1	NM_139197.2	Ptprm	NM_008984.2
B2m	NM_009735.3	Gcnt2	NM_008105.2	RHBDF1	NM_010117.2
B4galt4	NM_019804.3	Glul	NM_008131.3	RHBDF2	NM_001167680.1
Bach1	NM_007520.2	Gnas	NM_010309.3	Rab6b	NM_173781.4
Basp1	NM_027395.2	Golm1	NM_001035122.2	Rap1gds1	NM_001040690.1
Bin1	NM_001083334.1	Gp9	NM_018762.1	Rap2b	NM_028712.4
C1qa	NM_007572.2	Gpr165	NM_029536.3	Rapgef5	NM_175930.5
C1qb	NM_009777.2	Gpr34	NM_011823.4	Rasal3	NM_178785.3
C1qc	NM_007574.2	Grap	NM_027817.3	Rgmb	NM_178615.3
C3	XM_011246258.1	Grn	NM_008175.3	Rgs1	NM_015811.1
C3ar1	NM_009779.2	Gtf2h2	NM_022011.4	Rhob	NM_007483.2
C5ar2	NM_001146005.1	Gusb	NM_010368.1	Sall1	NM_021390.3
Cables1	NM_001146287.1	H2-D1	NM_010380.3	Sall3	NM_178280.3
Cadm1	NM_207675.2	Hexb	NM_010422.2	Selplg	NM_009151.3
Camk2n1	NM_025451.2	Hif1a	NM_010431.2	Sema4d	NM_013660.3
Capg	NM_007599.3	Hist1h2ab	NM_175660.3	Serinc3	NM_012032.4
Capn3	NM_001109761.1	Hpgds	NM_019455.4	Serpine2	NM_009255.2
Cbr1	NM_007620.2	Hps4	NM_138646.3	Serpinf1	NM_011340.3
Ccl2	NM_011333.3	Hspa1a	NM_010479.2	Sesn1	NM_001013370.2
Ccl3	NM_011337.1	Icam1	NM_010493.2	Siglech	NM_178706.4
Ccl4	NM_013652.1	Igf1	NM_001111274.1	Slc2a5	NM_019741.3
Ccl6	NM_009139.2	Il10	NM_010548.1	Slc7a8	NM_016972.2
Ccnd1	NM_007631.1	Il10ra	NM_008348.2	Slco2b1	NM_175316.3
Ccr5	NM_009917.5	Il1b	NM_008361.3	Slco4a1	NM_148933.1
Cd300lb	NM_199221.2	Il6st	NM_010560.2	Smad1	NM_008539.3
Cd34	NM_001111059.1	Inpp4b	NM_001024617.2	Smad3	NM_016769.3
Cd52	NM_013706.2	Inpp5d	NM_001110192.1	Snn	NM_009223.3
Cd63	NM_001042580.1	Itga6	NM_008397.3	Sparc	NM_009242.4
Cd68	NM_009853.1	Itgax	NM_021334.2	Spata13	XM_901902.2
Cd83	NM_009856.2	Itgb5	NM_001145884.1	Spp1	NM_009263.3
Cd9	NM_007657.3	Jun	NM_010591.2	Spry1	NM_011896.2
Cebpb	NM_009883.3	Kcnd1	NM_008423.1	St3gal6	NM_018784.2
Ch25h	NM_009890.1	Kdr	NM_010612.2	Stab1	NM_138672.2
Ckb	NM_021273.4	Khdrbs3	NM_010158.2	Syngr1	NM_009303.2

Clec7a	NM_020008.2	Klhl38	NM_177755.3	Tanc2	NM_181071.3
Clic4	NM_013885.2	Lair1	NM_001113474.1	Tgfb1	NM_011577.1
Cmklr1	NM_008153.3	Ldlrad4	NM_172631.3	Tgfbr1	NM_009370.2
Crybb1	NM_023695.2	Lgals3	NM_001145953.1	Tgfbr2	NM_009371.2
Csf1	NM_001113530.1	Lgals3bp	NM_011150.2	Timp2	NM_011594.3
Csf1r	NM_001037859.1	Lgmn	NM_011175.3	Tjp1	NM_009386.1
Csf3r	NM_001252651.1	Lilrb4a	NM_013532.2	Tmem100	NM_026433.2
Csmd3	NM_001081391.2	Limk1	NM_010717.2	Tmem119	NM_146162.2
Cst3	NM_009976.3	Lpl	NM_008509.2	Tnf	NM_013693.2
Cst7	NM_009977.3	Lrrc3	NM_145152.4	Tnfrsf11a	NM_009399.3
Cstb	NM_007793.3	Lrrc8a	NM_177725.4	Trem2	NM_031254.2
Ctsa	NM_001038492.2	Ly9	NM_008534.2	Tspan7	NM_019634.2
Ctsb	NM_007798.2	Ly96	NM_016923.1	Tspo	NM_009775.4
Ctsd	NM_009983.2	Lyz2	NM_017372.3	Ttr	NM_013697.4
Ctsl	NM_009984.3	Mafb	NM_010658.2	Txnip	NM_023719.1
Ctss	NM_021281.2	Mecp2	NM_010788.2	Tyrobp	NM_011662.2
Ctsz	NM_022325.4	Mef2a	NM_001033713.1	Upk1b	NM_178924.4
Cx3cr1	NM_009987.3	Mef2c	NM_001170537.1	Usp2	NM_016808.2
Cxcl16	NM_023158.6	Mertk	NM_008587.1	Vegfa	NM_001025250.3
Cxxc5	NM_133687.2	Myo1b	NM_010863.2	Zfp691	NM_001145935.1
Cybb	NM_007807.2	Nav2	NM_175272.3	Calr	NM_007591.3
Dnajb4	NM_027287.3	Nos2	NM_010927.3	Cltc	NM_001003908.1
Dst	NM_010081.2	Npl	NM_028749.1	Gapdh	NM_001001303.1
Ecscr	NM_001033141.1	Nrip1	NM_173440.2	Hprt	NM_013556.2
Egr1	NM_007913.5	Nuak1	NM_001004363.1	Hsp90b1	NM_011631.1
Eng	NM_001146350.1	Olfml2b	NM_177068.4	Hspa5	NM_022310.2
Entpd1	NM_009848.3	Olfml3	NM_133859.2	Lrp1	NM_008512.2
Epb41l2	NM_001199265.1	Olfr110	NM_146328.2	Pgk1	NM_008828.2
Eps15l1	NM_001122832.1	Olfr920	NM_146787.2	Tubb5	NM_011655.4
Etv5	NM_023794.2	P2ry12	NM_027571.3		
Extl3	NM_018788.3	P2ry13	NM_028808.3		

4 RESULTS

4.1 Part I: The role of the Alzheimer’s disease risk gene *iRhom2* in microglia

To establish a causal connection between methylation patterns in the iRhom2 promoter and an increased risk for Alzheimer's disease, it is crucial to obtain a thorough understanding of iRHOM2 function. The initial steps in advancing our knowledge of iRHOM2/ADAM17 regulation of AD-linked substrates involve characterizing the fundamental aspects of this complex shedding machinery. This process is explored in detail in Part I of this thesis.

4.1.1 Biochemical characterization of *iRhom2* in murine microglia

Microglia are the only iRHOM2-expressing cells in the murine brain (Sjöstedt et al., 2020) and iRHOM2 is the established regulator of ADAM17 in myeloid cells (Adrain et al., 2012; Li et al., 2015; McIlwain et al., 2012b), suggesting that iRHOM2 may influence microglial function. To explore the role of iRHOM2 in microglia, we isolated primary microglia (pMG) from mouse pups (P9) using magnetic-activated cell sorting (MACS) technology. This method relies on the specific labeling of microglia with magnetic anti-CD11b microbeads (Fig. 7A). MACS enabled the isolation of a highly pure microglial fraction, while the remaining brain cell types were collected in the flow-through fraction, as evidenced by the presence of the astrocyte marker GFAP, the oligodendrocyte marker CNPase, and neuron-specific ß-III-TUBULIN. The microglia-specific marker IBA1 was only detected in the magnetically retained fraction (Fig. 7B).

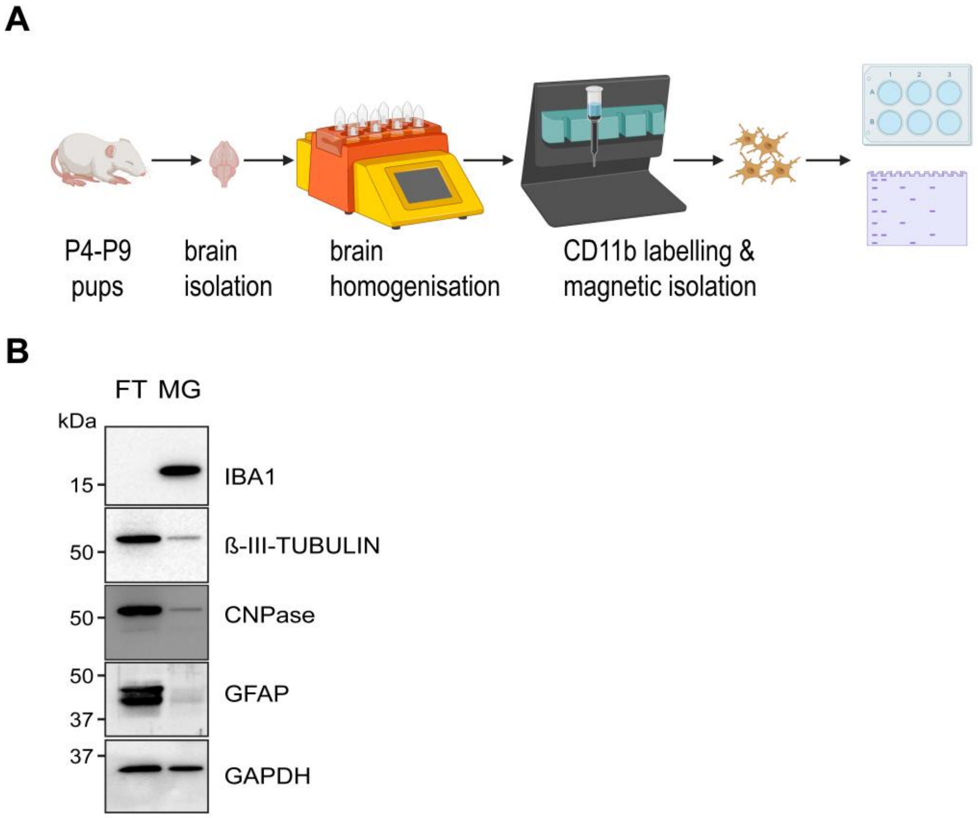

Figure 7: Isolation of microglial cells from postnatal (P) mouse brains. A) Schematic Illustration of the isolation procedure. Mouse brains (P4 – P9) are dissected, and cortices are enzymatically homogenized. Microglial cells are labelled by anti-CD11b coated magnetic beads and then passed through a magnetic separation column. The isolated microglia are then utilized for further biochemical analyses. B) Western blot analysis of fractionated brain cells. The microglia-depleted flow-through (FT) fraction consists of cells positive for GFAP (astrocytes), ß-III-TUBULIN (neurons), and CNPase (oligodendrocytes), while the microglia fraction (MG) is marked by the presence of IBA1. This confirms the successful isolation of a highly pure microglia fraction from postnatal mouse brains.

We further utilized MACS to isolate pMG from both *Wildtype* and *iRhom2*$^{-/-}$ mouse brains. As shown in Fig.8A, iRHOM2 was readily detectable at 100 kDa in *Wildtype* pMG, but was absent in *iRhom2*$^{-/-}$ pMG. Further, we examined the band pattern of ADAM17 in these cells to assess the status of the catalytically active part of ADAM17 in *iRhom2*$^{-/-}$ microglia. To better distinguish between the pro and mature forms of ADAM17, we removed the N-linked sugars using PNGase F and detected mature-ADAM17 slightly above 75 kDa in pMG and mouse embryonic fibroblasts (MEFs). Loss of *iRhom2* abrogated ADAM17 maturation, while leaving pro-ADAM17 unaffected, confirming the established role of iRHOM2 in the ER-to-Golgi shuttling of ADAM17 in pMG (Fig. 8B). The same effect was observed in MEFs, when both *iRhom2* and *iRhom1* were knocked out (Fig. 8C). To address the proteolytic activity of ADAM17 in *iRhom2 -/-* pMG, we stimulated pMG with LPS for 1 hour and checked for the release of soluble TNFa in the supernatants of these cells. As expected, LPS rapidly induced TNFa shedding in *Wildtype* pMG, but not *iRhom2*$^{-/-}$ pMG. Together, these data demonstrate that *iRhom2* knock-out parallels *Adam17* loss of function.

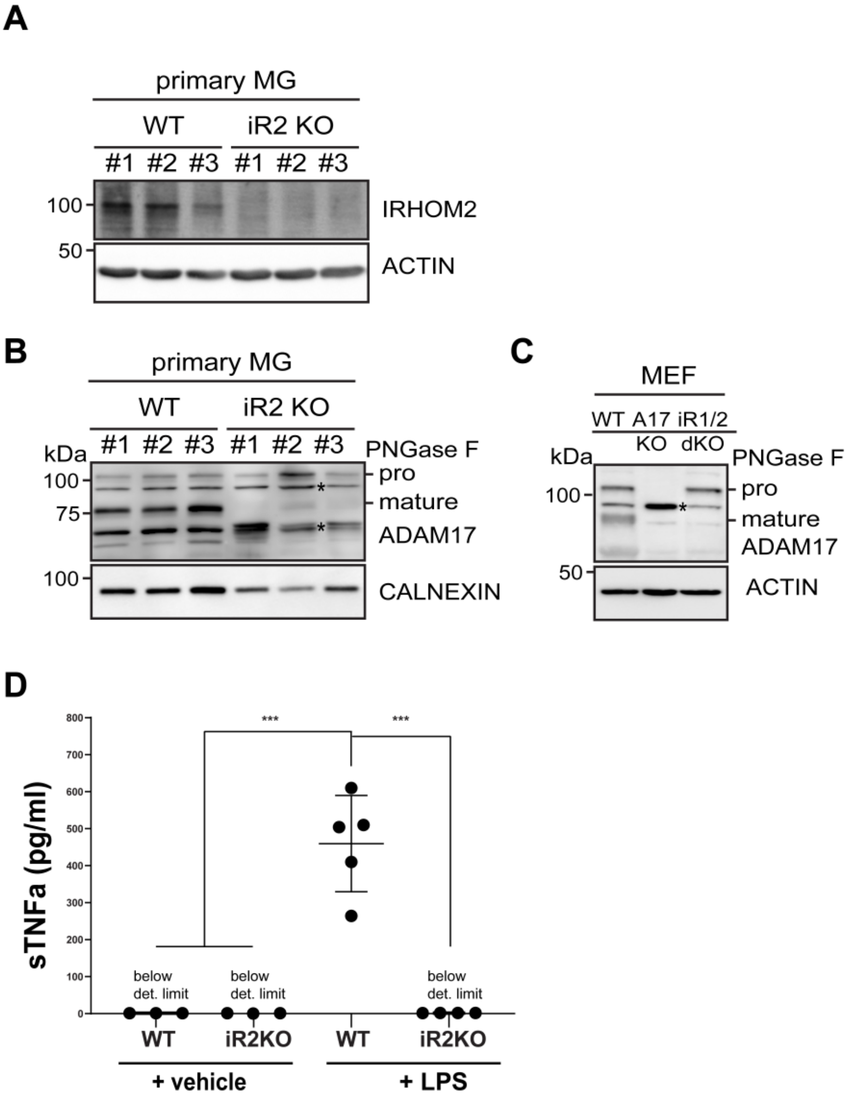

Figure 8: Characterization of primary microglia (MG) from *Wildtype* (WT) or *iRhom2*$^{-/-}$ (iR2KO) mice. A) Western blot analysis shows iRHOM2 at 100 kDa in WT, but absent in iRhom2 -/- MG. Three biological replicates per genotype are shown. ACTIN serves as a loading control. B-C) Western blot analyses of ADAM17 in MG (B) or in mouse embryonic fibroblasts (MEF) (C). Lysates were treated with PNGase F to separate the pro and mature forms of ADAM17. The pro form of ADAM17 appears slightly above 100 kDa, while the mature form appears at 75 kDa. In MG (B), knock-out of iRHOM2 leads to depletion of mature ADAM17. Calnexin serves as a loading control. Three biological replicates per genotype are shown. In MEF cells (C), IRHOM1 and iRHOM2 double knock-out (dKO) results in impaired ADAM17

maturation. ACTIN serves as a loading control. * Asterisks indicate nonspecific bands. D) Functional analysis of ADAM17 activity in WT or iRhom2$^{-/-}$ MG. Cultured MG were stimulated with 1 µg/mL LPS for 1 hour. Release of soluble TNFa was quantified by ELISA. One-way ANOVA with Tukey's correction for multiple comparisons. Data are represented as mean ± SD originating from at least three biological replicates. $^{*}p < 0.05$, $^{**}p < 0.01$, $^{***}p < 0.001$.

4.1.2 Transcriptomic and proteomic characterization of *iRhom2*$^{-/-}$ microglia

Microglia are characterized by the occurrence of different activation states, which are integral to their physiological function (Paolicelli et al., 2022). It was therefore conceivable that functional loss of ADAM17 directly impacts microglial activity. To verify this hypothesis, we isolated RNA of acutely isolated *Wildtype* and *iRhom2*$^{-/-}$ pMG to compare their transcriptional profile. We interrogated 235 different genes of interest using NANOSTRING technology. The selected genes are known markers of homeostatic microglia and disease-associated microglia (DAM), as well as transcription factors mediating transitory states (see Table 4). By pairwise comparison of microglial gene expression, we found profound upregulation of microglial activation markers and regulators of immune responses such as *Clec7a*, *Itgax*, *Ly9*, *Jun*, and *IL1b*, while others such as *Tspo*, *Cd63*, *Ccl4*, *Lpl*, and *H2-D1* were modestly increased, hinting towards a possible disease-associated phenotype (Fig. 9).

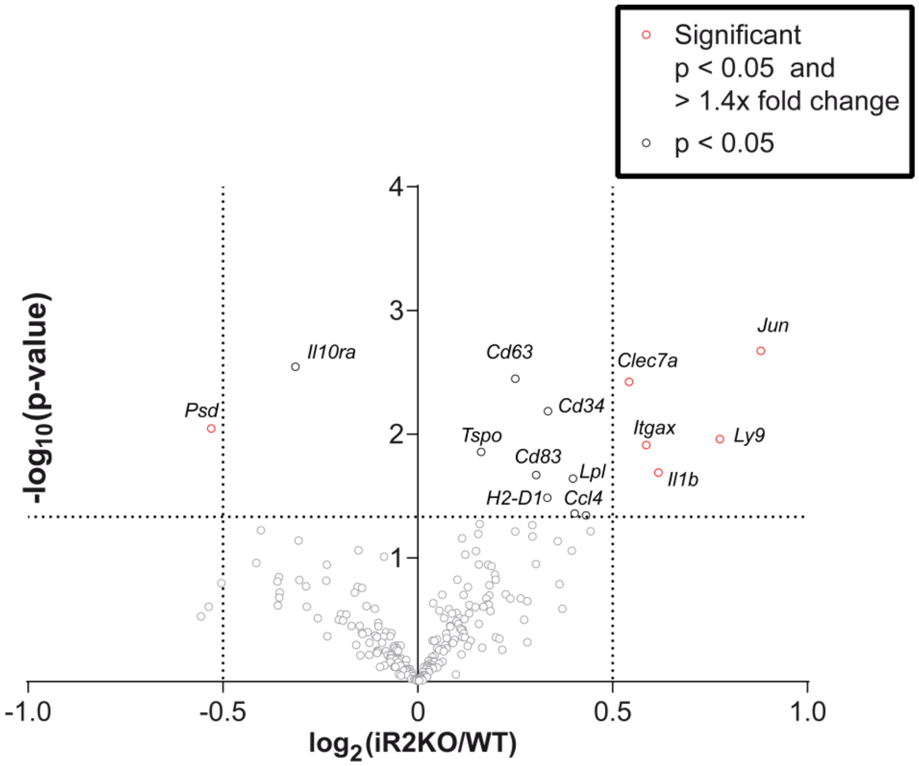

Figure 9: Quantitative Nanostring nCounter mRNA analysis of microglial gene expression. The volcano plot depicts mRNA changes in acutely isolated microglia from adult iR2KO mice in comparison to the WT. The $\log_2$ fold change is plotted against the Bonferroni-corrected p-value ($-\log_{10}$). The dotted line at y = 1.3 separates genes with a p-value < 0.05. Genes were considered significantly changed when the fold change was > 1.4 and p-value < 0.05 (plotted as red circles). Data derived from 8 biological replicates per genotype.

Transcriptional profiles can assess expression of certain genes and offer preliminary insights into the potential functional state of the microglia, but they do not provide detailed mechanistic understanding, nor do they inform about protein isoforms generated by ectodomain shedding. Since iRHOM2/ADAM17 is regulating ectodomain shedding of membrane proteins, major phenotypes upon loss of function are therefore more likely to be detected on protein level, specifically in the secretome. Thus, we adopted high-performance secretome protein enrichment with click sugars (hiSPECS), which had previously been used to successfully identify substrates of shedding proteases (Kuhn et al., 2016; Tüshaus et al., 2020; Tüshaus et al., 2021).

For hiSPECS analysis, primary microglia were metabolically labeled with a chemically-modified azide sugar, which is incorporated into newly synthesized N-glycosylated proteins. This modification facilitates the cultivation of pMG amidst abundant serum proteins, like albumin, necessary for their survival. Simultaneously, this modification enables the precise extraction of cell-derived secretome proteins, which are typically less abundant, from the conditioned medium, preparing them for subsequent analysis via label-free quantification (LFQ) by mass spectrometry (Fig. 10A). A liquid chromatography-tandem mass spectrometry (LC/MS-MS) analysis with a gradient of 70 min was used to determine the secretome on a Bruker timsTOF Pro using DIA-PASEF (data-independent acquisition coupled with parallel accumulation-serial fragmentation) (Meier et al., 2020). For subsequent DIA-MS data processing, we employed the fully automated DIA-NN pipeline. This software harnesses the power of deep neural networks and innovative signal correction approaches to ensure comprehensive proteome coverage (Demichev et al., 2020). We used 1 million microglia isolated from single pups (P9) of *iRhom2*$^{+/+}$ or *iRhom2*$^{-/-}$ mice and determined the secretome of the conditioned supernatant. In total, we quantified 2263 proteins in at least 3 out of 6 biological replicates in each group, of which 25% were annotated as glycoproteins according to UniProt (Fig. 10B).

Potential iRHOM2/ADAM17 targets are likely to be found among groups annotated as single-pass transmembrane (TM) or GPI-anchored proteins (GPI), as these categories of proteins are well-known to undergo ectodomain shedding (Fig. 10B, C). Among the identified TM and GPI proteins (225 in total), several potential iRHOM2/ADAM17 substrates had significantly reduced ectodomain abundance in the microglial *iRhom2*$^{-/-}$ secretome (Fig. 10D) including CSF1R, H2-L, H2-K1, and TREM2, a major risk factor for Alzheimer’s disease. The ectodomain of ADAM17 was also significantly reduced in the *iRhom2*$^{-/-}$ secretome, confirming the important role of iRHOM2 in ADAM17 maturation.

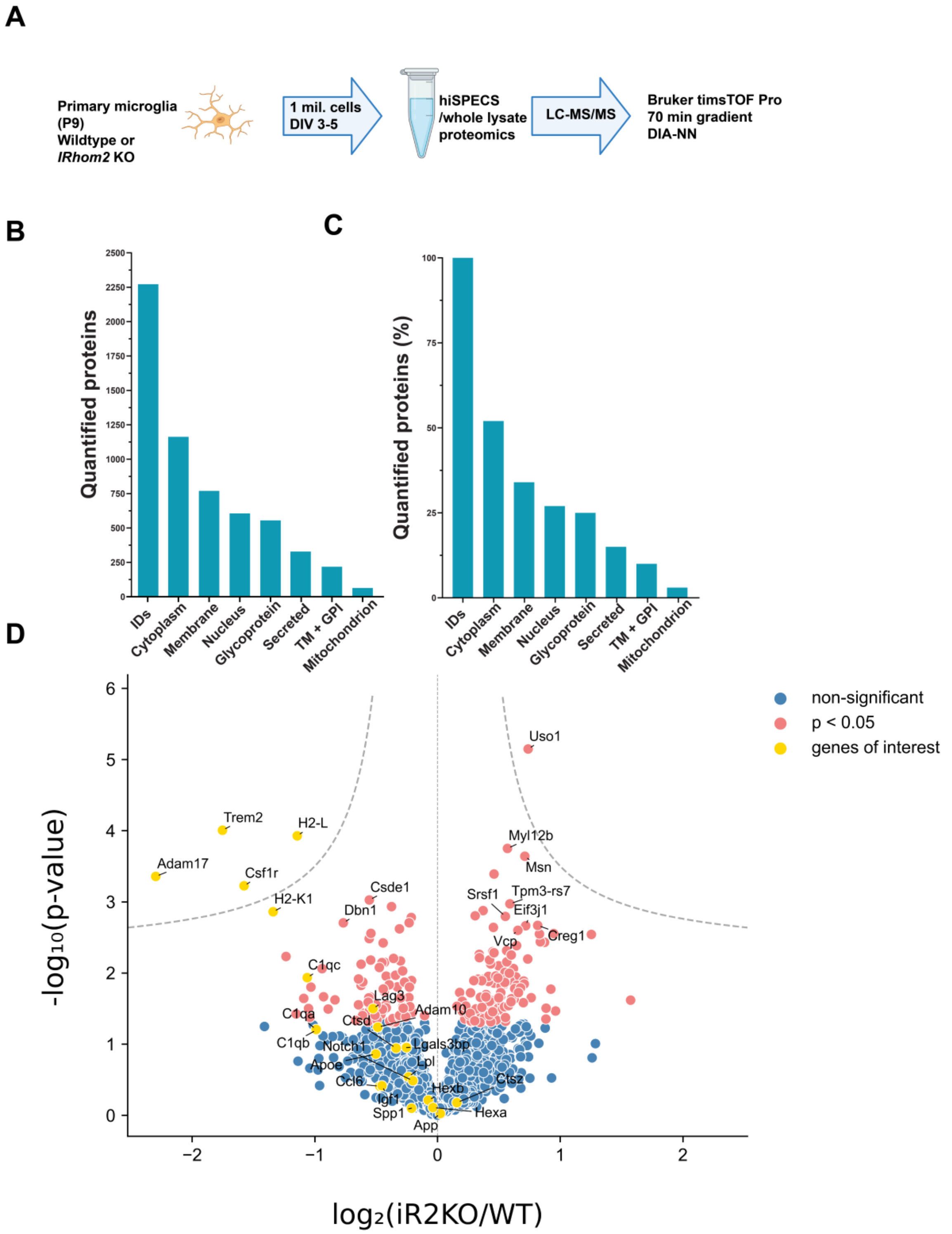

Figure 10: Secretome analysis of microglia from WT or *iRhom2*$^{-/-}$ mice. A) Experimental workflow. Microglia were isolated by magnetic separation and cultured for 5 days *in vitro*. The supernatant is collected and subjected to hiSPECS. The cultured MG are subjected to whole lysate proteomics (see figure 11). B) Bar chart displaying the quantified proteins (minimum 3/6 biological replicates in each group) upon hiSPECS of MG culture supernatant. Proteins are categorized based on their subcellular localisation and post-translational modifications according to UniProt. Upper graph: Absolute numbers of identified protein groups. Lower graph: Percentage distribution of identified protein groups. C) Volcano plot displaying protein abundance changes between WT and *iRhom2*$^{-/-}$ supernatants from MG. The $\log_2$ fold change

is plotted against the p-value ($-\log_{10}$). The dotted hyperbolic curve coloured in grey illustrates the permutation-based false discovery rate (FDR) estimate of 5% (N=6). Proteins with $p < 0.05$ are considered significantly regulated (pink dots). Genes of interest are highlighted in yellow and annotated, irrespective of their p-value.

Alterations in secretome abundance caused by ectodomain shedding are often inversely reflected by the cellular proteome. This is because reduced sheddase activity results in the accumulation of protease substrates on the cell surface. It is also plausible that diminished sheddase activity might trigger increased protein accumulation or even degradation via more intricate feedback or feed-forward mechanisms. Given this complexity, it is important to examine the cellular proteome to confirm that observed changes in the secretome were indeed caused by altered ectodomain shedding. To this end, we performed whole cell lysate proteomics on microglia cultured for secretome analysis using the same mass-spectrometric setup as aforementioned for the hiSPECS analysis. In total, we robustly detected 5845 proteins in 5 out of 6 biological replicates in each group (Fig. 11A). For the comparative analysis of proteomic changes, we considered proteins to be significantly altered if they surpassed a threshold of a log2 fold change greater than 0.5 or less than -0.5 with a p-value less than 0.05. We found subtle changes in the lysate proteome of *iRhom2*$^{-/-}$ as compared to *iRhom2*$^{+/+}$ with 196 proteins being differentially regulated (Fig. 11B). To better compare the relative abundance of TREM2, H2-K1, and CSF1R, which were the most regulated hits in hiSPECS, we extracted the LFQ values and plotted them side by side in relation to wildtype levels (Fig. 11C-E). While H2-K1 and TREM2 lysate LFQs remained unchanged between *Wildtype* and *iRhom2*$^{-/-}$, cellular CSF1R levels increased more than 1.5-fold upon loss of *iRhom2*.

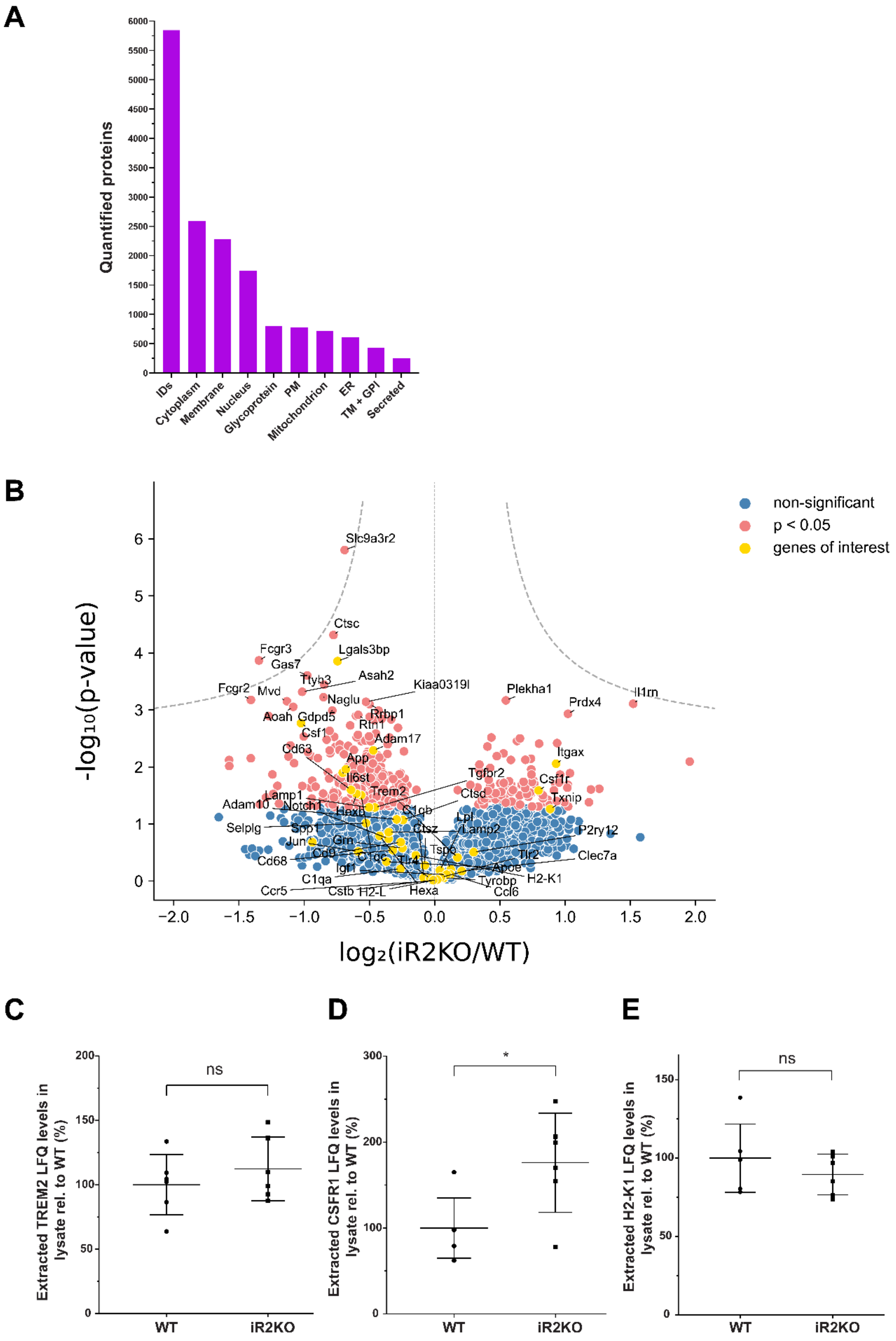

Figure 11: Proteomic analysis of microglia lysates from WT or *iRhom2*$^{-/-}$ mice. A) Bar chart indicating the quantified proteins (min 5/6 biological replicates in each group) upon whole lysate proteomics of MG. Proteins are categorized based on their subcellular localization and post-translational modifications annotation according to UniProt. Upper graph: Absolute

numbers of identified protein groups. B) Volcano plot displaying protein abundance changes between WT and iRhom2 -/- lysates from MG. The $\log_2$ fold change is plotted against the p-value ($-\log_{10}$). The dotted hyperbolic curve coloured in grey illustrates the permutation-based false discovery rate (FDR) estimate of 5% (N=6). Proteins with $p < 0.05$ are considered significantly regulated (pink dots). Genes of interest are highlighted in yellow and annotated, irrespective of their p-value. C-E) Extracted LFQ ratios of cellular TREM2, CSF1R, and H2-K1 of WT and *iRhom2*$^{-/-}$ MG. Two-sided independent Student's t-test. Data are normalized to WT and represented as mean ± SD from six biological replicates. *$p < 0.05$, **$p < 0.01$, ***$p < 0.001$.

4.1.3 Analysis of TREM2 shedding in *iRhom2*$^{-/-}$ microglia

The results obtained from transcriptomic and proteomic comparison hinted towards a more activated microglial state under *iRhom2*$^{-/-}$ conditions. Since TREM2 is known to be involved in mediating microglial activation (Keren-Shaul et al., 2017), and secretome analysis identified TREM2 as major ADAM17 substrate candidate, we hypothesized that TREM2 function could be severely impacted by loss of iRHOM2. Thus, we set out to further validate TREM2 as an ADAM17 substrate by immunoblotting and ELISA. Analysis of the membrane fraction of cultured primary microglia revealed accumulation of immature and mature forms of TREM2 upon loss of iRHOM2. The accumulation was more evident in the highly-glycosylated (mature) forms of TREM2, hinting towards increased TREM2 surface levels (Fig. 12A). In line with this result, the levels of soluble TREM2 in the supernatants were about three-fold increased in *Wildtype* compared to *iRhom2*$^{-/-}$ supernatants of cultured pMG (Fig.12B). As an additional control, we analyzed the levels of sAPPa and found a significant but modest decrease (~1.3-fold) upon loss of *iRhom2* (Fig. 12C). These results demonstrate that ADAM17 is a major sheddase of TREM2.

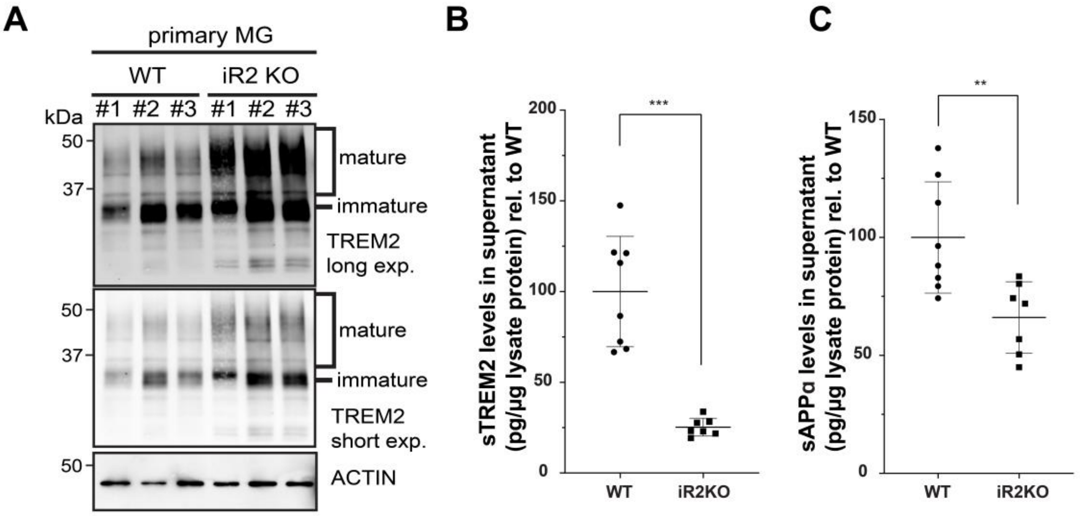

Figure 12: Analysis of TREM2 in microglia from WT or *iRhom2*$^{-/-}$ mice. A) Western blot analysis shows upregulation of mature and immature forms of TREM2 in *iRhom2*$^{-/-}$ (iR2KO) as compared to WT MG. Three biological replicates per genotype are shown. ACTIN serves as a loading control. B-C) Soluble TREM2 levels (B) and sAPPa levels (C) were determined in 72 h supernatants of cultured MG using ELISA. Data are normalized to lysate protein level. Two-sided independent Student's t-test. Data are represented as mean ± SD from at least seven biological replicates. $*p < 0.05$, $**p < 0.01$, $***p < 0.001$.

4.1.4 Functional consequences of TREM2 proteolysis by iRHOM2/ADAM17

Having established TREM2 as a major iRHOM2/ADAM17 client, we reasoned that TREM2 proteolysis potentially affects key microglial functions. To study the functional consequences of reduced TREM2 proteolysis, we isolated microglia from mouse pups (P4) and assessed their phagocytic capacity using an ex vivo amyloid ß (Aß) plaque clearance assay (Sebastian Monasor et al., 2020). We evaluated phagocytic clearance by quantifying the decrease in fibrillar Aß load visualized by Thiazine Red (ThR) staining after microglia were exogenously introduced to amyloid plaque-bearing brain sections obtained from 6-month old APPPS1 mice (Fig. 13A). Microglia deficient in *iRhom2* exhibited a 1.5-fold increase in plaque clearance as compared to *Wildtype*, suggesting enhanced TREM2 function when proteolysis by ADAM17 is impaired.

Another crucial function of microglia is the breakdown of lipids and recycling of cholesterol, a process that is tightly associated with the phagocytic cargo they have ingested. The breakdown of this cargo takes place in lysosomes, which becomes especially important when microglial function is required in scenarios like fighting Aß-pathology or after tissue injury. Tissue injury in the central nervous system (CNS) is often accompanied by lesion of the myelin sheath, a lipid-rich component containing large quantities of cholesterol. Since degradation of cholesterol is not possible, there are mechanisms in place mediating its storage and efflux (Cantuti-Castelvetri et al., 2018). Previous research has indicated that TREM2 plays a decisive role to adapt to excess cholesterol by controlling lipid droplet biogenesis (Gouna et al., 2021). This suggests that enhanced TREM2 function should ideally lead to increased lipid droplet formation. To test this, we isolated microglia from P9 pups and used Bodipy 493/503 dye to stain neutral lipids, which are commonly found within lipid droplets. In accordance with our hypothesis (Fig. 14A), we detected a higher number of lipid droplet-bearing cells in *iRhom2*-deficient microglia (Fig. 14B-C).

In summary, the proteolytic processing of TREM2 in microglia is primarily controlled by the iRHOM2/ADAM17 shedding machinery. The functional consequences of this cleavage event are highlighted by changes in phagocytic activity and altered lipid-droplet formation.

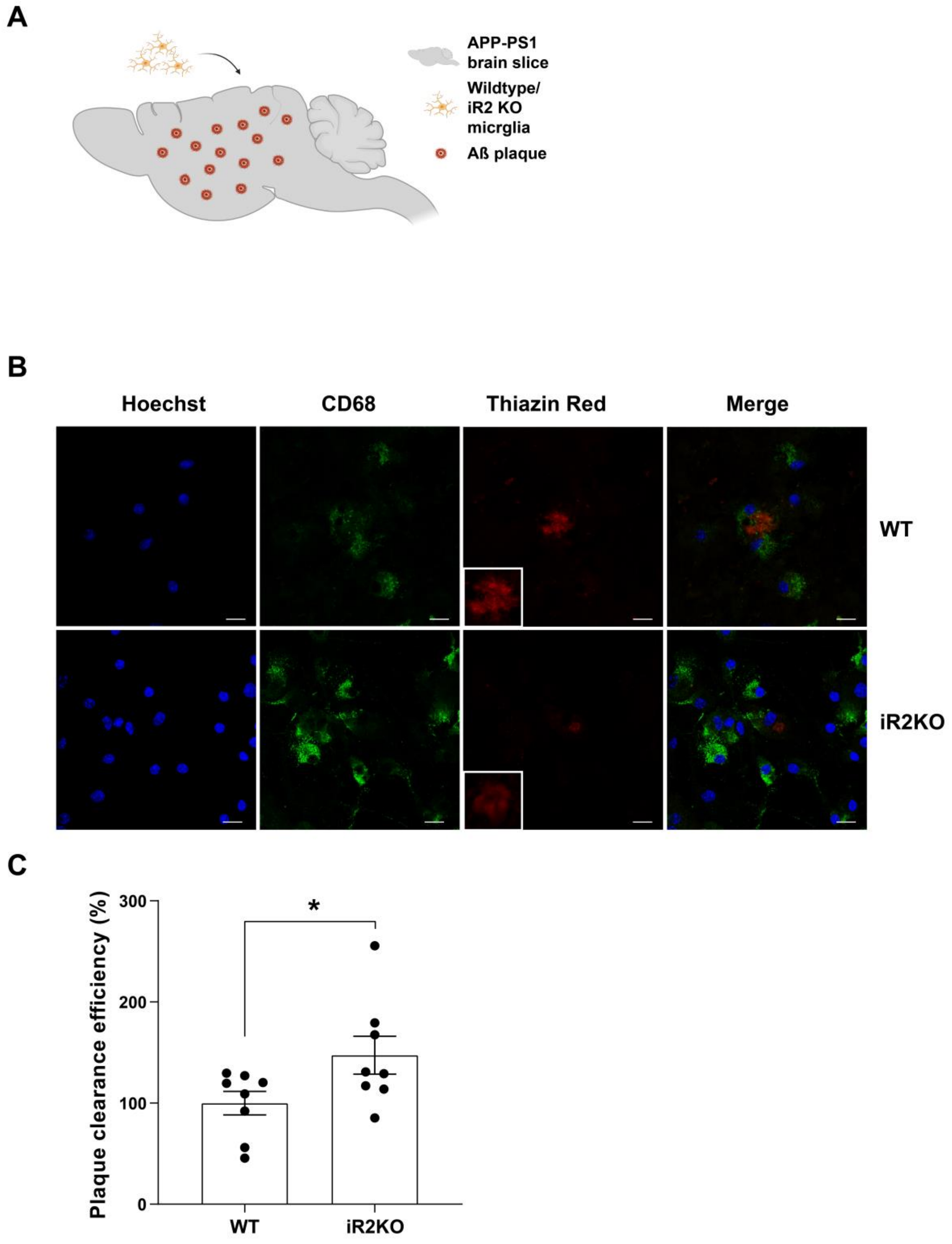

Figure 13: Phagocytosis of Aß plaques is increased in *iRhom2*$^{-/-}$ microglia. A) Schematic of the experimental setup. Acutely isolated microglia from WT or *iRhom2*$^{-/-}$ (iR2KO) mice are plated onto APPPS1 cryosections containing Aß plaques. B) Representative images of WT or *iRhom2*$^{-/-}$ microglia plated onto APPPS1 cryosection. Microglial lysosomes are stained with an antibody against CD68 (green), Aß plaques (red) are stained with Thiazine Red (ThR), and nuclei are stained with Hoechst (blue). Scale bar 20 µM. Inset: magnification of the plaque area. C) Quantification of phagocytic Aß uptake. Phagocytic uptake is expressed as plaque clearance efficiency by comparison of ThR-positive area of a brain section incubated with

microglia to the consecutive brain section without added cells. Two-sided independent Student’s t-test. Data are represented as mean ± SD from three independent experiments or eight biological replicates per genotype. *p < 0.05, **p < 0.01, ***p < 0.001.

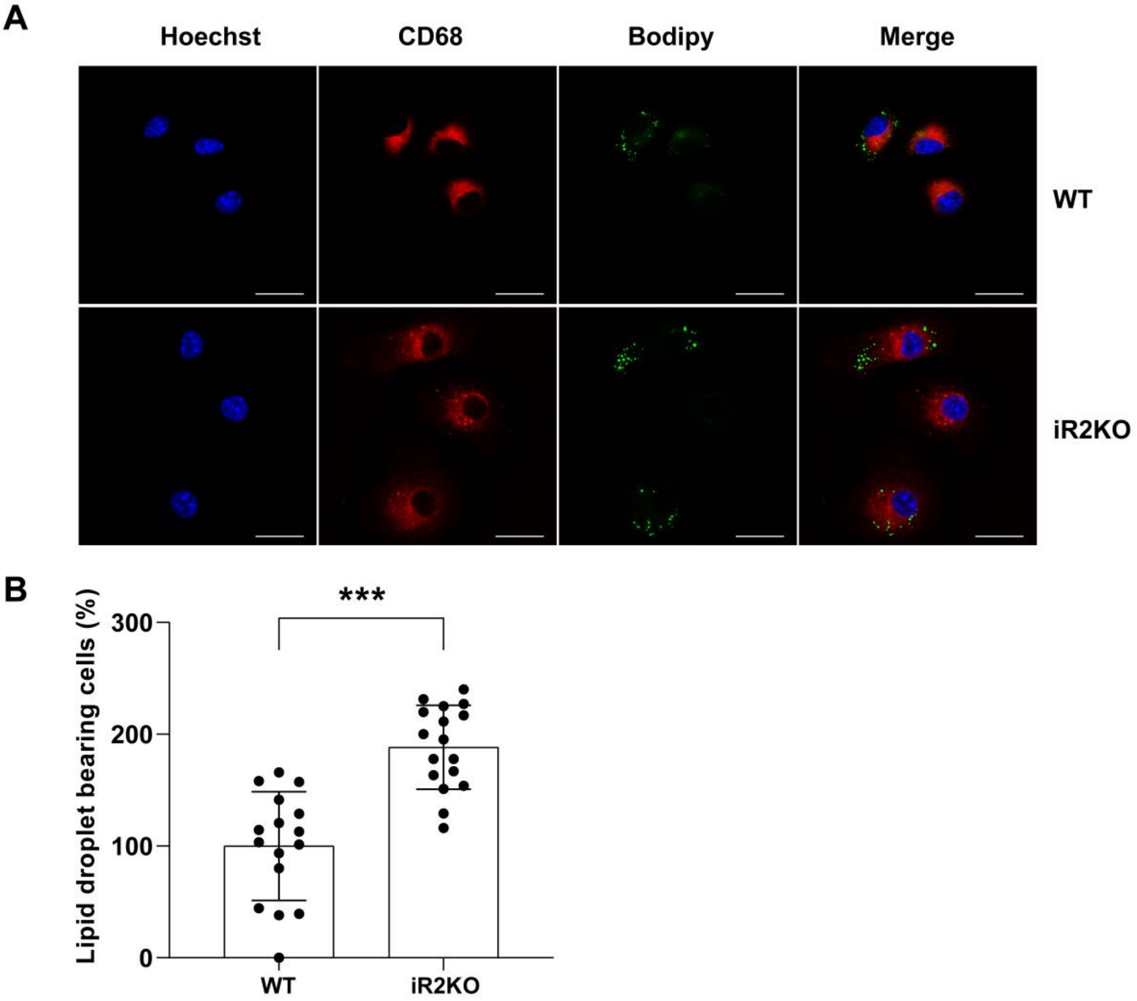

Figure 14: Elevated numbers of lipid droplets-bearing cells in *iRhom2*$^{-/-}$ microglia. A) Representative images of WT or *iRhom2*$^{-/-}$ (iR2KO) microglia plated on coverslips. At DIV4, microglial lysosomes are stained with CD68 (red), lipid droplets with Bodipy (green), and nuclei (blue) using Hoechst. Scale bar 20 µm. B) Quantification of lipid droplet-bearing cells. Two-sided independent Student’s t-test. Data are normalized to WT and presented as mean ± SD from three independent experiments or four biological replicates per genotype. *p < 0.05, **p < 0.01, ***p < 0.001.

4.2 PART II - ADAM Metalloproteases in COVID-19

Most of the data in the following part of this thesis has been published previously in the peer-reviewed Journal EMBO Reports (Jocher et al., 2022). Data that was retrieved from the published article is specifically indicated in the respective figure legend.

4.2.1 Proteolytic ectodomain shedding of ACE2

The Coronavirus receptor ACE2 had previously been shown to be shed by ADAM17 (Jia et al., 2009; Lambert et al., 2005). However, more recent research has also been implicating ADAM10 and other metalloproteases, such as MMP14, as major contributors to the shedding of ACE2 (Guo et al., 2022; Niehues et al., 2022). To investigate ACE2 shedding, we obtained the human A549 lung cell line stably overexpressing ACE2 and exposed them to the broad-spectrum metalloprotease inhibitor BB94 or the ADAM17 preferring inhibitor DPC-333 for 48 hours. These inhibitors were able to prevent the release of the extracellular part of ACE2 into the culture media by up to 50%, showing that these hydroxamate-based metalloprotease inhibitors were indeed potent to halt proteolytic ectodomain shedding of ACE2. Activation of shedding with PMA significantly boosted ACE2 shedding, pointing towards a substantial role for ADAM17 in ACE2 shedding (Fig. 15A). Notably, neither of the compounds affected levels of cellular ACE2 (Fig. 15B-C).

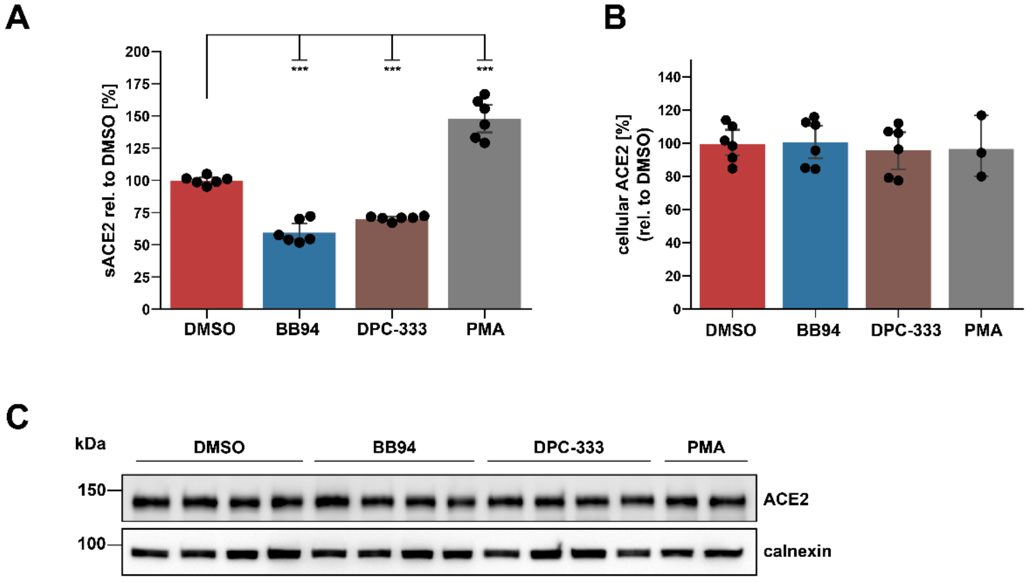

Figure 15: Analysis of ACE2 shedding in A549-ACE2 cells. A-C) A549-ACE2 cells were treated for 48 h with BB94 (10 µM), DPC-333 (5 µM) or DMSO. PMA (25 ng/ml) was added for

3 h before cell lysis. Inhibition of metalloproteases by BB94, and inhibition of ADAM metalloproteases by the ADAM17 preferring inhibitor DPC-333 lowered production of soluble ACE2 (sACE2) significantly. Spike in of PMA 3h before termination of the experiment led to an increase of sACE2 release as determined by ELISA showing that ADAM17 and potentially other BB94-sensitive proteases contribute to ACE2 shedding. B-C) Western blot analysis of ACE2 reveals that cellular levels of ACE2 remain unaffected by the treatment of the cells with indicated small molecules. Data are normalized to loading control calnexin and DMSO (N = 3-6). Two-sided independent Student's t-test with Benjamini-Hochberg FDR correction. A one-way ANOVA with Tukey's post-hoc multiple comparison test was performed. Data are normalized to DMSO. Data (A-B) are represented as means ± 95% CI of at least three biological replicates. $^{*}p < 0.05$, $^{**}p < 0.01$, $^{***}p < 0.001$. Figure retrieved from (Jocher et al., 2022).

To determine the relative contribution of BB94-sensitive proteases to ACE2 shedding, we employed a CRISPR/Cas9-directed genetic ablation approach to eliminate ADAM10 and ADAM17 in A549-ACE2 cells. We used lentiviral particles carrying two different single-guide-RNA (sgRNA) that targeted either ADAM10 or ADAM17 to infect the A540-ACE2 cells (Fig. 16A). In addition to the Cas9 endonuclease, the lentivirus delivered an antibiotic selection cassette. Following antibiotic selection with either puromycin or hygromycin, we examined ADAM10 and ADAM17 levels by immunoblotting (Fig. 16B). Both sgRNA guides successfully targeted ADAM10 and ADAM17, resulting in the reduction of the mature forms of ADAM10 and ADAM17 by up to 95%. Single guide 1 (KO1) was slightly more effective than single guide 2 (KO2) in targeting ADAM10 or ADAM17, hence the double knock-out (dKO) was generated by the combined action of single guide 1. Interestingly, the elimination of either ADAM10 or ADAM17 led to the upregulation of the other (Fig. 16C). To verify the functional depletion of ADAM10 and ADAM17, we measured the release of sAPPa in the supernatants of these cell lines (Fig. 16D). Both ADAM10 KO lines displayed a drastic reduction of sAPPa production of about 80 – 90 %. The ADAM17 KO1 only had a modest reduction in sAPPa of around 15%, while ADAM17 KO2 decreased sAPPa release by 35%. The ADAM10/ADAM17 dKO completed was completely deficient in conducting α-cleavage of APP, indicating a comprehensive knock-out of both proteases in this cell line. Having successfully generated ADAM10 and ADAM17 deficient A549-ACE2 cell lines, we collected supernatant over a 48-hour period to interrogate ACE2 shedding. The knock-out of ADAM17 led to a reduction of 50%, while depletion of ADAM10 decreased sACE2 release by 20%. The dKO reduced sACE2 release by 70%, suggesting that both ADAM10 and ADAM17 contribute to ACE2 cleavage in A549-ACE2 cells (Fig. 16E).

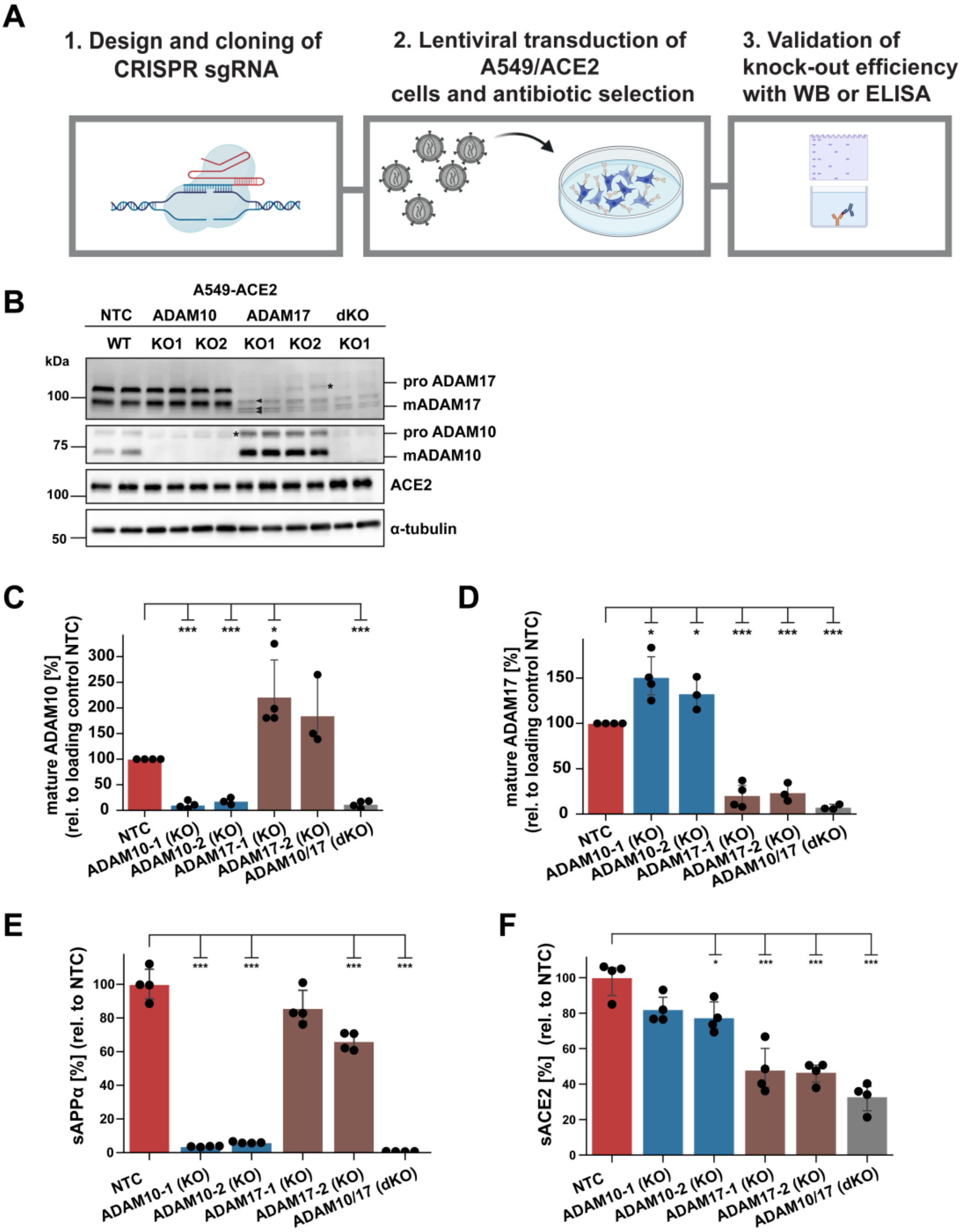

Figure 16: Generation of A549-ACE2 lines with ADAM10 and ADAM17 knock-out (KO). A) CRISPR sgRNAs targeting human ADAM10 and ADAM17 were designed using in silico approaches, and molecular cloning to generate lentiviral plasmids. A549-ACE2 cells are then selected with antibiotics and knock-out was validated with Western blotting and ELISA. Two different KO guides are used to generate KO lines for ADAM10 and ADAM17. A non-targeting control (NTC) guide RNA serves as a control. For generation of the ADAM10 and ADAM17 double knock-out (dKO), guide 1 of ADAM10 and ADAM17 was used. B) Western blot analysis

of A549-ACE2 KO lines reveals successful KO of ADAM10, ADAM17, or both (dKO), while cellular ACE2 remains largely unchanged. α-TUBULIN serves as a loading control. *: low amount of remaining pro ADAM10 and ADAM17. Arrowheads: the ADAM17 antibody detects three nonspecific bands that become only truly visible upon loss of ADAM17. C) Densitometric quantification of mature ADAM10 (left) and mature ADAM17 (right). The data are normalized to the loading control and NTC (N= 3-4). D) To assess the functional depletion of ADAM10 and ADAM17, sAPPα is quantified in conditioned media (48 h) of indicated A549-ACE2 cell lines. E) sACE2 is quantified in conditioned media (48 h) of indicated A549-ACE2 cell lines. B-E) Data are normalized to NTC (N=4) A two-sided independent Student's t test with Benjamini-Hochberg FDR correction was performed. Data are represented as mean ± 95% CI of at least three independent experiments. $^{*}p < 0.05$, $^{**}p < 0.01$, $^{***}p < 0.001$. Figure (B-D) retrieved from (Jocher et al., 2022).

4.2.2 The role of ADAM metalloproteases in the context of SARS-CoV-2 infection

The following chapter contains experiments using authentic SARS-CoV-2, which were conducted in BSL3 environment in collaboration with Dr. Vincent Grass.

Proteolytic ectodomain shedding of ACE2 is conducted by ADAM10 and ADAM17, but whether or not proteolysis contributes to viral infection is debated (Haga et al., 2008) (Heurich et al., 2014). To address this, we employed a semi-automated assay system based on the Incucyte S3 live-cell analysis instrument to monitor viral infection (Fig. 13A). We exposed A549-ACE2 cells to a SARS-CoV-2 virus that transfers green-fluorescent protein (GFP) (Thi Nhu Thao et al., 2020), and assayed viral growth over time. This engineered SARS-CoV-2 (SARS-CoV-2-GFP) was potently infecting A549-ACE2 cells, but did not evoke noticeable GFP signals in naive A549 cells (Fig. 17B-C). Interestingly, the first discernible differences between naïve A549 and A549-ACE2 cells were detected 12 hours post-infecton (hpi), which is approximately the time required for the virus to complete a single replication cycle (Fig. 17D).

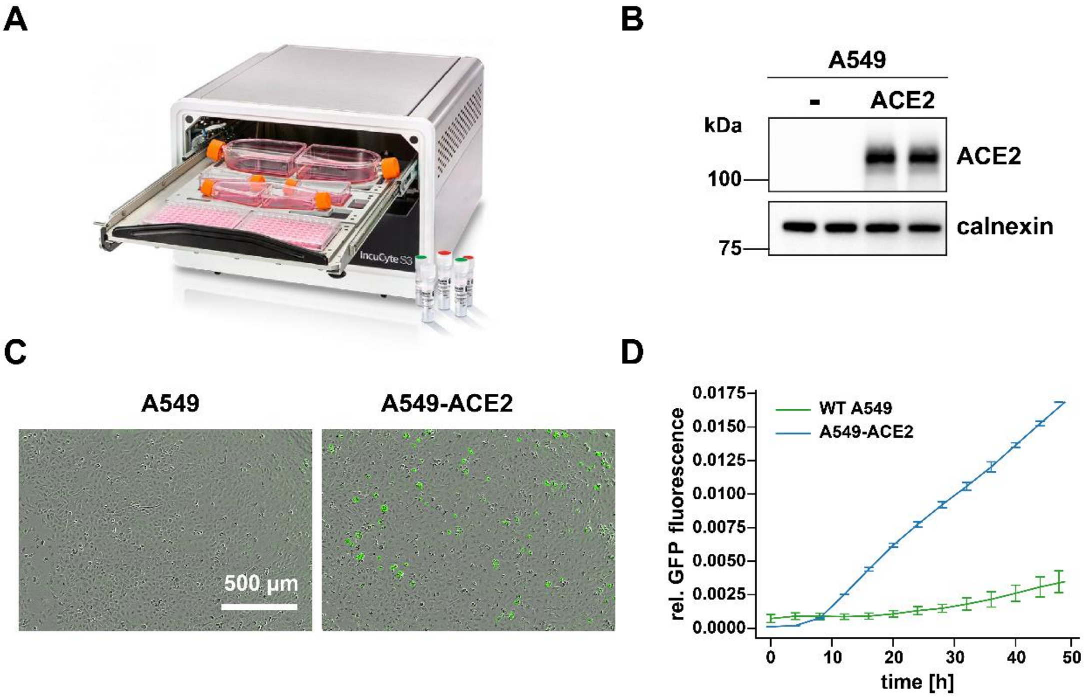

Figure 17: A semi-automated assay system for kinetic quantification of viral growth. A) Image of the Incucyte S3 Live-Cell analysis instrument (©Sartorius AG, Image provided by courtesy of Sartorius AG). B) Successful overexpression of ACE2 demonstrated by Western blot analysis of stably transduced A549-ACE2 cells compared to the ACE2-negative parental A549 cells. C) A genetically engineered SARS-CoV-2 expressing a green-fluorescent (GFP) cassette was used to infect parental or A549-ACE2 cells. Phase contrast and green channel overlay images show viral infection of A549-ACE2 cells but not ACE2-negative A549 cells. Scale: 500 µm. D) Infection is monitored and quantified by live-cell imaging over the course of 48 h, and expressed as the mean of the GFP-positive area relative to the whole area covered by A549 cells within the same well. Data are represented as means ± SD from three biological replicates. Figure B-D was retrieved from (Jocher et al., 2022).

We utilized this assay to measure the viral spread on A549-ACE2 cells that were treated with a panel of sheddase inhibitors at varying concentrations before infection with SARS-CoV-2-GFP (Fig. 18A). We found that the Cathepsin B/L inhibitor E64d, which blocks viral fusion after endocytosis, effectively blocked virus growth even at low concentrations (100 nM), corroborating previous reports that SARS-CoV-2 is able to infect human lung cells through an endocytic-lysosomal pathway (Shema Mugisha et al., 2020; Zhu et al., 2021). By contrast, the TMPRSS2 inhibitor camostat mesylate did not block viral entry in A549 cells, confirming that the TMPRRS2-mediated direct membrane fusion pathway is not active in these cells (Matsuyama et al., 2020). Inhibition of the sheddases BACE1 and BACE2 with the small-molecule inhibitor C3 (Lichtenthaler et al., 2018; Stachel et al., 2004) did not compromise viral growth, thus excluding any of these proteases being involved in SARS-CoV-2 spread. Strikingly, the use of BB94 and TAPI-1 to block sheddases of the ADAM family impeded viral growth severely, indicating a key role for ADAM metalloprotease in this infection model. Next, we wondered about which BB94/TAPI-1-sensitive metalloprotease mediated the effect of viral growth inhibition. To address this, we used apratastat and DPC-333, known to be more selective to ADAM17 than to other ADAM family members, to see whether they reproduce the effect of BB94. As anticipated, both DPC-333 and apratastat had similar efficacy in preventing viral outgrowth in A549-ACE2 cells. It is noteworthy that all three inhibitors significantly stalled viral growth even at a concentration as low as 10 nM (Fig. 18B). Another crucial finding was that none of the inhibitors used compromised cell proliferation or viability, as measured by phase contrast microscopy and MTT (3-(4,5-dimethylthiazol-2-yl)-2,5-diphenyltetrazolium bromide) assays (Fig. 18C-E).

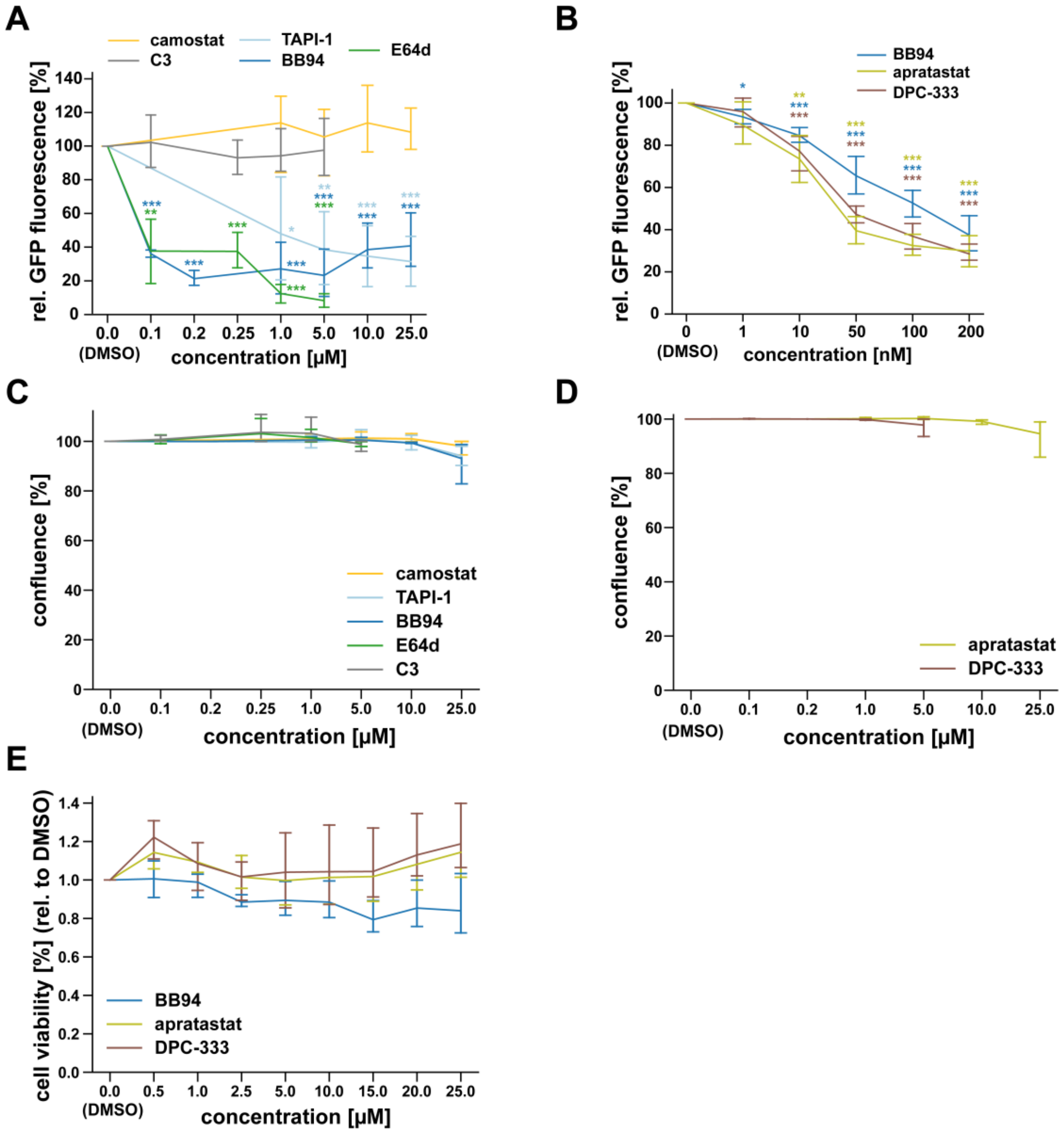

Figure 18: Inhibitors of ADAM metalloproteases block infection of A549-ACE2 cells. A) A549-ACE2 cells were pre-treated for 6 hours with indicated concentrations of the broadspectrum ADAM inhibitor TAPI-1 and BB94, the BACE-inhibitor C3, the TMPRSS2 inhibitor camostat, or the Cathepsin inhibitor E64d. The GFP-fluorescence was determined 48 hours post-infection (hpi). Data (N=3-6) are displayed relative to DMSO-treated control cells. A two-sided independent Student’s t-test with Benjamini-Hochberg FDR correction was performed to compare every indicated data point to DMSO (0 µM). Data are represented as mean ± 95% CI of at least three independent experiments. *p < 0.05, **p < 0.01, ***p < 0.001. Figure retrieved from (Jocher et al., 2022).

4.2.3 Emergence of a metalloprotease-dependent entry pathway in SARS-CoV-2 virus

The following chapter contains experiments using authentic SARS-CoV-2 to infect primary human cells, which were conducted in BSL3 environment in collaboration with Dr. Vincent Grass and Dr. Constanze Jakwerth.

We observed that the SARS-CoV-2 virus heavily relies on the cathepsin-dependent entry (Fig. 18A) to infect A549-ACE2 cells. At the same time, we found that a metalloprotease, sensitive to BB94 and other inhibitors more specifically targeting ADAM17, blocked virus spread just as efficiently as E64d. Thus, we hypothesized that a metalloprotease could constitute a yet unknown entry pathway or that a metalloprotease integrates into the endocytic-lysosomal pathway. To investigate this, we treated the A549-ACE2 cells with either a metalloprotease inhibitor, E64d, or a combination of both. Strikingly, when the cells were pre-treated with the compounds for several hours prior to infection, A549-ACE2 cells were completely protected from infection (Fig. 19A). However, in practical situations, treatment is typically administered after infection has occurred, whereas our research has primarily focused on a preventive treatment paradigm. To ascertain that these inhibitors would also be effective post-infection, we infected the A549-ACE2 cells and incubated them for 4 hours before applying the pharmacological treatment (Fig. 19B). Remarkably, the metalloprotease inhibitors were nearly as efficient in blocking further viral spread as when employed as a preventive measure. In contrast, E64d was considerably less effective when administered after viral infection.

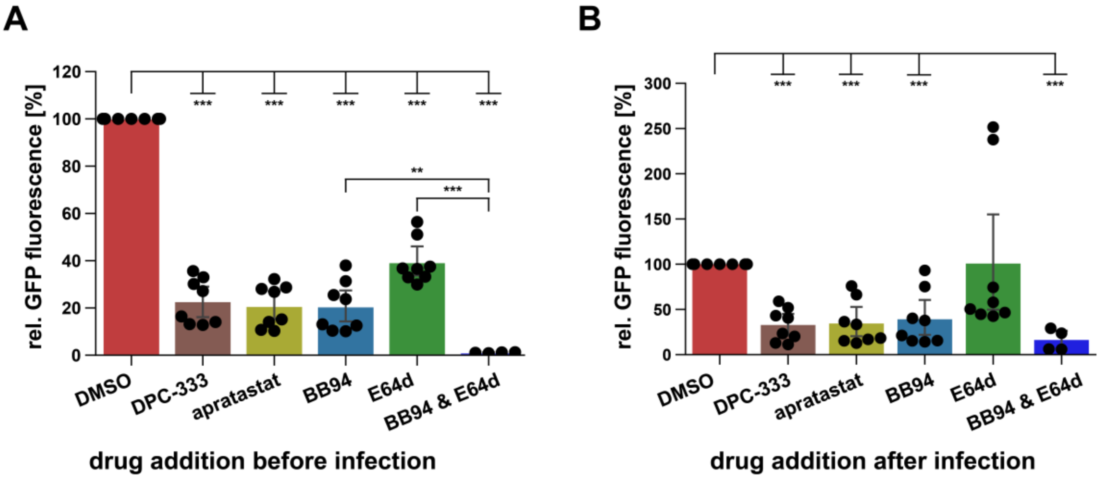

Figure 19: A metalloprotease-dependent viral entry pathway emerges in A549-ACE2 cells. Viral growth is monitored using the Incucyte S3 as described in Fig. 13. A-B) A549-ACE2

cells are pre-treated for 6 hours with DPC-333 (5 µM), apratastat (10 µM), BB94 (10 µM), E64d (5 µM), and BB94 + E64d (10 µM + 5 µM) before being infected with SARS-CoV-2-GFP. B) A549-ACE2 cells are treated with indicated inhibitors 4 hours after infection with SARS-CoV-2-GFP. Data (A-B) are from 48 h post-infection and are normalized to DMSO (N=4-8). A two-sided independent Student's t-test with Benjamini-Hochberg FDR correction was performed. Data are represented as mean ± 95% CI of at least three independent experiments. *p < 0.05, **p < 0.01, ***p < 0.001. Figure retrieved from (Jocher et al., 2022).

For viral research, A549 lung cells are a commonly used cell line, but they do not have all the relevant features in place, to draw a general conclusion with regards to the molecular underpinnings of SARS-CoV-2 cells entry. Hence, it is important to validate obtained findings in cells that more closely resemble the potential *in vivo* situation. Normal human bronchoepithelial cells (NHBE) is the cell model of choice to address this question, because they derive from human post-mortem tissue and express ADAMs, and the canonical host cell protease TMPRSS2 at significant levels (Jocher et al., 2022). We infected NHBE cells from up to eight different donors with SARS-CoV-2-GFP after treating the cells with inhibitors blocking the TMPRRS2, the cathepsin and the possible metalloprotease-dependent entry pathways (Fig. 20A-B). Interestingly, the metalloprotease inhibitors BB94, apratastat, and DPC-333 impeded viral infection of NHBE cells to a similar extent (50 – 70% reduction). The TMPRSS2 inhibitor camostat displayed comparable, but more variable effects on viral entry. E64d blocked viral entry potently in some donors, but had no or only modest effects on others. To corroborate the finding that the metalloprotease entry route functions as a separate pathway, we exposed NHBE cells to combinations of each inhibitor. Dual combinations were additive in terms of their antiviral potency, indicating the presence of three unique cellular entry pathways. Impressively, the triple combination of camostat, E64d, and BB94 entirely safeguarded NHBE cells from viral infection, underscoring the importance of blocking all available entry routes to achieve maximum protection (Fig. 16A). Similar to A549-ACE2 cells, the application of a metalloprotease inhibitor, either alone or in combination with camostat or E64d, after viral infection exhibited strong antiviral effects in NHBE cells. It is noteworthy that the antiviral activity of E64d was absent in NHBE cells when applied post-infection (Fig. 20B).

Together, these results demonstrate that SARS-CoV-2 exploits three distinct cellular entry pathways to infect NHBE cells. In A549-ACE2 cells, however, only two pathways are available, because TMPRSS2 is absent in these cells.

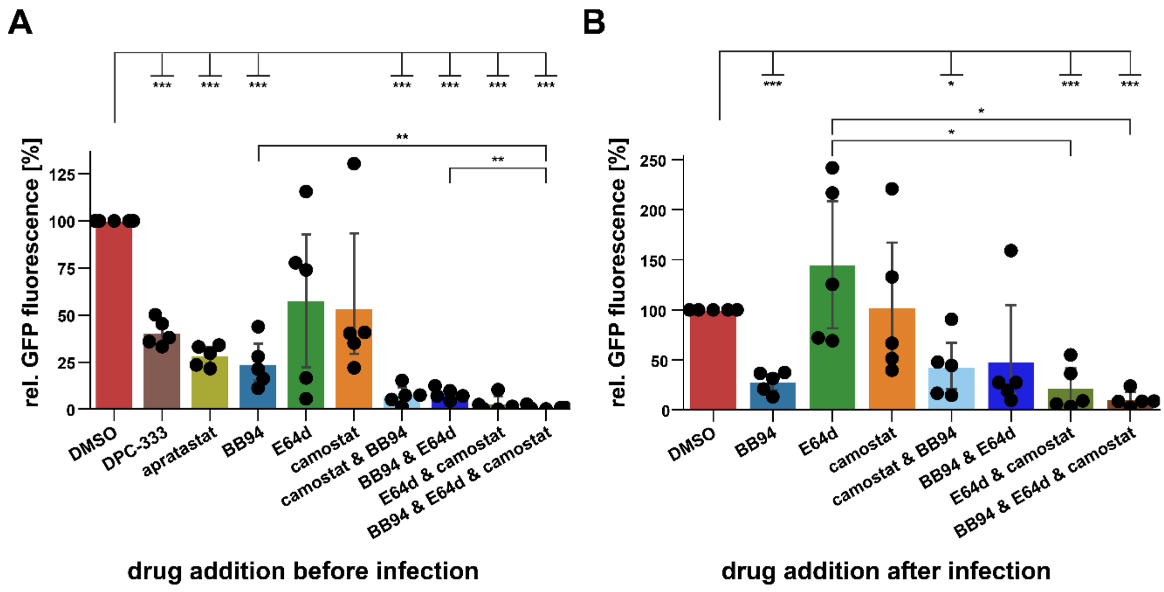

Figure 20: The metalloprotease entry pathway is active in primary normal human bronchoepithelial cells (NHBE). Viral growth is monitored using the Incucyte S3 as described in Fig. 13. A-B) NHBE cells are pre-treated for 6 hours with DPC-333 (5 µM), apratastat (10 µM), BB94 (10 µM), E64d (5 µM), camostat (10 µM), or in combination with camostat + BB94, (10 µM), BB94 + E64d (10 µM + 5 µM), E64d + camostat (5 µM + 10 µM). and BB94 + E64d + camostat (10 µM + 5 µM + 10 µM) before being infected with SARS-CoV-2-GFP. B) NHBE cells are treated with indicated inhibitors 4 hours after infection with SARS-CoV-2-GFP. Data (A-B) are from 72 h post-infection and are normalized to DMSO (N=4-8). A two-sided independent Student’s t-test with Benjamini-Hochberg FDR correction was performed. Data are represented as mean ± 95% CI of at least three independent experiments. *$p < 0.05$, **$p < 0.01$, ***$p < 0.001$. Figure retrieved from (Jocher et al., 2022).

4.2.4 The metalloprotease entry pathway is hijacked by SARS-CoV-2 variants of concern

The following chapter contains experiments using authentic SARS-CoV-2, which were conducted in BSL3 environment in collaboration with Dr. Vincent Grass and Lydia Riepler.

Next, we examined whether the metalloprotease inhibitors could also prevent the infection of A549-ACE2 cells with clinical isolates of SARS-CoV-2 (such as SARS-CoV-2-MUC-IMB-1 and the Innsbruck 1.2 isolate). Additionally, we evaluated their impact on viral outgrowth caused by the emerging, more rapidly spreading alpha (B.1.1.7), beta (B.1.351), delta (B1.617.2), and omicron (B.1.1.529) SARS-CoV-2 variants (Tegally et al., 2020; Thi Nhu Thao et al., 2020). Clinical virus isolates are not easily available as engineered version that express GFP upon infection, hence we opted to assess viral infection by the classical RT-qPCR approach that quantifies viral replication within the infected A549-ACE2 cells. The detection of viral replication by RT-qPCR is based on the properties of fluorescent probes like SYBRGreen. These probes emit strong signals when they are bound to double-stranded DNA complexes (Fig. 21A). Intriguingly, BB94 treatment prior to infection reduced viral RNA in all of the tested SARS-CoV-2 strains, including the alpha, beta, delta, and omicron virus variants (Fig. 21B-C). Comparable results were observed with the ADAM17-selective inhibitor DPC-333, which restricted infection of A549-ACE2 cells by the Innsbruck 1.2 isolate virus and the beta and delta virus variants to an extent similar to BB94 (Fig. 21C). These experiments emphasize the significance of a metalloprotease in the infection process of SARS-CoV-2 and its variants of concern.

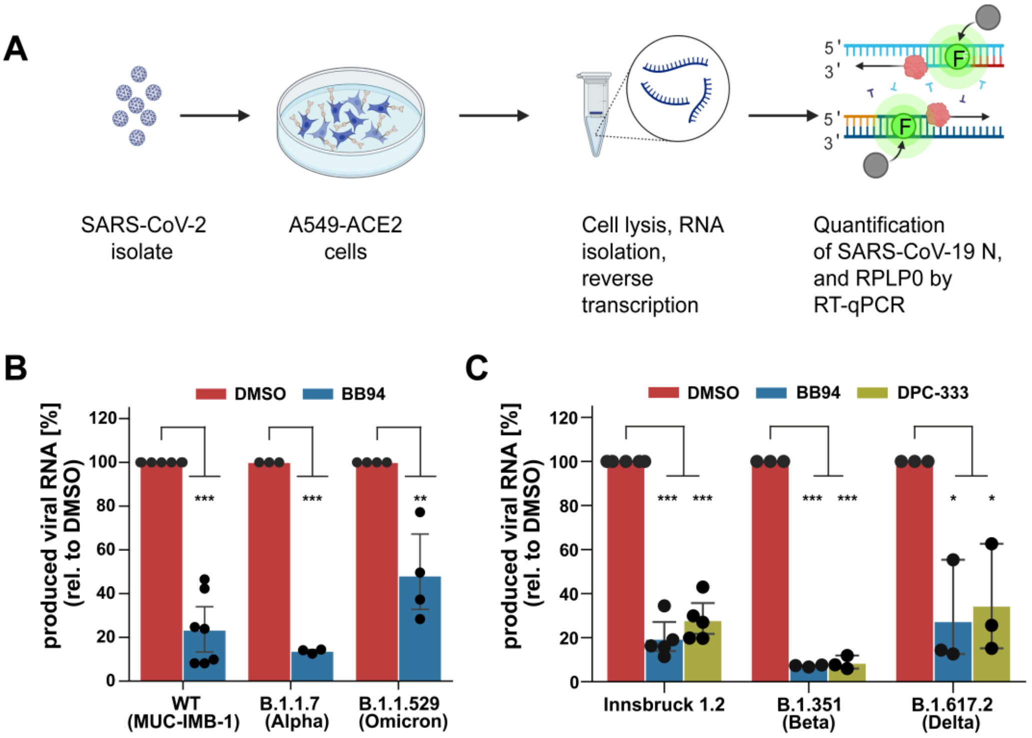

Figure 21: Metalloprotease inhibitors block entry of SARS-CoV-2 variants of concern. A) Illustration of experimental workflow. A549-ACE2 cells are infected with SARS-CoV-2 isolates. 24 hours after inoculation, the cells are lysed and viral replication is quantified by RT-qPCR. Probes targeting the SARS-CoV-2 N protein coding region and RPLP0 as the housekeeping control gene are used as replication primers necessary for fluorescent (F) SYBRGreen incorporation. B-C) A549-ACE2 cells are pre-treated for 6 hours with BB94 (10 µM) or DPC-333 (5 µM), and then inoculated with the indicated variants of concern. Viral RNA (SARS-CoV-2 N gene relative to RPLP0) is quantified 24 hours post-infection. Data are normalized to DMSO (N=3-7). A two-sided independent Student's t-test with Benjamini-Hochberg FDR correction was performed. Data are represented as mean ± 95% CI of at least three independent experiments. *$p < 0.05$, **$p < 0.01$, ***$p < 0.001$. Figure retrieved from (Jocher et al., 2022).

4.2.6 Elucidating key determinants of the SARS-CoV-2 metalloprotease entry pathway

The following chapter contains experiments using pseudotyped VSV-S, which were conducted in collaboration with Lydia Riepler.

The lifecycle of the SARS-CoV-2 virus involves several equally important steps, as discussed earlier (see Fig. 6). Yet, it remains unclear at which exact stage the metalloprotease plays its role. Following up on our hypothesis that the cleavage of ACE2 by ADAM17 triggers this mechanism, we used replication-deficient vesicular stomatitis virus equipped with the SARS-CoV-2 S protein (VSV-S) and a GFP-reporter cassette to infect A549-ACE2 cells (Fig. 22A). For comparison, we used a VSV pseudotype equipped with glycoprotein (GP) of the lymphocytic choriomeningitis virus (LCMV) that uses α-dystroglycan as its receptor (Fig. 22B). As expected, both pseudotyped viruses readily infected A549-ACE2 cells. However, only metalloprotease inhibitors blocked VSV-S infection, indicating a specific mechanism requiring ACE2, the SARS-CoV-2 spike protein, and a metalloprotease (Fig. 22A-B). Next, we addressed whether ADAM10 or ADAM17 mediated the effect of the metalloprotease inhibition on pseudotype entry. To do so, we infected the A549-ACE2 knock-out cell lines (Fig. 22C) with the VSV-S pseudotype. Metalloprotease inhibition by BB94 reduced pseudotype entry by about 60% in NTC and ADAM17 KO cells, but had no effect in ADAM10 and ADAM10/ADAM17-dKO cells. Further addition of E64d to ADAM10-deficient cells entirely halted viral infection. Strikingly, the combination of BB94 and E64d fully blocked viral infection in all cell lines, showing that the pseudotype, like the genuine SARS-CoV-2, enters the A549-ACE2 cells through an endocytic-lysosomal and a metalloprotease dependent pathway (Fig. 22C). Having established that ADAM10 was responsible for pseudotype entry, we wondered whether ADAM10 acts through proteolytic cleavage of ACE2, because ADAM10 did not make a major contribution to ACE2 shedding (Fig. 16E). To this end, we pre-incubated the VSV-S pseudotype with increasing amounts of recombinant soluble ACE2 (sACE2) or bovine serum albumin (BSA) as control. We observed a decreasing number of infected cells as sACE2 levels increased, demonstrating that ACE2 cleavage by ADAM10 is dispensable for pseudotype entry (Fig. 22D).

The pseudotype is a good model to determine the most essential components required for virus entry, but it has certain key differences compared to the genuine SARS-CoV-

2 virus that could potentially affect the interpretation of results from *in vitro* experiments. Thus, we infected the A549-ACE2 cell lines with a clinical isolate of SARS-CoV-2 (MUC-IMB-1) and performed RT-qPCR to quantify viral replication in these cells. The metalloprotease inhibitor BB94 reduced viral RNA by about 70% in NTC cells. In both the ADAM10 and ADAM17 KO lines (except ADAM10 KO2), metalloprotease inhibition lowered viral RNA load, but had essentially no effect on ADAM10/ADAM17 dKO cells. The KO of ADAM17 had a slightly higher effect than KO of ADAM10, which yielded more variable results. These results demonstrate that the SARS-CoV-2 relies more on ADAM17 and ADAM10 for viral entry, and only the dKO fully mimics the effect of the metalloprotease inhibitor (Fig. 22E). Next, we addressed whether ACE2 shedding contributes to infection of A549-ACE2 cells with the authentic SARS-CoV-2 virus, because sACE2 production by ADAM17 was dispensable for pseudotype entry. To boost sACE2 production, we incubated the A549-ACE2 cells with increasing amounts of PMA before infection of the cells. Interestingly, PMA drastically increased A549-ACE2 infection over the course of 48 hours, demonstrating that increased ADAM17 activity augments viral infection (Fig. 22F).

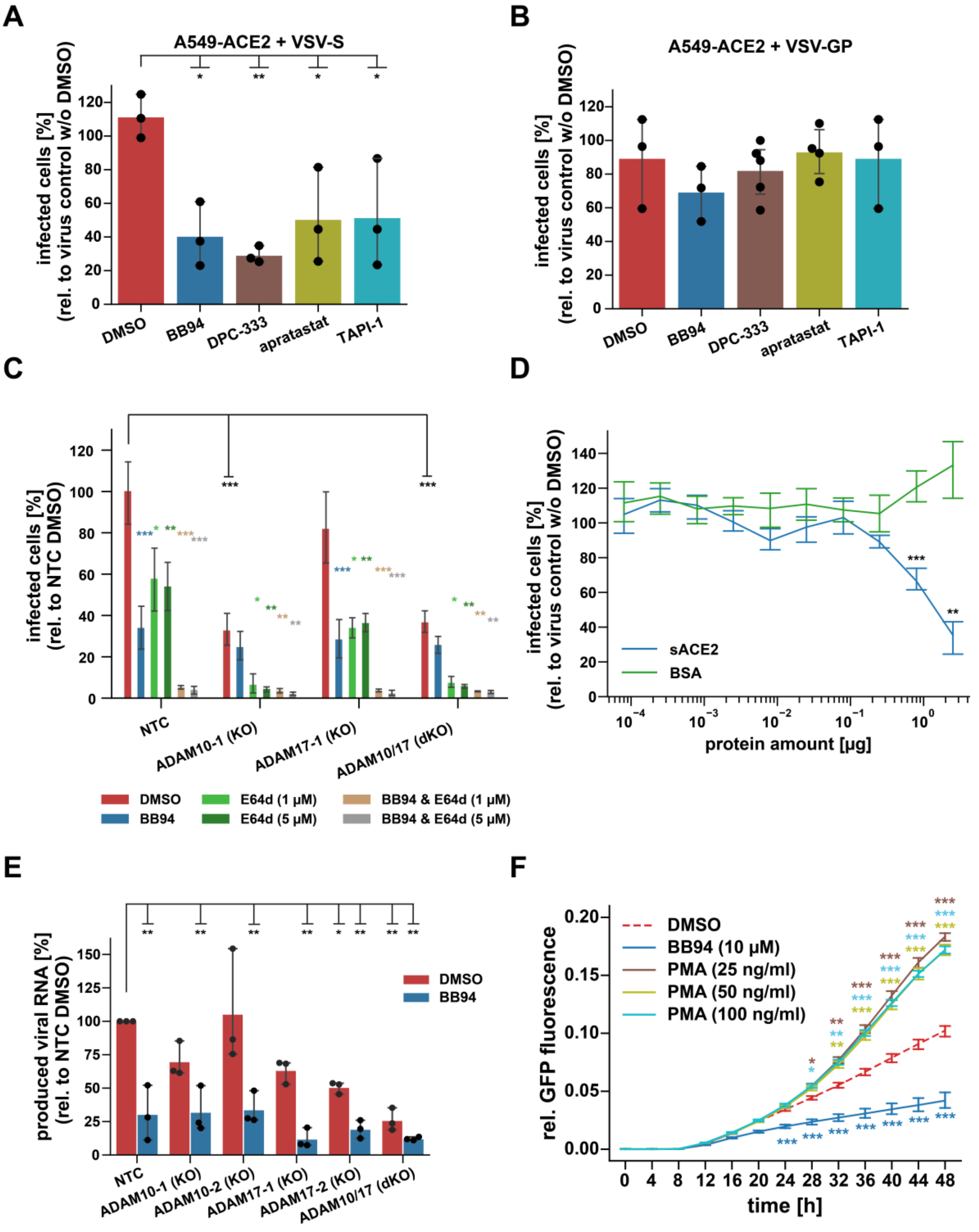

Figure 22: ADAM10 and ADAM17 contribute to SARS-CoV-2 entry. A-B) A549-ACE2 cells were pre-treated for 1 hour with BB94 (10 µM), DPC-333 (5 µM), apratastat (10 µM), or TAPI-1 (10 µM) before inoculation with (A) GFP-encoding pseudotyped VSV-S (VSV pseudotyped with SARS-CoV-2 spike protein (VSV-S)) or (B) pseudotyped VSV-GP (VSV pseudotyped with LCMV glycoprotein (VSV-GP)). At 16 hours post-inoculation, infected cells were analyzed by counting of GFP-positive cells. Data (N=3-5) are normalized to virus-only control wells without vehicle (virus control w/o DMSO). A one-way ANOVA with Tukey's post-hoc multiple comparison test was conducted. Asterisks indicate significance compared to DMSO. C) A549-ACE2 knock-out cell lines were inoculated with VSV-S particles and infected cells were counted 16 hpi. Cells were pre-treated with indicated inhibitors 1 hour before inoculation. Data

(N=3-5) are normalized to NTC DMSO. A two-way ANOVA with Tukey's post-hoc multiple comparison test was conducted. Coloured asterisks indicate significance compared to DMSO within the respective cell line. Black asterisks indicate significance when compared to DMSO of the NTC cell line. D) GFP-encoding pseudotyped VSV-S were pre-incubated with indicated amounts of the human ACE2 ectodomain (sACE2) or bovine serum albumin (BSA) prior to infection of A549-ACE2 cells. GFP-positive cells were counted at 16 hpi. Data are normalized to a virus-only control without vehicle (N=3). A two-sided independent Student's t-test with Benjamini-Hochberg FDR correction was performed. E) Indicated A549-ACE2 cell lines are infected with the SARS-CoV-2 "Wildtype" strain MUC-IMB-1 6 hours after treatment with BB94 (10 µM) or DMSO. Viral RNA (SARS-CoV-2 N gene relative to RPLP0) is quantified 24 hours post-infection. Data are normalized to DMSO (N=3). A two-sided independent Student's t-test with Benjamini-Hochberg FDR correction was performed. F) A549-ACE2 were treated with BB94 (10 µM) for 6 hours or PMA for 30 minutes at indicated concentrations before infection with SARS-CoV-2-GFP. A two-way ANOVA with Tukey's post-hoc multiple comparison test was conducted. Asterisks indicate significantly changed fluorescence intensity of the respective condition compared to the DMSO control at the respective time point (N = 9). Data (A-F) are represented as mean ± 95% CI of at least three independent experiments. *p < 0.05, **p < 0.01, ***p < 0.001. Figures apart from Fig. (18C) are retrieved from (Jocher et al., 2022).

4.2.7 The SARS-CoV-2 spike protein is a target for metalloprotease cleavage

We have shown that ACE2 can be cleaved by both ADAM10 and ADAM17, but the relative contribution of ADAM10 to this cleavage was rather minor compared to ADAM17 (Fig. 16E). At the same time, ADAM10 was responsible for the infection of A549-ACE2 cells, and sACE2 prevented the infection of these cells (Fig. 22C-D). When infecting A549-ACE2 with SARS-CoV-2, the contribution ratio was in favor of ADAM17, but the dKO had the strongest effect, suggesting that both proteases play a role (Fig. 22E). Hence, we suspected that the proteolysis of ACE2 is not the only reason for the underlying phenomenon. Knowing that the spike protein must be cleaved at the S2' site for the virus to enter the cells (Hoffmann et al., 2018), we hypothesized that the spike protein can also be cleaved by ADAM10 or ADAM17. To tackle this question, we performed *in vitro* cleavage assays using recombinant full-length SARS-CoV-2 spike protein and the catalytically active portions of either ADAM10, ADAM17, or TMPRRS2. To block ADAM or TMPRRS2 activity we pre-incubated these proteases with BB94 or camostat, respectively, before adding the spike protein and activity buffers. As anticipated, both ADAM10 and ADAM17 readily cleaved the spike protein in vitro, and the band pattern was remarkably similar to that of TMPRRS2 (Fig. 23A-B). The SARS-CoV-2 must bind to the ACE2 receptor on the cell surface and this can theoretically serve as a platform for interaction with either ADAM10 or ADAM17, but unlike in an in vitro experiment, the interaction between spike and protease is highly context-dependent and needs precise timing. To demonstrate that the SARS-CoV-2 virus was capable of interacting with ADAM17 *in situ*, we conducted proximity ligation assays (PLA). This method is based on signal amplification by closed circle DNA molecules when two proteins are in close proximity (Fig. 23C). We infected A549-ACE2 cells with SARS-CoV-2 (MUC-IMB-1) and incubated the cells on ice for 2 hours to stop endocytosis. Then, we either maintained the cells on ice or moved them to 37°C for 15 minutes to check whether the interaction of spike and ADAM17 occurs. A strong PLA signal was detected when cells were maintained on ice, showing that ADAM17 and spike already interact at the cell surface. Interestingly, when shifting the cells to 37°C, the PLA signal increased further, suggesting that ADAM17 was integral to SARS-CoV-2 entry.

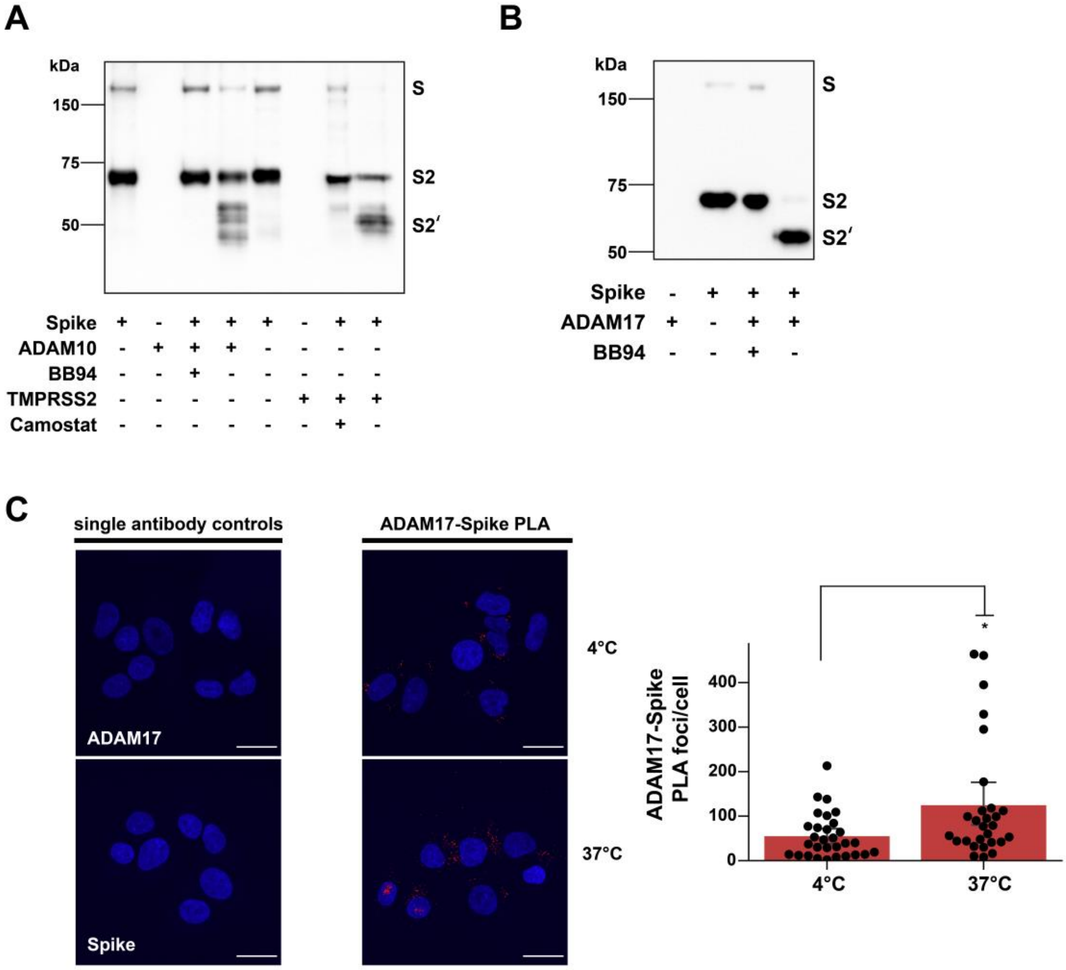

Figure 23: ADAM10 and ADAM17 cleave the SARS-CoV-2 spike protein in vitro, and endogenous ADAM17 interacts with authentic SARS-CoV-2 spike on A549-ACE2 cells.

A-B) In vitro cleavage of SARS-CoV-2 spike protein by recombinant ADAM10, ADAM17, and TMPRSS2. The recombinant spike protein (1 µg) is digested with the indicated proteases in the presence or absence of protease inhibitors (10 µM) for 24 hours at a 1:1 ratio and is analyzed by Western Blot. The C-terminally HIS-tagged spike protein is detected using an anti-HIS antibody. C) A proximity ligation assay (PLA) demonstrates the interaction of endogenous ADAM17 with the spike protein of authentic SARS-CoV-2. A549-ACE2 cells are infected with SARS-CoV-2 (MUC-IMB-1) and placed on ice. After 2 hours, cells are incubated at 37°C for 15 min or left on ice. Representative overlays between Nuclei (Hoechst, blue) and the PLA (pseudo-coloured: red) channel are shown. Scale: 20 µm. D) PLA foci per cell are determined by automated image analysis using Image J. A two-sided independent Student's t-test was performed. Data (N=28-30 images per condition) are represented as means ± 95% CI of at least three independent experiments. *$p < 0.05$, **$p < 0.01$, ***$p < 0.001$. Figure retrieved from (Jocher et al., 2022).

Having shown that ADAMs can cleave the recombinant SARS-CoV-2 spike protein *in vitro* and that ADAM17 can interact with authentic SARS-CoV-2 spike *in situ*, we wondered whether spike proteolysis could also occur in a cellular system. To test this, we opted for a Syncytia formation assay, which allows for the observation of multinucleation upon spike proteolysis after ACE2 engagement (Fig. 24A). When A549-ACE2-NTC cells were co-cultured together with Spike-expressing HEK293T cells, robust syncytia formation was observed (Fig. 24B). Addition of BB94 lowered the GFP-positive syncytia area, as well as the number of nuclei within each syncytium by up to 50%. Knocking out ADAM10 in A549-ACE2 cells was sufficient to bring the syncytia formation and the number of nuclei in the syncytia down to the level seen in BB94-treated NTC cells. However, ADAM17 KO did not have the same effect on syncytia formation, whereas the effect of knocking out both ADAM10 and ADAM17 was similar to that of the ADAM10 single KO (Fig. 24B-C). In addition, the cathepsin inhibitor E64d that effectively blocked SARS-CoV-2 cell infection (Fig. 18A, 19), did not prevent cell-cell fusion (Fig. 25).

Together, these results reveal that although both ADAM10 and ADAM17 can cleave the spike protein *in vitro*, ADAM10 specifically mediates the formation of syncytia, which is indicative of spike protein priming in a cellular system. Thus, it is very well possible that different cellular and viral systems require different proteases to function effectively.

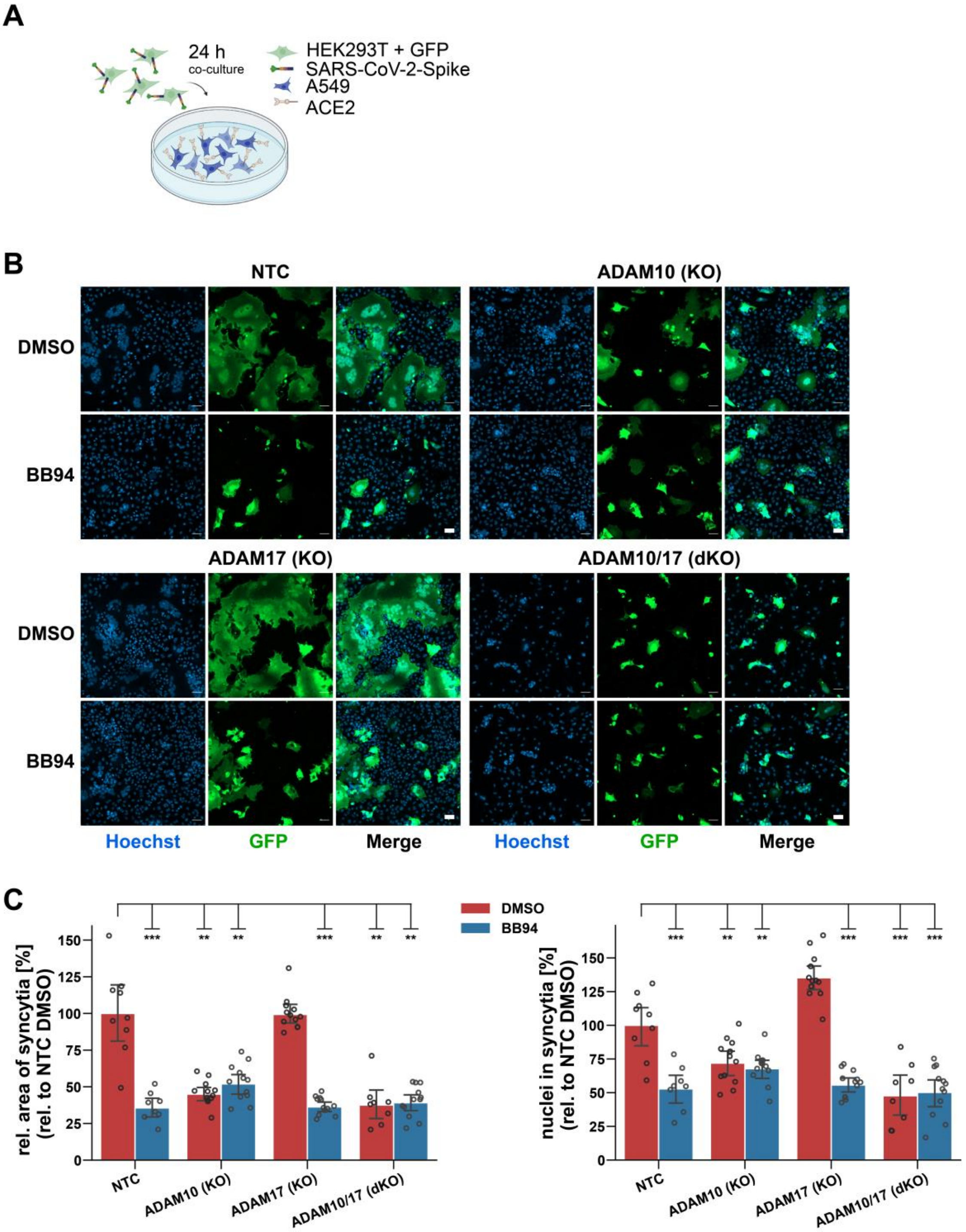

Figure 24: ADAM10 mediates syncytia formation in A549-ACE2 cells. A) Illustration of the syncytia formation assay. GFP and spike protein co-expressing donor cells (HEK293T) are co-cultured with A549-ACE2 NTC, ADAM10 KO guide 1, ADAM17 KO guide 1, or dKO acceptor cells. 24 h co-cultures are analyzed by confocal microscopy. B) Confocal microscopy of A549-ACE2 fused with Spike protein expressing HEK293T cells demonstrates that spike protein activation required for syncytia formation is mediated by ADAM10, and cannot be further blocked by the addition of BB94 (10 µM). Scale: 50 µm. C) Quantification of confocal images,

as shown in (B). Left Plot: The area of syncytia (green, GFP area) is quantified and normalized to the Hoechst signal (nuclei, blue) to equalize differences in cell density of the recorded syncytia area. Right Plot: The nuclei within fused cells are quantified by calculating the ratio between the Hoechst signal within syncytia and the total Hoechst area. Data are normalized to NTC DMSO (N >= 8 images per condition). A two-way ANOVA with Tukey's correction for multiple comparisons was performed. Data are represented as means ± 95% CI of at least 3 independent experiments. *p < 0.05, **p < 0.01, ***p < 0.001. Figure retrieved from (Jocher et al., 2022).

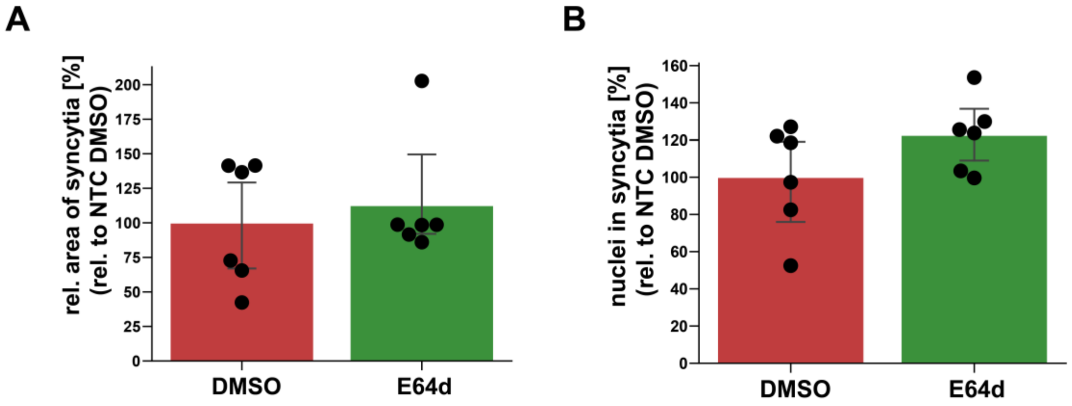

Figure 25: Cathepsins do not contribute to syncytia formation in A549-ACE2 cells. A-B) Experiment is carried out as described in Fig. 24. A549-ACE2 cells were co-cultured with GFP and spike protein co-expressing HEK293T cells in the presence or absence of the endolysosomal cathepsin-inhibitor E64d (5 µM). Data are normalized to DMSO (N=6 images per condition). A two-sided independent Student's t-test was performed. Data are represented as means ± 95% CI of three independent experiments. *p < 0.05, **p < 0.01, ***p < 0.001. Figure retrieved from (Jocher et al., 2022).

5 DISCUSSION

The multitude of interesting functions of ADAM17 in regulating crucial aspects of development and adult homeostasis are well-documented (Zunke and Rose-John, 2017), but how exactly ADAM17 contributes to Alzheimer's disease and COVID-19 is largely unknown. To shed light on the pathophysiology of ADAM17 in these diseases, my doctoral thesis focused on ADAM17-dependent proteolytic processes in the context of AD and SARS-CoV-2 cell entry and pathogenesis. To better highlight the specific contributions of ADAM17 to these diseases, the functions of ADAM17 with regards to microglia biology and COVID-19 will be discussed in the following two separate sections.

5.1 Exploring iRHOM2 function in microglia

A major goal of this thesis was to characterize iRHOM2 in microglia, because previous studies established an epigenetically induced upregulation linked to late-onset Alzheimer's disease. To investigate iRHOM2 on the protein level, we concentrated our efforts on studying microglia, because this is the brain cell type exhibiting high *iRhom2* expression. Previous studies had elucidated the role of iRHOM2 in ADAM17 maturation, which led to a complete loss of ADAM17 activity in macrophages (Adrain et al., 2012; McIlwain et al., 2012a) and microglia (Li et al., 2015). Our results on primary microglia studying ADAM17 maturation and TNFa release after LPS stimulation in *iRhom2*$^{-/-}$ microglia support these findings.

To study consequences of loss of ADAM17 activity; we pursued our hypothesis that altered ectodomain shedding might affect the transcriptional state of microglia. Indeed, previous single-cell RNA sequencing studies of microglia had revealed different physiologically and disease-associated microglia states that were characterized by a different repertoire of cell surface proteins. (Hammond et al., 2019; Keren-Shaul et al., 2017). These proteins are typically potential shedding substrate candidates. In our bulk transcriptomic analysis intended to define the overall transcriptional profile of primary microglia, we found significantly upregulated proteins indicative of microglial activation in *iRhom2*$^{-/-}$ microglia. Among the most significantly changed transcripts, we found Clec7a, IL1b, and Cd11c (Itgax), which are known to be involved in innate immunity, response to Aß and tau pathology (Grubman et al., 2021; Jiang et al., 2021;

Krasemann et al., 2017). Interestingly, the top-regulated gene was the transcription factor c-JUN, a protein involved in cellular responses to oxidative stress (Shen and Liu, 2006). While these findings hinted towards an altered microglial state in *iRhom2*$^{-/-}$ microglia under steady-state conditions, it remains elusive how these altered transcripts affect cellular function on the molecular level.

We further extended our analysis to study the microglial secretome using the previously developed hiSPECS method (Tüshaus et al., 2020). Among the significantly altered proteins, we identified the well-described ADAM17 substrates CSF1R and TREM2, but also potential new substrates such as H2-K1, or H2-L. Since microglia are known to be activated during cell culture (Cadiz et al., 2022), the question arose whether these significantly changed substrates could also be physiological ADAM10 substrates. Notably, substrates that are either believed or actually proven to be shed by ADAM10 under physiological conditions, such as APP or Notch, remained unchanged in the secretome of *iRhom2*$^{-/-}$ microglia. This provides good evidence, that shedding of CSF1R, TREM2, H2-K1, and H2-L is indeed primarily controlled by ADAM17. We further substantiate these findings by the analysis of the cellular proteome of these cells by mass spectrometry. Remarkably, the loss of iRHOM2 does not affect cellular levels of TREM2, H2-K1 or H2-L1. In case of CSF1R, cellular levels actually increase in the absence of iRHOM2. This strengthens the idea that the reduced levels observed in the secretome can be attributed to restricted ectodomain shedding. CSF1R and TREM2 are important regulators of microglia function, and their molecular action has been well-documented. Among the two, TREM2 exhibits a pronounced and direct association with AD, which prompted us to further investigate the interplay between iRHOM2/ADAM17 and TREM2 biology.

While upregulation of TREM2 in *iRhom2*$^{-/-}$ microglia is not evident as determined with whole lysate proteomics, analysis of the membrane fraction of microglia lysate with Western blotting reveals higher levels of mature TREM2. Additionally, there is a noteworthy reduction in the levels of the soluble ectodomain of TREM2 in the supernatants of these cells. These findings suggest that ADAM17 plays a significant role in regulating the proteolytic release of TREM2, which aligns with a previous report (Feuerbach et al., 2017). Increased TREM2 surface levels have been shown to enhance downstream signaling and increased phagocytosis (Kleinberger et al., 2014; Schlepckow et al., 2020). Moreover, others reported increased phagocytosis of *iRhom2*$^{-/-}$ in monocyte-derived cell lines and bone-marrow-derived macrophages. The suggested molecular mechanism implied TNFa signaling as a major contributor to this phenotype (Seifert et al., 2020). We assessed phagocytosis of acutely isolated microglia, in which we find a significant increase of Aß-plaque clearance. Collectively, these results provide good evidence that TREM2 might be responsible for this phenotype in *iRhom2*$^{-/-}$ microglia. Indeed, previous work investigated the role of a TREM2-cleavage resistant mutant and compellingly, this particular isoform strongly upregulated phagocytosis of various substrates *in vitro* (Dhandapani et al., 2022). In parallel, another study that investigated the role of TREM2 in efferocytosis in a model of nonalcoholic steatohepatitis made similar observations. In this study, the clearance of lipid-laden hepatocytes was impaired due to upregulation of pro-inflammatory cytokines that stimulated ADAM17-dependent TREM2 shedding (Wang et al., 2023).

The role TREM2 is not only required for phagocytosis, but it controls also cell-autonomous programs pivotal for recycling of the ingested material. Thus, it is not surprising that studies identified TREM2 as a regulator for lipid metabolism, in particular being responsible for the management of cellular cholesterol through lipid droplets biogenesis (Gouna et al., 2021; Nugent et al., 2019). Lipid droplets are intracellular organelles that regulate storage of lipids and function as a central depot for cholesterol, which is critical for the maintenance of cellular membranes. Our investigations reveal the presence of an increased number of microglia bearing lipid droplets, which hints towards altered lipid droplet biogenesis in *iRhom2*-deficient microglia. A previous study had reported a similar phenotype in iPSC-derived microglia upon ADAM17 inhibition. The authors attributed this phenotype to the accumulation of reactive oxygen species which ultimately led to the occurrence of peroxidated lipids due to restricted TNFa signaling (Muliyil et al., 2020). Thus, further research is required to delineate the molecular cause of the lipid droplets phenotype elicited by loss of iRHOM2.

Taken together, we have explored fundamental aspects of iRHOM2/ADAM17 function in microglia; however, there are certain limitations to be addressed..Our in vitro studies are limited in that microglia cultures may only poorly represent the possible *in vivo* scenario. To precisely elucidate the effects of ADAM17-induced TREM2 cleavage, it would be desirable to compare a cleavage-resistant TREM2 mutant with TREM2 KO and loss of iRhom2 in parallel. Since ADAM17 activity is known to increase profoundly in inflammatory conditions, it would be advantageous to induce iRHOM2/ADAM17 experimentally.. Thus, *in vivo* studies that contain a strong pro-inflammatory component are promising for deciphering the effects of iRHOM2/ADAM17 on TREM2. Moreover, to address the question of which is the physiologically relevant sheddase, it will be important to examine the knockout of ADAM10 and ADAM17 in microglia *in vivo.* Despite the limitations of this study, the results presented in this thesis provide incentive to follow up on the study of iRHOM2, particularly in the context of TREM2 ectodomain shedding. Due to the emerging roles of TREM2 in myeloid biology, great efforts are underway to manipulate TREM2 function to treat neurodegenerative diseases (Schlepckow et al., 2020; van Lengerich et al., 2023). Thus, iRHOM2 inhibition to enhance TREM2 function represents a promising strategy for therapeutic intervention.

5.2 The role of ectodomain shedding in SARS-CoV-2 cell entry and pathogenesis

The presented results of the second part of this thesis shed light on two critical novel biological functions that contribute to the current understanding of SARS-CoV-2 infections and COVID-19. Firstly, we establish ADAM17 as a host factor that facilitates SARS-CoV-2 to infect lung cells. Secondly, we identify ADAM10 as the membrane-associated protease that causes the formation of lung cell syncytia, which is a characteristic frequently observed pathological feature in the lungs of patients with COVID-19.

The metalloproteases ADAM10 and ADAM17 are closely related and they are recognized as important members of the so-called full-time sheddases, due to their major functions in proteolytic ectodomain shedding (Lichtenthaler et al., 2018). Although both proteases are known to have an overlapping substrate repertoire *in vitro*, there are numerous studies highlighting their different roles in health and disease. In this thesis, we uncover novel and distinct roles of ADAM10 and ADAM17 on SARS-CoV-2 cell entry and pathology.

Employing pharmacological inhibitors and genetic ablation models, we demonstrate that ACE2 ectodomain shedding is mediated by both ADAM10 and ADAM17. We also show that ACE2 cleavage is neither fully depleted by the genetic ablation of these two ADAMs nor by a pan-metalloprotease inhibition using BB94. This suggests that there is still room for other proteases to contribute to ACE2 shedding. In fact, a recent report demonstrated that in particular MMP14 (MT1-MMP) controls ACE2 cleavage in primary human airway epithelial cells, suggesting that there is at least one other major protease besides ADAM10/17, contributing to ACE2 ectodomain shedding (Guo et al., 2022). We directed our experiments towards the question whether ACE2-shedding by ADAM10/17 would impact on SARS-CoV-2 cell entry. Indeed, we find that an array of different inhibitors – with members of low and high specificity towards ADAM17 – can potently block SARS-CoV-2 spread in A549-ACE2 cells, and most importantly, also in primary bronchial epithelial cells. Remarkably, inhibition of metalloproteases and cathepsins exert synergistic effects on SARS-CoV-2 entry in the A549-ACE2 cells, which shows that they act on separate entry pathways. Viral entry in primary lung cells can be blocked only upon triple inhibition because they also have the TMPRSS2 entry pathway available. This shows, that the ADAM metalloprotease pathway is a novel entry route for SARS-CoV-2.

Rapid viral mutagenesis is a common feature of quickly spreading and pathogenic strains. However, it is imperative to experimentally examine whether these evolved strains exploit similar entry pathways (Harvey et al., 2021). We studied several prevalent variants of concern and find that metalloprotease inhibition effectively blocks the alpha, beta, and delta variants, but is less effective against the omicron strain. Others had reported opposite results finding metalloproteases more important for omicron infection than previous strains (Chan et al., 2023). The discrepancies are likely attributable to the specific omicron subvariant and the cellular systems being used in these studies.

Preventing SARS-CoV-2 spread *in vivo* is crucial for the effective treatment of infected patients. The emergence of new viral strains often presents a challenge as effective therapies are generally scarce, largely due to the incomplete understanding of the molecular mechanisms underlying the pathogenesis. A promising emerging therapeutic approach, which has the potential to be effective against any coronavirus that utilizes ACE2 as the entry receptor, involves administering the recombinantly produced ACE2 to patients (Monteil et al., 2022). In principle, the S-protein binding site of ACE2 should be sufficient to effectively decoy SARS-CoV-2 (Shoemaker et al., 2022). However, recent studies have questioned this therapeutic option, merely due to the discovery of an entry pathway that depends on soluble ACE2 binding to the AT1-receptor (Yeung et al., 2021) and involved receptor-mediated endocytosis through

ACE2 cleavage by MMP14 (Guo et al., 2022). In our study, we find that both ADAM10 and ADAM17 contribute to ACE2 shedding, but only ADAM10 mediated the entry of SARS-CoV-2 pseudotyped particles. In contrast, infection of lung cells with authentic SARS-CoV-2 is synergistically mediated by both ADAM10 and ADAM17. Interestingly, the strong ADAM17 activator PMA increases ACE2 shedding and viral infection, but soluble ACE2 blocks pseudotype entry. Given these discrepancies, we conclude that ADAM10 and ADAM17 adopt different roles in SARS-CoV-2 entry, and that ACE2 cleavage could contribute to it, but is unlikely to be the only mechanism responsible for this effect.

The coronavirus spike protein requires cleavage at the S2’ site for infection and the subcellular location of the proteolytic event dictates viral entry (Dittmar et al., 2021). In light of our discoveries that ADAM10 and ADAM17 facilitate viral entry independently of the cathepsin and the TMPRRS2 pathway, we deliver multiple lines of evidence that ADAMs act mechanistically on spike protein cleavage. First, we show that in an in vitro cleavage assay both ADAM10 and ADAM17 can cleave the spike protein directly on the S2’ site similar to the cleavage observed with TMPRRS2. Second, we demonstrate that the spike protein located on authentic SARS-CoV-2 virions can directly interact with ADAM17 on the cell surface, and thirdly, we show that ADAM10 is responsible for spike protein cleavage required for syncytia formation, which is a critical pathological feature in the lungs of COVID-19 patients (Buchrieser et al., 2020; Bussani et al., 2020) and involves the fusion of infected cells that express the S protein with cells expressing the ACE2 receptor. Syncytia formation is frequently used as a readout to demonstrate spike protein cleavage at the S2’ site (Buchrieser et al, 2020; Ou et al, 2020). While earlier studies did not establish a necessity for ADAM10 or other ADAM proteases in syncytia formation, it is noteworthy that some studies observed cell fusion to be hindered by broad-spectrum metalloprotease inhibitors, which can also inhibit ADAM10 (Nguyen et al, 2020; Hörnich et al, 2021). Additionally, ionomycin, a calcium ionophore known to facilitate the cleavage of ADAM10 and ADAM17 substrates (Horiuchi et al, 2007; Le Gall et al, 2009), was found to promote cell fusion (Braga et al, 2021). This evidence aligns with our discovery that ADAM10 is critical for efficient cell fusion.

It is important to mention that multiple studies conducted concurrently with ours largely confirmed our findings. For instance, a study by Harte et al. (2022) showed ADAM17 cleaves the spike protein in a cellular system, and found a significant, albeit less strong, involvement of ACE2 cleavage to be facilitating SARS-CoV-2 entry (Harte et al., 2022). This shows that multiple proteolytic cleavage events could be in place simultaneously. Interestingly, there is some disagreement regarding the comparability between pseudotyped and authentic SARS-CoV-2 viruses. Our findings suggest that pseudotyped VSV-S particles infiltrate cells via ADAM10 in A549-ACE2 cells, with reports indicating similar behavior in other cell types (Yamamoto et al., 2022). However, in our experiments, the genuine SARS-CoV-2 (MUC-IMB) infiltrates A549-ACE2 predominantly through ADAM17, while other studies observed ADAM17's involvement primarily with the omicron variant (Chan et al., 2023). Therefore, it remains a topic for future investigation to determine the precise degree to which a particular metalloprotease contributes to SARS-CoV-2 entry and pathogenesis.

Taken together, our work establishes ADAM10 and ADAM17 as important host factors for SARS-CoV-2 cell entry and pathogenesis. The findings enrich the pertinent scientific literature by revealing a previously undiscovered cellular entry pathway for the SARS-CoV-2 virus. This contribution aligns with a growing body of studies underscoring the pivotal role of metalloproteases in SARS-CoV-2. Although the exact contribution of a certain metalloprotease *in vivo* is yet to be defined, it is conceivable that metalloproteases could serve as viable drug targets in the context of COVID-19. Consequently, this work lays a robust groundwork for designing further research studies for the better treatment of COVID-19.

5.3 The pathophysiological functions of ADAM17 in Alzheimer’s disease and COVID-19

The pathophysiological processes of ADAM17 are inherently linked to it’s role in proteolytic processing of numerous substrates. Thus, systematic identification of protease substrates is pivotal to unravel these biological secrets and offers new opportunities for therapeutic intervention. The research on the ADAM17 substrates TREM2, ACE2, and the SARS-CoV-2 spike protein within the context of AD and COVID-19 further enriches our knowledge of important ADAM17 functions, inevitably spurring motivation for future studies.

6 CONCLUSION AND FUTURE PERSPECTIVE

In summary, the main goal of this thesis was to provide new insights of the biology of the alpha-secretases ADAM10 and ADAM17 with an emphasis on shedding TREM2 in the context of Alzheimer's disease and as host factors for SARS-CoV-2.

The role of iRHOM2/ADAM17 in the shedding of TREM2 in microglia is an important aspect of membrane proteolysis that will undoubtedly continue to be researched. This is because TREM2 is such an essential protein for the biology of myeloid cells. Our work touches on some aspects of this biology and will set the stage for future experiments so that therapeutic approaches through the inhibition of iRHOM2/ADAM17 to increase TREM2 activity can become a reality.

The establishment of ADAM10 and ADAM17 as host factors for SARS-CoV-2 contributes to our understanding of the coronavirus pandemic. Above all, the identification of a new entry pathway for this virus could help protect against coronaviruses, which have an unanticipated plasticity in their spike protein enabling them to infect a cell in many different ways. In addition, it can be assumed that the efforts to inhibit individual host cell proteases will not be sufficient in the case of coronavirus, but rather combination approaches will have to be resorted to. At the same time, however, this may lead to organ-specific treatments where the inhibition of individual proteases will be more important than others. Further studies are necessary, in order to precisely define the ratio of cell entry pathways in the different tissues. Another important point is the prevention of possible vaccine side effects, in which the spike protein may lead to the fusion of healthy body cells (Parry et al., 2023). It is certainly exciting to check whether and to what extent the fusogenic capacity of vaccine-induced spike proteins may depend on the metalloproteases.

The findings of this thesis will hopefully spark new perspectives in the field of ADAM biology in Alzheimer's disease and virology. It will surely be exciting to explore the feasibility of iRHOM2 inhibition for the treatment of diseases benefiting from TREM2 agonism. In the realm of virology, the finding that ADAM metalloproteases enable virus entry will hopefully provide incentive to explore whether other pathogenic viruses have developed similar mechanisms.

7 REFERENCES

Adrain, C., Zettl, M., Christova, Y., Taylor, N., and Freeman, M. (2012). Tumor necrosis factor signaling requires iRhom2 to promote trafficking and activation of TACE. Science (New York, NY) *335*, 225-228.

Atapattu, L., Saha, N., Llerena, C., Vail, M.E., Scott, A.M., Nikolov, D.B., Lackmann, M., and Janes, P.W. (2012). Antibodies binding the ADAM10 substrate recognition domain inhibit Eph function. Journal of cell science *125*, 6084-6093.

Ballard, C., Gauthier, S., Corbett, A., Brayne, C., Aarsland, D., and Jones, E. (2011). Alzheimer's disease. Lancet (London, England) *377*, 1019-1031.

Berner, D.K., Wessolowski, L., Armbrust, F., Schneppenheim, J., Schlepckow, K., Koudelka, T., Scharfenberg, F., Lucius, R., Tholey, A., Kleinberger, G., *et al.* (2020). Meprin β cleaves TREM2 and controls its phagocytic activity on macrophages. FASEB journal : official publication of the Federation of American Societies for Experimental Biology *34*, 6675-6687.

Black, R.A., Rauch, C.T., Kozlosky, C.J., Peschon, J.J., Slack, J.L., Wolfson, M.F., Castner, B.J., Stocking, K.L., Reddy, P., Srinivasan, S., *et al.* (1997). A metalloproteinase disintegrin that releases tumour-necrosis factor-alpha from cells. Nature *385*, 729-733.

Blobel, C.P. (2005). ADAMs: key components in EGFR signalling and development. Nature reviews Molecular cell biology *6*, 32-43.

Boehm, M., and Nabel, E.G. (2002). Angiotensin-converting enzyme 2--a new cardiac regulator. The New England journal of medicine *347*, 1795-1797.

Bosch-Queralt, M., Cantuti-Castelvetri, L., Damkou, A., Schifferer, M., Schlepckow, K., Alexopoulos, I., Lütjohann, D., Klose, C., Vaculčiaková, L., Masuda, T., *et al.* (2021). Diet-dependent regulation of TGFβ impairs reparative innate immune responses after demyelination. Nature metabolism *3*, 211-227.

Bramhall, S.R., Hallissey, M.T., Whiting, J., Scholefield, J., Tierney, G., Stuart, R.C., Hawkins, R.E., McCulloch, P., Maughan, T., Brown, P.D., *et al.* (2002). Marimastat as maintenance therapy for patients with advanced gastric cancer: a randomised trial. British journal of cancer *86*, 1864-1870.

Brummer, T., Pigoni, M., Rossello, A., Wang, H., Noy, P.J., Tomlinson, M.G., Blobel, C.P., and Lichtenthaler, S.F. (2018). The metalloprotease ADAM10 (a disintegrin and metalloprotease 10) undergoes rapid, postlysis autocatalytic degradation. FASEB journal : official publication of the Federation of American Societies for Experimental Biology *32*, 3560-3573.

Buchrieser, J., Dufloo, J., Hubert, M., Monel, B., Planas, D., Rajah, M.M., Planchais, C., Porrot, F., Guivel-Benhassine, F., Van der Werf, S., *et al.* (2020). Syncytia formation by SARS-CoV-2-infected cells. The EMBO journal *39*, e106267.

Bussani, R., Schneider, E., Zentilin, L., Collesi, C., Ali, H., Braga, L., Volpe, M.C., Colliva, A., Zanconati, F., Berlot, G., *et al.* (2020). Persistence of viral RNA, pneumocyte syncytia and thrombosis are hallmarks of advanced COVID-19 pathology. EBioMedicine *61*, 103104.

Buxbaum, J.D., Liu, K.N., Luo, Y., Slack, J.L., Stocking, K.L., Peschon, J.J., Johnson, R.S., Castner, B.J., Cerretti, D.P., and Black, R.A. (1998). Evidence that tumor necrosis factor alpha converting enzyme is involved in regulated alpha-secretase cleavage of the Alzheimer amyloid protein precursor. The Journal of biological chemistry *273*, 27765-27767.

REFERENCES

Cadiz, M.P., Jensen, T.D., Sens, J.P., Zhu, K., Song, W.M., Zhang, B., Ebbert, M., Chang, R., and Fryer, J.D. (2022). Culture shock: microglial heterogeneity, activation, and disrupted single-cell microglial networks in vitro. Molecular neurodegeneration *17*, 26.

Cantuti-Castelvetri, L., Fitzner, D., Bosch-Queralt, M., Weil, M.T., Su, M., Sen, P., Ruhwedel, T., Mitkovski, M., Trendelenburg, G., Lütjohann, D.*, et al.* (2018). Defective cholesterol clearance limits remyelination in the aged central nervous system. Science (New York, NY) *359*, 684-688.

Chan, J.F., Huang, X., Hu, B., Chai, Y., Shi, H., Zhu, T., Yuen, T.T., Liu, Y., Liu, H., Shi, J.*, et al.* (2023). Altered host protease determinants for SARS-CoV-2 Omicron. Science advances *9*, eadd3867.

Colombo, A., Dinkel, L., Müller, S.A., Sebastian Monasor, L., Schifferer, M., Cantuti-Castelvetri, L., König, J., Vidatic, L., Bremova-Ertl, T., Lieberman, A.P.*, et al.* (2021). Loss of NPC1 enhances phagocytic uptake and impairs lipid trafficking in microglia. Nature communications *12*, 1158.

De Jager, P.L., Srivastava, G., Lunnon, K., Burgess, J., Schalkwyk, L.C., Yu, L., Eaton, M.L., Keenan, B.T., Ernst, J., McCabe, C.*, et al.* (2014). Alzheimer's disease: early alterations in brain DNA methylation at ANK1, BIN1, RHBDF2 and other loci. Nature neuroscience *17*, 1156-1163.

De Strooper, B., Annaert, W., Cupers, P., Saftig, P., Craessaerts, K., Mumm, J.S., Schroeter, E.H., Schrijvers, V., Wolfe, M.S., Ray, W.J.*, et al.* (1999). A presenilin-1-dependent gamma-secretase-like protease mediates release of Notch intracellular domain. Nature *398*, 518-522.

Demichev, V., Messner, C.B., Vernardis, S.I., Lilley, K.S., and Ralser, M. (2020). DIA-NN: neural networks and interference correction enable deep proteome coverage in high throughput. Nature methods *17*, 41-44.

Dhandapani, R., Neri, M., Bernhard, M., Brzak, I., Schweizer, T., Rudin, S., Joller, S., Berth, R., Kernen, J., Neuhaus, A.*, et al.* (2022). Sustained Trem2 stabilization accelerates microglia heterogeneity and Aβ pathology in a mouse model of Alzheimer's disease. Cell reports *39*, 110883.

DiCarlo, G., Wilcock, D., Henderson, D., Gordon, M., and Morgan, D. (2001). Intrahippocampal LPS injections reduce Abeta load in APP+PS1 transgenic mice. Neurobiology of aging *22*, 1007-1012.

Dittmar, M., Lee, J.S., Whig, K., Segrist, E., Li, M., Kamalia, B., Castellana, L., Ayyanathan, K., Cardenas-Diaz, F.L., Morrisey, E.E.*, et al.* (2021). Drug repurposing screens reveal cell-type-specific entry pathways and FDA-approved drugs active against SARS-Cov-2. Cell reports *35*, 108959.

Dreymueller, D., Uhlig, S., and Ludwig, A. (2015). ADAM-family metalloproteinases in lung inflammation: potential therapeutic targets. American journal of physiology Lung cellular and molecular physiology *308*, L325-343.

Drummond, A.H., Beckett, P., Brown, P.D., Bone, E.A., Davidson, A.H., Galloway, W.A., Gearing, A.J., Huxley, P., Laber, D., McCourt, M.*, et al.* (1999). Preclinical and clinical studies of MMP inhibitors in cancer. Annals of the New York Academy of Sciences *878*, 228-235.

Feuerbach, D., Schindler, P., Barske, C., Joller, S., Beng-Louka, E., Worringer, K.A., Kommineni, S., Kaykas, A., Ho, D.J., Ye, C.*, et al.* (2017). ADAM17 is the main sheddase for the generation of human triggering receptor expressed in myeloid cells (hTREM2) ectodomain and cleaves TREM2 after Histidine 157. Neuroscience letters *660*, 109-114.

Gnirss, K., Kühl, A., Karsten, C., Glowacka, I., Bertram, S., Kaup, F., Hofmann, H., and Pöhlmann, S. (2012). Cathepsins B and L activate Ebola but not Marburg virus glycoproteins for efficient entry into cell lines and macrophages independent of TMPRSS2 expression. Virology *424*, 3-10.

Gouna, G., Klose, C., Bosch-Queralt, M., Liu, L., Gokce, O., Schifferer, M., Cantuti-Castelvetri, L., and Simons, M. (2021). TREM2-dependent lipid droplet biogenesis in phagocytes is required for remyelination. The Journal of experimental medicine *218*.

Grubman, A., Choo, X.Y., Chew, G., Ouyang, J.F., Sun, G., Croft, N.P., Rossello, F.J., Simmons, R., Buckberry, S., Landin, D.V.*, et al.* (2021). Transcriptional signature in microglia associated with Aβ plaque phagocytosis. Nature communications *12*, 3015.

Guerreiro, R., Wojtas, A., Bras, J., Carrasquillo, M., Rogaeva, E., Majounie, E., Cruchaga, C., Sassi, C., Kauwe, J.S., Younkin, S.*, et al.* (2013). TREM2 variants in Alzheimer's disease. The New England journal of medicine *368*, 117-127.

Guo, X., Cao, J., Cai, J.P., Wu, J., Huang, J., Asthana, P., Wong, S.K.K., Ye, Z.W., Gurung, S., Zhang, Y.*, et al.* (2022). Control of SARS-CoV-2 infection by MT1-MMP-mediated shedding of ACE2. Nature communications *13*, 7907.

Gupta, A., Madhavan, M.V., Sehgal, K., Nair, N., Mahajan, S., Sehrawat, T.S., Bikdeli, B., Ahluwalia, N., Ausiello, J.C., Wan, E.Y.*, et al.* (2020). Extrapulmonary manifestations of COVID-19. Nature medicine *26*, 1017-1032.

Haga, S., Yamamoto, N., Nakai-Murakami, C., Osawa, Y., Tokunaga, K., Sata, T., Yamamoto, N., Sasazuki, T., and Ishizaka, Y. (2008). Modulation of TNF-α-converting enzyme by the spike protein of SARS-CoV and ACE2 induces TNF-α production and facilitates viral entry. Proceedings of the National Academy of Sciences *105*, 7809-7814.

Haining, E.J., Yang, J., Bailey, R.L., Khan, K., Collier, R., Tsai, S., Watson, S.P., Frampton, J., Garcia, P., and Tomlinson, M.G. (2012). The TspanC8 subgroup of tetraspanins interacts with A disintegrin and metalloprotease 10 (ADAM10) and regulates its maturation and cell surface expression. The Journal of biological chemistry *287*, 39753-39765.

Hammond, T.R., Dufort, C., Dissing-Olesen, L., Giera, S., Young, A., Wysoker, A., Walker, A.J., Gergits, F., Segel, M., Nemesh, J.*, et al.* (2019). Single-Cell RNA Sequencing of Microglia throughout the Mouse Lifespan and in the Injured Brain Reveals Complex Cell-State Changes. Immunity *50*, 253-271.e256.

Harte, J.V., Wakerlin, S.L., Lindsay, A.J., McCarthy, J.V., and Coleman-Vaughan, C. (2022). Metalloprotease-Dependent S2'-Activation Promotes Cell-Cell Fusion and Syncytiation of SARS-CoV-2. Viruses *14*.

Hartl, D., May, P., Gu, W., Mayhaus, M., Pichler, S., Spaniol, C., Glaab, E., Bobbili, D.R., Antony, P., Koegelsberger, S.*, et al.* (2020). A rare loss-of-function variant of ADAM17 is associated with late-onset familial Alzheimer disease. Molecular psychiatry *25*, 629-639.

Harvey, W.T., Carabelli, A.M., Jackson, B., Gupta, R.K., Thomson, E.C., Harrison, E.M., Ludden, C., Reeve, R., Rambaut, A., Peacock, S.J.*, et al.* (2021). SARS-CoV-2 variants, spike mutations and immune escape. Nature reviews Microbiology *19*, 409-424.

Heitzler, P., and Simpson, P. (1991). The choice of cell fate in the epidermis of Drosophila. Cell *64*, 1083-1092.

Heneka, M.T., Carson, M.J., El Khoury, J., Landreth, G.E., Brosseron, F., Feinstein, D.L., Jacobs, A.H., Wyss-Coray, T., Vitorica, J., Ransohoff, R.M.*, et al.* (2015). Neuroinflammation in Alzheimer's disease. The Lancet Neurology *14*, 388-405.

Herber, D.L., Mercer, M., Roth, L.M., Symmonds, K., Maloney, J., Wilson, N., Freeman, M.J., Morgan, D., and Gordon, M.N. (2007). Microglial activation is required for

Abeta clearance after intracranial injection of lipopolysaccharide in APP transgenic mice. Journal of neuroimmune pharmacology : the official journal of the Society on NeuroImmune Pharmacology *2*, 222-231.

Herrlich, A., and Kefaloyianni, E. (2018). iRhoms: A Potential Path to More Specific Therapeutic Targeting of Lupus Nephritis. American journal of kidney diseases : the official journal of the National Kidney Foundation *72*, 617-619.

Heurich, A., Hofmann-Winkler, H., Gierer, S., Liepold, T., Jahn, O., and Pohlmann, S. (2014). TMPRSS2 and ADAM17 cleave ACE2 differentially and only proteolysis by TMPRSS2 augments entry driven by the severe acute respiratory syndrome coronavirus spike protein. Journal of virology *88*, 1293-1307.

Hoffmann, M., Hofmann-Winkler, H., and Pöhlmann, S. (2018). Priming Time: How Cellular Proteases Arm Coronavirus Spike Proteins. In Activation of Viruses by Host Proteases, E. Böttcher-Friebertshäuser, W. Garten, and H.D. Klenk, eds. (Cham: Springer International Publishing), pp. 71-98.

Hoffmann, M., Kleine-Weber, H., and Pohlmann, S. (2020). A Multibasic Cleavage Site in the Spike Protein of SARS-CoV-2 Is Essential for Infection of Human Lung Cells. Molecular cell.

Horiuchi, K., Le Gall, S., Schulte, M., Yamaguchi, T., Reiss, K., Murphy, G., Toyama, Y., Hartmann, D., Saftig, P., and Blobel, C.P. (2007). Substrate selectivity of epidermal growth factor-receptor ligand sheddases and their regulation by phorbol esters and calcium influx. Molecular biology of the cell *18*, 176-188.

Howard, L., Lu, X., Mitchell, S., Griffiths, S., and Glynn, P. (1996). Molecular cloning of MADM: a catalytically active mammalian disintegrin-metalloprotease expressed in various cell types. The Biochemical journal *317 (Pt 1)*, 45-50.

Hsia, H.E., Tüshaus, J., Brummer, T., Zheng, Y., Scilabra, S.D., and Lichtenthaler, S.F. (2019). Functions of 'A disintegrin and metalloproteases (ADAMs)' in the mammalian nervous system. Cellular and molecular life sciences : CMLS *76*, 3055-3081.

Hughes, C.S., Moggridge, S., Müller, T., Sorensen, P.H., Morin, G.B., and Krijgsveld, J. (2019). Single-pot, solid-phase-enhanced sample preparation for proteomics experiments. Nature protocols *14*, 68-85.

Imai, Y., Kuba, K., Rao, S., Huan, Y., Guo, F., Guan, B., Yang, P., Sarao, R., Wada, T., Leong-Poi, H.*, et al.* (2005). Angiotensin-converting enzyme 2 protects from severe acute lung failure. Nature *436*, 112-116.

Jendresen, C., Digre, A., Cui, H., Zhang, X., Vlodavsky, I., Li, J.P., and Nilsson, L.N.G. (2019). Systemic LPS-induced Aβ-solubilization and clearance in AβPP-transgenic mice is diminished by heparanase overexpression. Scientific reports *9*, 4600.

Jia, H.P., Look, D.C., Tan, P., Shi, L., Hickey, M., Gakhar, L., Chappell, M.C., Wohlford-Lenane, C., and McCray, P.B., Jr. (2009). Ectodomain shedding of angiotensin converting enzyme 2 in human airway epithelia. American journal of physiology Lung cellular and molecular physiology *297*, L84-96.

Jiang, S., Maphis, N.M., Binder, J., Chisholm, D., Weston, L., Duran, W., Peterson, C., Zimmerman, A., Mandell, M.A., Jett, S.D.*, et al.* (2021). Proteopathic tau primes and activates interleukin-1β via myeloid-cell-specific MyD88- and NLRP3-ASC-inflammasome pathway. Cell reports *36*, 109720.

Jocher, G., Grass, V., Tschirner, S.K., Riepler, L., Breimann, S., Kaya, T., Oelsner, M., Hamad, M.S., Hofmann, L.I., Blobel, C.P.*, et al.* (2022). ADAM10 and ADAM17 promote SARS-CoV-2 cell entry and spike protein-mediated lung cell fusion. EMBO reports, e54305.

Jorissen, E., Prox, J., Bernreuther, C., Weber, S., Schwanbeck, R., Serneels, L., Snellinx, A., Craessaerts, K., Thathiah, A., Tesseur, I.*, et al.* (2010). The disintegrin/metalloproteinase ADAM10 is essential for the establishment of the brain cortex. The Journal of neuroscience : the official journal of the Society for Neuroscience *30*, 4833-4844.

Jouannet, S., Saint-Pol, J., Fernandez, L., Nguyen, V., Charrin, S., Boucheix, C., Brou, C., Milhiet, P.E., and Rubinstein, E. (2016). TspanC8 tetraspanins differentially regulate the cleavage of ADAM10 substrates, Notch activation and ADAM10 membrane compartmentalization. Cellular and molecular life sciences : CMLS *73*, 1895-1915.

Keren-Shaul, H., Spinrad, A., Weiner, A., Matcovitch-Natan, O., Dvir-Szternfeld, R., Ulland, T.K., David, E., Baruch, K., Lara-Astaiso, D., Toth, B.*, et al.* (2017). A Unique Microglia Type Associated with Restricting Development of Alzheimer's Disease. Cell *169*, 1276-1290.e1217.

Kleinberger, G., Yamanishi, Y., Suárez-Calvet, M., Czirr, E., Lohmann, E., Cuyvers, E., Struyfs, H., Pettkus, N., Wenninger-Weinzierl, A., Mazaheri, F.*, et al.* (2014). TREM2 mutations implicated in neurodegeneration impair cell surface transport and phagocytosis. Science translational medicine *6*, 243ra286.

Kopan, R., and Ilagan, M.X. (2009). The canonical Notch signaling pathway: unfolding the activation mechanism. Cell *137*, 216-233.

Krasemann, S., Madore, C., Cialic, R., Baufeld, C., Calcagno, N., El Fatimy, R., Beckers, L., O'Loughlin, E., Xu, Y., Fanek, Z.*, et al.* (2017). The TREM2-APOE Pathway Drives the Transcriptional Phenotype of Dysfunctional Microglia in Neurodegenerative Diseases. Immunity *47*, 566-581.e569.

Kuba, K., Imai, Y., Rao, S., Gao, H., Guo, F., Guan, B., Huan, Y., Yang, P., Zhang, Y., Deng, W.*, et al.* (2005). A crucial role of angiotensin converting enzyme 2 (ACE2) in SARS coronavirus-induced lung injury. Nature medicine *11*, 875-879.

Kuhn, P.H., Colombo, A.V., Schusser, B., Dreymueller, D., Wetzel, S., Schepers, U., Herber, J., Ludwig, A., Kremmer, E., Montag, D.*, et al.* (2016). Systematic substrate identification indicates a central role for the metalloprotease ADAM10 in axon targeting and synapse function. eLife *5*.

Kuhn, P.H., Koroniak, K., Hogl, S., Colombo, A., Zeitschel, U., Willem, M., Volbracht, C., Schepers, U., Imhof, A., Hoffmeister, A.*, et al.* (2012). Secretome protein enrichment identifies physiological BACE1 protease substrates in neurons. The EMBO journal *31*, 3157-3168.

Kuhn, P.H., Wang, H., Dislich, B., Colombo, A., Zeitschel, U., Ellwart, J.W., Kremmer, E., Rossner, S., and Lichtenthaler, S.F. (2010). ADAM10 is the physiologically relevant, constitutive alpha-secretase of the amyloid precursor protein in primary neurons. The EMBO journal *29*, 3020-3032.

Kwon, H.S., and Koh, S.H. (2020). Neuroinflammation in neurodegenerative disorders: the roles of microglia and astrocytes. Translational neurodegeneration *9*, 42.

Lagares, D., Ghassemi-Kakroodi, P., Tremblay, C., Santos, A., Probst, C.K., Franklin, A., Santos, D.M., Grasberger, P., Ahluwalia, N., Montesi, S.B.*, et al.* (2017). ADAM10-mediated ephrin-B2 shedding promotes myofibroblast activation and organ fibrosis. Nature medicine *23*, 1405-1415.

Lambert, D.W., Yarski, M., Warner, F.J., Thornhill, P., Parkin, E.T., Smith, A.I., Hooper, N.M., and Turner, A.J. (2005). Tumor necrosis factor-alpha convertase (ADAM17) mediates regulated ectodomain shedding of the severe-acute respiratory syndrome-coronavirus (SARS-CoV) receptor, angiotensin-converting enzyme-2 (ACE2). The Journal of biological chemistry *280*, 30113-30119.

Lambert, J.C., Ibrahim-Verbaas, C.A., Harold, D., Naj, A.C., Sims, R., Bellenguez, C., DeStafano, A.L., Bis, J.C., Beecham, G.W., Grenier-Boley, B.*, et al.* (2013). Meta-analysis of 74,046 individuals identifies 11 new susceptibility loci for Alzheimer's disease. Nature genetics *45*, 1452-1458.

Lammich, S., Kojro, E., Postina, R., Gilbert, S., Pfeiffer, R., Jasionowski, M., Haass, C., and Fahrenholz, F. (1999). Constitutive and regulated alpha-secretase cleavage of Alzheimer's amyloid precursor protein by a disintegrin metalloprotease. Proceedings of the National Academy of Sciences of the United States of America *96*, 3922-3927.

Le Gall, S.M., Bobé, P., Reiss, K., Horiuchi, K., Niu, X.D., Lundell, D., Gibb, D.R., Conrad, D., Saftig, P., and Blobel, C.P. (2009). ADAMs 10 and 17 represent differentially regulated components of a general shedding machinery for membrane proteins such as transforming growth factor alpha, L-selectin, and tumor necrosis factor alpha. Molecular biology of the cell *20*, 1785-1794.

Le Gall, S.M., Maretzky, T., Issuree, P.D., Niu, X.D., Reiss, K., Saftig, P., Khokha, R., Lundell, D., and Blobel, C.P. (2010). ADAM17 is regulated by a rapid and reversible mechanism that controls access to its catalytic site. Journal of cell science *123*, 3913-3922.

Li, W., Moore, M.J., Vasilieva, N., Sui, J., Wong, S.K., Berne, M.A., Somasundaran, M., Sullivan, J.L., Luzuriaga, K., Greenough, T.C.*, et al.* (2003). Angiotensin-converting enzyme 2 is a functional receptor for the SARS coronavirus. Nature *426*, 450-454.

Li, X., Maretzky, T., Weskamp, G., Monette, S., Qing, X., Issuree, P.D.A., Crawford, H.C., McIlwain, D.R., Mak, T.W., Salmon, J.E.*, et al.* (2015). iRhoms 1 and 2 are essential upstream regulators of ADAM17-dependent EGFR signaling. Proceedings of the National Academy of Sciences *112*, 6080-6085.

Lichtenthaler, S.F., Dominguez, D.I., Westmeyer, G.G., Reiss, K., Haass, C., Saftig, P., De Strooper, B., and Seed, B. (2003). The cell adhesion protein P-selectin glycoprotein ligand-1 is a substrate for the aspartyl protease BACE1. The Journal of biological chemistry *278*, 48713-48719.

Lichtenthaler, S.F., Lemberg, M.K., and Fluhrer, R. (2018). Proteolytic ectodomain shedding of membrane proteins in mammals-hardware, concepts, and recent developments. The EMBO journal *37*.

Lipper, C.H., Egan, E.D., Gabriel, K.H., and Blacklow, S.C. (2023). Structural basis for membrane-proximal proteolysis of substrates by ADAM10. Cell *186*, 3632-3641.e3610.

Liu, J.M., Tan, B.H., Wu, S., Gui, Y., Suo, J.L., and Li, Y.C. (2021). Evidence of central nervous system infection and neuroinvasive routes, as well as neurological involvement, in the lethality of SARS-CoV-2 infection. Journal of medical virology *93*, 1304-1313.

Lorenzen, I., Lokau, J., Korpys, Y., Oldefest, M., Flynn, C.M., Künzel, U., Garbers, C., Freeman, M., Grötzinger, J., and Düsterhöft, S. (2016). Control of ADAM17 activity by regulation of its cellular localisation. Scientific reports *6*, 35067.

Maretzky, T., McIlwain, D.R., Issuree, P.D., Li, X., Malapeira, J., Amin, S., Lang, P.A., Mak, T.W., and Blobel, C.P. (2013). iRhom2 controls the substrate selectivity of stimulated ADAM17-dependent ectodomain shedding. Proceedings of the National Academy of Sciences of the United States of America *110*, 11433-11438.

Masters, P.S. (2006). The molecular biology of coronaviruses. Advances in virus research *66*, 193-292.

Matsuyama, S., Nao, N., Shirato, K., Kawase, M., Saito, S., Takayama, I., Nagata, N., Sekizuka, T., Katoh, H., Kato, F.*, et al.* (2020). Enhanced isolation of SARS-CoV-2 by TMPRSS2-expressing cells. Proceedings of the National Academy of Sciences *117*, 7001-7003.

McIlwain, D.R., Lang, P.A., Maretzky, T., Hamada, K., Ohishi, K., Maney, S.K., Berger, T., Murthy, A., Duncan, G., Xu, H.C.*, et al.* (2012a). iRhom2 Regulation of TACE Controls TNF-Mediated Protection Against Listeria and Responses to LPS. Science (New York, NY) *335*, 229-232.

McIlwain, D.R., Lang, P.A., Maretzky, T., Hamada, K., Ohishi, K., Maney, S.K., Berger, T., Murthy, A., Duncan, G., Xu, H.C.*, et al.* (2012b). iRhom2 regulation of TACE controls TNF-mediated protection against Listeria and responses to LPS. Science (New York, NY) *335*, 229-232.

Meier, F., Brunner, A.D., Frank, M., Ha, A., Bludau, I., Voytik, E., Kaspar-Schoenefeld, S., Lubeck, M., Raether, O., Bache, N.*, et al.* (2020). diaPASEF: parallel accumulation-serial fragmentation combined with data-independent acquisition. Nature methods *17*, 1229-1236.

Meilandt, W.J., Ngu, H., Gogineni, A., Lalehzadeh, G., Lee, S.H., Srinivasan, K., Imperio, J., Wu, T., Weber, M., Kruse, A.J.*, et al.* (2020). Trem2 Deletion Reduces Late-Stage Amyloid Plaque Accumulation, Elevates the Aβ42:Aβ40 Ratio, and Exacerbates Axonal Dystrophy and Dendritic Spine Loss in the PS2APP Alzheimer's Mouse Model. The Journal of neuroscience : the official journal of the Society for Neuroscience *40*, 1956-1974.

Michaud, J.P., Hallé, M., Lampron, A., Thériault, P., Préfontaine, P., Filali, M., Tribout-Jover, P., Lanteigne, A.M., Jodoin, R., Cluff, C.*, et al.* (2013). Toll-like receptor 4 stimulation with the detoxified ligand monophosphoryl lipid A improves Alzheimer's disease-related pathology. Proceedings of the National Academy of Sciences of the United States of America *110*, 1941-1946.

Mohler, K.M., Sleath, P.R., Fitzner, J.N., Cerretti, D.P., Alderson, M., Kerwar, S.S., Torrance, D.S., Otten-Evans, C., Greenstreet, T., Weerawarna, K.*, et al.* (1994). Protection against a lethal dose of endotoxin by an inhibitor of tumour necrosis factor processing. Nature *370*, 218-220.

Monteil, V., Eaton, B., Postnikova, E., Murphy, M., Braunsfeld, B., Crozier, I., Kricek, F., Niederhöfer, J., Schwarzböck, A., Breid, H.*, et al.* (2022). Clinical grade ACE2 as a universal agent to block SARS-CoV-2 variants. EMBO molecular medicine *14*, e15230.

Moss, M.L., Bomar, M., Liu, Q., Sage, H., Dempsey, P., Lenhart, P.M., Gillispie, P.A., Stoeck, A., Wildeboer, D., Bartsch, J.W.*, et al.* (2007). The ADAM10 prodomain is a specific inhibitor of ADAM10 proteolytic activity and inhibits cellular shedding events. The Journal of biological chemistry *282*, 35712-35721.

Moss, M.L., Jin, S.L., Milla, M.E., Bickett, D.M., Burkhart, W., Carter, H.L., Chen, W.J., Clay, W.C., Didsbury, J.R., Hassler, D.*, et al.* (1997). Cloning of a disintegrin metalloproteinase that processes precursor tumour-necrosis factor-alpha. Nature *385*, 733-736.

Moss, M.L., Sklair-Tavron, L., and Nudelman, R. (2008). Drug insight: tumor necrosis factor-converting enzyme as a pharmaceutical target for rheumatoid arthritis. Nature clinical practice Rheumatology *4*, 300-309.

Muliyil, S., Levet, C., Düsterhöft, S., Dulloo, I., Cowley, S.A., and Freeman, M. (2020). ADAM17-triggered TNF signalling protects the ageing Drosophila retina from lipid droplet-mediated degeneration. The EMBO journal *39*, e104415.

Niehues, R.V., Wozniak, J., Wiersch, F., Lilienthal, E., Tacken, N., Schumertl, T., Garbers, C., Ludwig, A., and Düsterhöft, S. (2022). The collectrin-like part of the

SARS-CoV-1 and -2 receptor ACE2 is shed by the metalloproteinases ADAM10 and ADAM17. FASEB journal : official publication of the Federation of American Societies for Experimental Biology *36*, e22234.

Nugent, A.A., Lin, K., van Lengerich, B., Lianoglou, S., Przybyla, L., Davis, S.S., Llapashtica, C., Wang, J., Kim, D.J., Xia, D.*, et al.* (2019). TREM2 Regulates Microglial Cholesterol Metabolism upon Chronic Phagocytic Challenge. Neuron.

Pan, D., and Rubin, G.M. (1997). Kuzbanian controls proteolytic processing of Notch and mediates lateral inhibition during Drosophila and vertebrate neurogenesis. Cell *90*, 271-280.

Paolicelli, R.C., Sierra, A., Stevens, B., Tremblay, M.E., Aguzzi, A., Ajami, B., Amit, I., Audinat, E., Bechmann, I., Bennett, M.*, et al.* (2022). Microglia states and nomenclature: A field at its crossroads. Neuron *110*, 3458-3483.

Park, J.E., Li, K., Barlan, A., Fehr, A.R., Perlman, S., McCray, P.B., Jr., and Gallagher, T. (2016). Proteolytic processing of Middle East respiratory syndrome coronavirus spikes expands virus tropism. Proceedings of the National Academy of Sciences of the United States of America *113*, 12262-12267.

Parry, P.I., Lefringhausen, A., Turni, C., Neil, C.J., Cosford, R., Hudson, N.J., and Gillespie, J. (2023). 'Spikeopathy': COVID-19 Spike Protein Is Pathogenic, from Both Virus and Vaccine mRNA. Biomedicines *11*.

Peschon, J.J., Slack, J.L., Reddy, P., Stocking, K.L., Sunnarborg, S.W., Lee, D.C., Russell, W.E., Castner, B.J., Johnson, R.S., Fitzner, J.N.*, et al.* (1998). An essential role for ectodomain shedding in mammalian development. Science (New York, NY) *282*, 1281-1284.

Qiao, X., Cummins, D.J., and Paul, S.M. (2001). Neuroinflammation-induced acceleration of amyloid deposition in the APPV717F transgenic mouse. The European journal of neuroscience *14*, 474-482.

Riepler, L., Rössler, A., Falch, A., Volland, A., Borena, W., von Laer, D., and Kimpel, J. (2020). Comparison of Four SARS-CoV-2 Neutralization Assays. Vaccines *9*.

Robinson, M.D., McCarthy, D.J., and Smyth, G.K. (2010). edgeR: a Bioconductor package for differential expression analysis of digital gene expression data. Bioinformatics (Oxford, England) *26*, 139-140.

Rooke, J., Pan, D., Xu, T., and Rubin, G.M. (1996). KUZ, a conserved metalloprotease-disintegrin protein with two roles in Drosophila neurogenesis. Science (New York, NY) *273*, 1227-1231.

Rosenbaum, D., and Saftig, P. (2023). New insights into the function and pathophysiology of the ectodomain sheddase A Disintegrin And Metalloproteinase 10 (ADAM10). The FEBS journal.

Schiffman, C., McHale, C.M., Hubbard, A.E., Zhang, L., Thomas, R., Vermeulen, R., Li, G., Shen, M., Rappaport, S.M., Yin, S.*, et al.* (2018). Identification of gene expression predictors of occupational benzene exposure. PloS one *13*, e0205427.

Schlepckow, K., Kleinberger, G., Fukumori, A., Feederle, R., Lichtenthaler, S.F., Steiner, H., and Haass, C. (2017). An Alzheimer-associated TREM2 variant occurs at the ADAM cleavage site and affects shedding and phagocytic function. EMBO molecular medicine *9*, 1356-1365.

Schlepckow, K., Monroe, K.M., Kleinberger, G., Cantuti-Castelvetri, L., Parhizkar, S., Xia, D., Willem, M., Werner, G., Pettkus, N., Brunner, B.*, et al.* (2020). Enhancing protective microglial activities with a dual function TREM2 antibody to the stalk region. EMBO molecular medicine *12*, e11227.

Schlöndorff, J., Becherer, J.D., and Blobel, C.P. (2000). Intracellular maturation and localization of the tumour necrosis factor alpha convertase (TACE). The Biochemical journal *347 Pt 1*, 131-138.

Sebastian Monasor, L., Müller, S.A., Colombo, A.V., Tanrioever, G., König, J., Roth, S., Liesz, A., Berghofer, A., Piechotta, A., Prestel, M.*, et al.* (2020). Fibrillar Aβ triggers microglial proteome alterations and dysfunction in Alzheimer mouse models. eLife *9*.

Seifert, A., Wozniak, J., Düsterhöft, S., Kasparek, P., Sedlacek, R., Dreschers, S., Orlikowsky, T.W., Yildiz, D., and Ludwig, A. (2020). The iRhom2/ADAM17 Axis Attenuates Bacterial Uptake by Phagocytes in a Cell Autonomous Manner. International journal of molecular sciences *21*.

Shema Mugisha, C., Vuong, H.R., Puray-Chavez, M., Bailey, A.L., Fox, J.M., Chen, R.E., Wessel, A.W., Scott, J.M., Harastani, H.H., Boon, A.C.M.*, et al.* (2020). A Simplified Quantitative Real-Time PCR Assay for Monitoring SARS-CoV-2 Growth in Cell Culture. mSphere *5*.

Shen, H.M., and Liu, Z.G. (2006). JNK signaling pathway is a key modulator in cell death mediated by reactive oxygen and nitrogen species. Free radical biology & medicine *40*, 928-939.

Shoemaker, R.H., Panettieri, R.A., Jr., Libutti, S.K., Hochster, H.S., Watts, N.R., Wingfield, P.T., Starkl, P., Pimenov, L., Gawish, R., Hladik, A.*, et al.* (2022). Development of an aerosol intervention for COVID-19 disease: Tolerability of soluble ACE2 (APN01) administered via nebulizer. PloS one *17*, e0271066.

Simmons, G., Gosalia, D.N., Rennekamp, A.J., Reeves, J.D., Diamond, S.L., and Bates, P. (2005). Inhibitors of cathepsin L prevent severe acute respiratory syndrome coronavirus entry. Proceedings of the National Academy of Sciences of the United States of America *102*, 11876-11881.

Sims, R., van der Lee, S.J., Naj, A.C., Bellenguez, C., Badarinarayan, N., Jakobsdottir, J., Kunkle, B.W., Boland, A., Raybould, R., Bis, J.C.*, et al.* (2017). Rare coding variants in PLCG2, ABI3, and TREM2 implicate microglial-mediated innate immunity in Alzheimer's disease. Nature genetics *49*, 1373-1384.

Sjöstedt, E., Zhong, W., Fagerberg, L., Karlsson, M., Mitsios, N., Adori, C., Oksvold, P., Edfors, F., Limiszewska, A., Hikmet, F.*, et al.* (2020). An atlas of the protein-coding genes in the human, pig, and mouse brain. Science (New York, NY) *367*.

Skeggs, L.T., Dorer, F.E., Levine, M., Lentz, K.E., and Kahn, J.R. (1980). The biochemistry of the renin-angiotensin system. Advances in experimental medicine and biology *130*, 1-27.

Srinivasan, K., Friedman, B.A., Larson, J.L., Lauffer, B.E., Goldstein, L.D., Appling, L.L., Borneo, J., Poon, C., Ho, T., Cai, F.*, et al.* (2016). Untangling the brain's neuroinflammatory and neurodegenerative transcriptional responses. Nature communications *7*, 11295.

Stachel, S.J., Coburn, C.A., Steele, T.G., Jones, K.G., Loutzenhiser, E.F., Gregro, A.R., Rajapakse, H.A., Lai, M.T., Crouthamel, M.C., Xu, M.*, et al.* (2004). Structure-based design of potent and selective cell-permeable inhibitors of human beta-secretase (BACE-1). Journal of medicinal chemistry *47*, 6447-6450.

Tape, C.J., Willems, S.H., Dombernowsky, S.L., Stanley, P.L., Fogarasi, M., Ouwehand, W., McCafferty, J., and Murphy, G. (2011). Cross-domain inhibition of TACE ectodomain. Proceedings of the National Academy of Sciences of the United States of America *108*, 5578-5583.

Tegally, H., Wilkinson, E., Giovanetti, M., Iranzadeh, A., Fonseca, V., Giandhari, J., Doolabh, D., Pillay, S., San, E.J., Msomi, N.*, et al.* (2020). Emergence and rapid spread of a new severe acute respiratory syndrome-related coronavirus 2 (SARS-CoV-2) lineage with multiple spike mutations in South Africa. medRxiv, 2020.2012.2021.20248640.

Thi Nhu Thao, T., Labroussaa, F., Ebert, N., V'Kovski, P., Stalder, H., Portmann, J., Kelly, J., Steiner, S., Holwerda, M., Kratzel, A.*, et al.* (2020). Rapid reconstruction of SARS-CoV-2 using a synthetic genomics platform. Nature *582*, 561-565.

Tüshaus, J., Müller, S.A., Kataka, E.S., Zaucha, J., Sebastian Monasor, L., Su, M., Güner, G., Jocher, G., Tahirovic, S., Frishman, D.*, et al.* (2020). An optimized quantitative proteomics method establishes the cell type-resolved mouse brain secretome. The EMBO journal *39*, e105693.

Tüshaus, J., Müller, S.A., Shrouder, J., Arends, M., Simons, M., Plesnila, N., Blobel, C.P., and Lichtenthaler, S.F. (2021). The pseudoprotease iRhom1 controls ectodomain shedding of membrane proteins in the nervous system. FASEB journal : official publication of the Federation of American Societies for Experimental Biology *35*, e21962.

Tyanova, S., Temu, T., Sinitcyn, P., Carlson, A., Hein, M.Y., Geiger, T., Mann, M., and Cox, J. (2016). The Perseus computational platform for comprehensive analysis of (prote)omics data. Nature methods *13*, 731-740.

van Lengerich, B., Zhan, L., Xia, D., Chan, D., Joy, D., Park, J.I., Tatarakis, D., Calvert, M., Hummel, S., Lianoglou, S.*, et al.* (2023). A TREM2-activating antibody with a blood-brain barrier transport vehicle enhances microglial metabolism in Alzheimer's disease models. Nature neuroscience *26*, 416-429.

Vassar, R., Bennett, B.D., Babu-Khan, S., Kahn, S., Mendiaz, E.A., Denis, P., Teplow, D.B., Ross, S., Amarante, P., Loeloff, R.*, et al.* (1999). Beta-secretase cleavage of Alzheimer's amyloid precursor protein by the transmembrane aspartic protease BACE. Science (New York, NY) *286*, 735-741.

Walls, A.C., Park, Y.J., Tortorici, M.A., Wall, A., McGuire, A.T., and Veesler, D. (2020). Structure, Function, and Antigenicity of the SARS-CoV-2 Spike Glycoprotein. Cell *181*, 281-292.e286.

Walls, A.C., Tortorici, M.A., Bosch, B.J., Frenz, B., Rottier, P.J.M., DiMaio, F., Rey, F.A., and Veesler, D. (2016a). Cryo-electron microscopy structure of a coronavirus spike glycoprotein trimer. Nature *531*, 114-117.

Walls, A.C., Tortorici, M.A., Frenz, B., Snijder, J., Li, W., Rey, F.A., DiMaio, F., Bosch, B.J., and Veesler, D. (2016b). Glycan shield and epitope masking of a coronavirus spike protein observed by cryo-electron microscopy. Nature structural & molecular biology *23*, 899-905.

Wang, H., Horbinski, C., Wu, H., Liu, Y., Sheng, S., Liu, J., Weiss, H., Stromberg, A.J., and Wang, C. (2016). NanoStringDiff: a novel statistical method for differential expression analysis based on NanoString nCounter data. Nucleic acids research *44*, e151.

Wang, X., He, Q., Zhou, C., Xu, Y., Liu, D., Fujiwara, N., Kubota, N., Click, A., Henderson, P., Vancil, J.*, et al.* (2023). Prolonged hypernutrition impairs TREM2-dependent efferocytosis to license chronic liver inflammation and NASH development. Immunity *56*, 58-77.e11.

Weis, M., and Maisner, A. (2015). Nipah virus fusion protein: Importance of the cytoplasmic tail for endosomal trafficking and bioactivity. European journal of cell biology *94*, 316-322.

Weskamp, G., Tushaus, J., Li, D., Feederle, R., Maretzky, T., Swendeman, S., Falck-Pedersen, E., McIlwain, D.R., Mak, T.W., Salmon, J.E.*, et al.* (2020). ADAM17 stabilizes its interacting partner inactive Rhomboid 2 (iRhom2) but not inactive Rhomboid 1 (iRhom1). The Journal of biological chemistry.

Wetzel, S., Seipold, L., and Saftig, P. (2017). The metalloproteinase ADAM10: A useful therapeutic target? Biochimica et biophysica acta Molecular cell research *1864*, 2071-2081.

Wong, E., Cohen, T., Romi, E., Levin, M., Peleg, Y., Arad, U., Yaron, A., Milla, M.E., and Sagi, I. (2016). Harnessing the natural inhibitory domain to control TNFalpha Converting Enzyme (TACE) activity in vivo. Scientific reports *6*, 35598.

Wong, E., Maretzky, T., Peleg, Y., Blobel, C.P., and Sagi, I. (2015). The Functional Maturation of A Disintegrin and Metalloproteinase (ADAM) 9, 10, and 17 Requires Processing at a Newly Identified Proprotein Convertase (PC) Cleavage Site. The Journal of biological chemistry *290*, 12135-12146.

Yamamoto, M., Gohda, J., Kobayashi, A., Tomita, K., Hirayama, Y., Koshikawa, N., Seiki, M., Semba, K., Akiyama, T., Kawaguchi, Y.*, et al.* (2022). Metalloproteinase-Dependent and TMPRSS2-Independent Cell Surface Entry Pathway of SARS-CoV-2 Requires the Furin Cleavage Site and the S2 Domain of Spike Protein. mBio *13*, e0051922.

Yeung, M.L., Teng, J.L.L., Jia, L., Zhang, C., Huang, C., Cai, J.P., Zhou, R., Chan, K.H., Zhao, H., Zhu, L.*, et al.* (2021). Soluble ACE2-mediated cell entry of SARS-CoV-2 via interaction with proteins related to the renin-angiotensin system. Cell.

Zhao, Y., Dávila, E.M., Li, X., Tang, B., Rabinowitsch, A.I., Perez-Aguilar, J.M., and Blobel, C.P. (2022). Identification of Molecular Determinants in iRhoms1 and 2 That Contribute to the Substrate Selectivity of Stimulated ADAM17. International journal of molecular sciences *23*.

Zhou, B.B., Peyton, M., He, B., Liu, C., Girard, L., Caudler, E., Lo, Y., Baribaud, F., Mikami, I., Reguart, N.*, et al.* (2006). Targeting ADAM-mediated ligand cleavage to inhibit HER3 and EGFR pathways in non-small cell lung cancer. Cancer cell *10*, 39-50.

Zhu, Y., Feng, F., Hu, G., Wang, Y., Yu, Y., Zhu, Y., Xu, W., Cai, X., Sun, Z., Han, W.*, et al.* (2021). A genome-wide CRISPR screen identifies host factors that regulate SARS-CoV-2 entry. Nature communications *12*, 961.

Zocchi, M.R., Camodeca, C., Nuti, E., Rossello, A., Venè, R., Tosetti, F., Dapino, I., Costa, D., Musso, A., and Poggi, A. (2016). ADAM10 new selective inhibitors reduce NKG2D ligand release sensitizing Hodgkin lymphoma cells to NKG2D-mediated killing. Oncoimmunology *5*, e1123367.

Zunke, F., and Rose-John, S. (2017). The shedding protease ADAM17: Physiology and pathophysiology. Biochimica et biophysica acta Molecular cell research *1864*, 2059-2070.

8 APPENDIX

8.1 Appendix 1: Point-to-point protocol: hiSPECS analysis of primary microglia supernatant

Cell Culture:

- Seed cells (1 Mio. per 6-well)
- At day 3 in culture exchange media to F12-DMEM (P/S) +10% FBS + ManNAz (50 mM stock; 1:1000)
- Wash cells 1x with PBS
- Add 1 ml medium + ManNAz to each well of a 6-well plate
- Grow your cells in ManNAz (50 µM) containing medium
- Harvest supernatant 72 hours after ManNAz labeling. Filter through 0.45 µM centrifuge tubes, add PI (1:500) (Do not add EDTA!),
-

ConA/WGA enrichment:

Note: Do not add EDTA! ; Cut-off tip to avoid shearing of the beads; Don't spin beads higher than 4000 rpm, use 1.5mL low binding tubes

- For 0.9 mL medium use 50 µL ConA + 50 µl WGA beads, vortex before!
- Wash total ConA/WGA beads (in 2ml Eppi) 2x with 1 mL Binding buffer to get rid of ethanol.
  - centrifuge on table top centrifuge 2000g 1min, take off sup
- Bead distribution
  - Fill up beads with binding buffer up to max. volume
  - Divide total bead-buffer volume by (# of samples +1)
  - Distribute calculated volume to all samples
  - Refill remaining beads to max. volume
  - Distribute calculated volume again to all samples
- Add 1 mL Medium to the ConA/WGA beads and rotate at least 2h 4°C
  (If tube not full add binding buffer to prevent drying of the beads)
- Spin down with 2000g 1 min and take off supernatant (these are the unbound proteins)
- 3x wash with Binding buffer (rotate 1min over-head, spin down before taking off supernatant)

- Add 500 µL Elution buffer (Combine 250mM ConA + 250 mM WGA elution buffer) to ConA/WGA beads and rotate over-head 30 min; spin down
- Place supernatant into Pierce Spin Column (filter beads!)
- Repeat elution step with another 500 µL Elution buffer
- Place filtered eluate into a fresh 1.5 mL loBind tube

Click to magnetic DBCO beads:

- Wash the Magnetic DBCO beads (50 µL per 1 mL Supernatant) 2x with 1mL mass spec grade $H2O$ in low binding tube; 1.5 mL at RT in magnetic rack.!
- Distribute DBCO beads as before-mentioned.
- Add filtered Eluate to the magnetic beads and shake o/n (16h) at 4°C 1200 rpm-

Washing of magnetic beads:

- Wash beads 3x 1 mL with SDS buffer without SDC; shake briefly at 1200 rpm RT
- Wash beads 3x 1 mL with 8 M UREA buffer with 0.1% SDC; rotate briefly;
- Wash beads 3x1 mL with 20% acetonitrile with 0.1% SDC; rotate briefly;
- Add 2x 500 µL mass spec grade dH2O with 0.1% SDC, resuspend beads and transfer them to a new 1.5 mL low binding tube
- Discard SN > beads should be dry before adding DTT

- Denaturation:
  - Add 50 µL of 10mM DTT in 100mM ABC with 0.1% SDC
  - Incubate 30 min at 1200 rpm and 37°C
  - Discard supernatant
- Alkylation:
  - Add 50 µL of 55mM IAA(10,2mg/ml) in 100mM ABC with 0.1% SDC
  - Incubate 30 min at 1200 rpm at 20°C **in the dark** (cover with aluminium)
  - Discard supernatant
- Wash beads 2x with 100 µL 100mM ABC with 0.1% SDC
- Add LysC solution 50 µl per sample
  (0.2 µg per sample, std is 0,5 µg/µl) in 100mM ABC with 0.1% SDC
  - Incubate 3h at 1200 rpm at 37°C
- Add Trypsin solution 50 µl per sample (0.2 µg per sample, std is 0,5 µg/µl) in 100mM ABC without 0.1% SDC
  - Incubate o/n (16h) at 1200 rpm at 37°C
- Next morning, take off peptides and place them into a new 0.5 mL low binding tube
- Wash beads twice with 100 µL 100mM ABC without 0.1% SDC and place it to the peptides
  - Too big SDC pellet if added
- SpeedVAC samples to lower volume to ~ 50 µl. (~ 30 min)

Measure volume of each sample (**should be below 65 µl!**), if volume is 0, add 50 µl MS-dH2O in order to dissolve the peptide. Sonicate dissolved peptides briefly.

Buffers:

- **Binding Buffer**:
  - 5 mM MgCl2 (1M stock solution at 4°C (Anna))
  - 5mM MnCl2 (0,629 mg/1mL)
  - 5mM CaCl2 (0,555 mg/1mL)
  - 0.5M NaCl (29,2 mg/1mL)
  - in 20mM TrisHCL pH 7.5
    (Stock Solution 0.5M; Use 2mL (0.5M) for 50 mL Binding buffer/ 0.04mL per mL) Check pH!
    MW: MgCl2 95,211 g/mol; MnCl2 125,844 g/mol; CaCl2 110,98 g/mol; NaCl 58,44 g/mol
  -
- **Elution Buffer (ConA)**:
  - 500 mM Methyl-alpha-D-mannopyranoside (97.09mg/1mL = 500 mM; MW:194.18 g/mol)
  - 10 mM EDTA (2,9mg/1mL; MW: 292,24 g/mol)
  - in 20 mM TrisHCl pH 7.5

- **Elution Buffer (WGA)**
  - 500 mM NaDGlucosamine (110.6 mg/1mL = 500 mM; MW: 221.21 g/mol)
  - 10 mM EDTA 2,9mg/1mL; MW: 292,24 g/mol)
  - in 20 mM TrisHCl pH 7.5

- **Combined Elution Buffer (ConA + WGA)**
  - Mix ConA + WGA elution buffer 1:1 to yield a combined elution buffer with 250 mM of each sugar.
  - (Add 10 mM EDTA, if it was not already added before.) -> was added before

  - **SDS buffer:**
    - 0.1 M TrisHCl pH 8.5 (1xUA)
    - 1% SDS
    - 250 mM NaCl (14.6 mg/mL NaCl, 10 mg/mL SDS)

  - **UREA Buffer (fresh)**
    - 8 M UREA
    - in 0.1 M TrisHCl pH 8.5 (for 10 mL use 4.8g UREA and 6.5 mL Tris-HCL pH 8.5)

8.2 Appendix 2: Point-to-point protocol: SP3 contaminant removal

A. Materials

- SP3 beads in a 4 µg/µL concentrated solution
  Combine 20 µL SeraMag A and 20 µL SeraMag B beads
  Add 160 µL of MS-H2O and let beads attach in the magrack, remove SN
  Rinse beads with 200 µL MS water by pipette mixing, repeat washing 2x
  Resolve beads in 100 µL MS water
- 100% Acetonitrile
- MS water
- 8% Formic Acid
- 0.1% Formic Acid
- Costar Spin-X Columns 0.22 µm (max. 2000 g)

B. Protocol

- Transfer dissolved peptides into fresh 1.5 ml loBind tube.
- Add 10 µL beads (**5 µl for supernatants**) to the samples (equals 20 µg of protein)
  Binding works better in neutral/basic conditions, if necessary add 50 mM ABC
- Add 100% ACN to a final concentration of > 95% (v/v) and incubate for 18 min at 1000 rpm on Thermomix, RT (I use 1300 µl for 50 µl ddH2O, just to be on the safe side)
  Maximal volume possible: 75 µL of sample-bead solution (+1425 µL ACN)
- Spin down and discard SN with magrack (magnetic rack)
- Wash beads with 200 µL 100% ACN, discard SN
- Add 50 µL MS water and mix with the pipette, spin down and collect SN with magrack in a fresh 0.5 ml LoBind tube
- Acifify the samples with 2 µL 8% FA
- Wash Spin-X (0.22 µm) with 200 µL 0.1% FA, spin for 2 min, discard flow-through
- Put the sample on the membrane and spin again for 2 min
- Discard filter, transfer to 0.5 ml loBind tube and dry samples in the Speedvac.
- Resolve in 20 µL 0.1% FA and sonicate for 30 sec
- Samples are now ready for the MS-measurement.

8.3 Appendix 3: Point-to-point protocol: SP3 for whole lysate proteomics

- After harvesting of primary microglia supernatant for hiSPECS, cells were lysed and stored at -20°C until tryptic digestion.
- 10 µg of lysate protein was digested using the SP3 Protocol as follows:

A. Materials

- Benzonase/MgCl:
  Benzonase (sigma >= 250 units/µL) → use 1:100 dilution
  100 mM MgCl2 solution → 10 µL per 100µl sample volume
  compatibility: Triton X < 0.4% (effective to 1%),; SDC < 0.4% (70% activity); SDS < 0.1%, at 1% active for 15 min; urea < 6M

- DTT:
  Dilute frozen 1M DTT stock with 50mM ABC to reach a final conc. of 200 mM DTT.
- ABC 50 mM:
  3.95 mg/mL in LC-MS grade water
- IAA 400 mM:
  73.98 mg/mL in 50mM ABC
- Acetonitrile 100%
- Ethanol 80%:
  Mix with LC-MS grade Ethanol with LC-MS grade water
- Trypsin 0.05 µg/µl
  Dilute frozen aliquots with 50 mM ABC
- LysC 0.05 µg/µl:
  Dilute frozen aliquots with 50 mM ABC
- SeraMag Beads A und B:
  Sera-Mag SpeedBeads A: (Fisher Scientific; CAT No. 09-981-121, Magnetic Carboxylate Modified)
  Sera-Mag SpeedBeads B: (Fisher Scientific; CAT No. 09-981-123, Magnetic Carboxylate Modified)
  Capacity ~100 µg of protein per µg of beads
  Best use > 0.1 µg/µL in the protocol as it is beneficial
  - 0.1% Formic Acid: Mass spec grade
  - Costar Spin-X Columns 0.22 µm (max. 2000 g)
  -
  - **Bead Preparation**

Combine 20µl of SeraMag A and 20µl of SeraMag B beads
Add 160µl of MS-H2O
Place Tube on a magnetic rack and let beads attach to the wall for 2 minutes. Once beads are attached, remove and discard supernatant.
Rinse beads with 200 µl of LC-MS grade water by pipette mixing (off the magnetic rack). Repeat washing step twice.

B. Protocol

- **<u>SP3 Preparation</u>**
- Dilute sample (i.e. 10-20 µg) in 50 mM TrisHCl or ABC to 35 µL
- Add 5 µl of 100 mM MgCl2 and 10 µL of 1:100 diluted Benzonase
- Incubate for 30min at 37°C at 1000 rpm
- Add 2.5 µl 200 mM DTT
- Incubate for 30 min at 37°C (thermomixer 1200 rpm).
- Add 5 µl IAA (400mM)
- Incubate for 30 min at 24 °C in the dark (thermomixer 1200 rpm.)
- Add 2.5 µl 200 mM DTT
    - ➔ Final Volume: **<u>= 60 µL</u>**

- **<u>SP3 Binding</u>**
- Add 10 µl beads. (~20 µg of beads) → 70 µL
- Add ACN 100% to a final conc. of 70% (v/v) ACN (+164µL) pipette **or** add Ethanol 100% to a final conc. of 80% (v/v) EtOH (+280µL) and mix immediately with the pipette

Incubate for 30min at RT (thermomixer 1000 rpm, 24°C).

- 200µl Ethanol 80%, 30sec incubation, discard the supernatant.
- 200µl Ethanol 80%, 30sec incubation, discard the supernatant.
- 200µl Ethanol 80%, 30sec incubation, discard the supernatant.
- 200µl Ethanol 80%, 30sec incubation, discard the supernatant.
- **<u>SP3 Digestion</u>**
- Add 20 µl of Trypsin (0.015 µg/µl) and 20 µl of LysC (0.015 µg/µl) to the beads for 20 µg of protein. (Trypsin:Prot and LysC:Prot = 1:80)
- Incubate for 30 min (up to 3 h) on a Thermomixer at 1000 rpm (37°C).
- Spin Down and incubate overnight (16 h) at room temperature
- **<u>Sample collection:</u>**
- Wash Spin-X with 200 µL 0.1% FA, spin for 2 min at 2000 g
- Discard flow-through and put samples into magnetic rack
- Transfer the supernatant on top of the membrane
- Add 20 µL of 0.1% formic acid to the beads
- Sonicate 2*30 s in the water bath.
- Collect sample by centrifugation and put them into the magnetic rack
- Transfer the supernatant on top of the membrane of the same Spin-X tube
- Add 2 µL of 8% formic acid to the sample to acidify
- Centrifuge 2 min at 2000 g and discard membrane
- Dry down the sample in the speed vac if necessary and resolve in desired amount (usually 10-20 µL) of 0.1% FA
- Samples are now ready for the MS-measurement.

8.4 List OF FIGURES

8.4 LIST OF TABLES

ACKNOWLEDGMENT

The completion of this PhD thesis was enabled by the combined support of multiple institutions. I was awarded a two-year fellowship by the Friedrich-Naumann-Stiftung für die Freiheit (FNF). Further generous support was provided by the Technical University of Munich – Institute for Advanced Study (TUM-IAS), and the the international Max Planck Research School for Molecular Life Sciences (IMPRS-LS). I would like to express my gratitude for the training you have provided me and for significantly influencing my personal development on a professional level over the past few years.

I extend my gratitude to Stefan for his unwavering faith and encouragement in my work and, perhaps even more important, my own ideas. His lesson that the quality of scientific output surpasses the sheer number of a journal's impact factor have profoundly shaped my approach to research. Furthermore, I want to thank Carl Blobel, who introduced me to Stefan and instilled in me the essence of scientific curiosity. Without his influence, I certainly would not have strived for a PhD degree.

Further, I want to thank my lab colleagues. In particular my dear friend Stephan Breimann for his unlimited support scientifically and personally. Next, I want to thank Sarah for her support with cell culture, Hung-En and Johanna for their help in the very beginning of my PhD journey, Goezde and Laura for their help with completion of this thesis, and Stephan Müller for support related to mass spectrometry. To Anke and Marcel for quickly resolving unforeseen problems.

To all my collaborators, in particular Vincent Grass and Andreas Pichlmair, who made decisive contributions to the COVID manuscript. To Janine Kimpel, Lydia Riepler, and Constanze Jakwerth for the fruitful collaboration.

Last but certainly not at least, I would like to express my unlimited gratitude to my family. My parents and siblings for supporting and encouraging me unconditionally. My IMPRS friends Marlene, Sophie, Pedro and the others. My friends from university and beyond Hanna, Sidney, Tasi, Ingmar, Marcus, Tobi, Fabi, Daniel, Sara, and Ben. Finally, I want to thank Sophie Robinson for her heartwarming support and always lending an open ear.